Data Storage and Retrieval using Photorefractive Crystals (Holographic Memories)

A Thesis presented for the degree of

Doctor of Philosophy

in

The Faculty of Science

University of Calicut, Calicut

by

RAVINDER KUMAR BANYAL

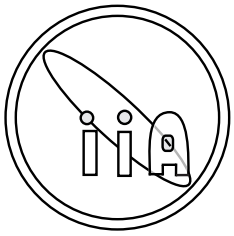

Indian Institute of Astrophysics

Bangalore, 560034, INDIA

October, 2005

Dedicated to

The Sweet Memories of My Grandfather

DECLARATION

I hereby declare that the matter contained in this thesis is the result of the investigations carried out by me at the Indian Institute of Astrophysics, Bangalore, under the supervision of Dr. K. Neelakandan. This thesis has not been submitted for the award of any degree, diploma, associateship, fellowship etc. of any university or institute.

Dr. K. Neelakandan
(Thesis Supervisor)

Ravinder Kumar Banyal
(Ph.D. Candidate)

Indian Institute of Astrophysics
Bangalore 560 034, INDIA
October, 2005

CERTIFICATE

This is to certify that the thesis entitled **"Data Storage and Retrieval using Photorefractive Crystals (Holographic Memories)"** submitted to the University of Calicut by Mr. Ravinder Kumar Banyal for the award of the degree of Doctor of Philosophy in the faculty of Science, is based on the results of the investigations carried out by him under my supervision and guidance, at the Indian Institute of Astrophysics, Bangalore. This thesis has not been submitted for the award of any degree, diploma, associateship, fellowship etc. of any university or institute.

Dr. K. Neelakandan
(Thesis Supervisor)

Professor, Department of Physics,
University of Calicut, Kerala
October, 2005

DECLARATION

I hereby declare that the matter contained in this thesis is the result of the investigations carried out by me at the Indian Institute of Astrophysics, Bangalore, under the supervision of Dr. B. Raghavendra Prasad. This thesis has not been submitted for the award of any degree, diploma, associateship, fellowship etc. of any university or institute.

Dr. B. Raghavendra Prasad
(Thesis Supervisor)

Ravinder Kumar Banyal
(Ph.D. Candidate)

Indian Institute of Astrophysics
Bangalore 560 034, INDIA
October, 2005

CERTIFICATE

This is to certify that the thesis entitled **"Data Storage and Retrieval using Photorefractive Crystals (Holographic Memories)"** submitted to the University of Calicut by Mr. Ravinder Kumar Banyal for the award of the degree of Doctor of Philosophy in the faculty of Science, is based on the results of the investigations carried out by him under my supervision and guidance, at the Indian Institute of Astrophysics, Bangalore. This thesis has not been submitted for the award of any degree, diploma, associateship, fellowship etc. of any university or institute.

Dr. B. Raghavendra Prasad
(Thesis Supervisor)

Indian Institute of Astrophysics
Koramangala, II Block
Bangalore, Karnataka
October, 2005

Acknowledgements

It was the best of times, it was the worst of times, it was the age of wisdom, it was the age of foolishness, it was the epoch of belief, it was the epoch of incredulity, it was the season of Light, it was the season of Darkness, it was the spring of hope, it was the winter of despair ...

The above opening passage from *'A Tale of Two Cities'* by Charles Dickens would aptly sum-up the high and low points of bygone years! And now, I am indeed delighted to acknowledge people who mattered most during this phase.

First and foremost, I would like to thank my supervisor Dr. B. Raghavendra Prasad for giving me an opportunity to work with him. Without his constant support and able guidance, this thesis would not have been complete. I am also grateful to him for creating excellent lab facilities and a very congenial work atmosphere that helped me to carry out the research work smoothly and independently.

I wish to acknowledge The Director, The Board of Graduate Studies, the library and the adminstration staff of IIA and CREST for their encouraging support and help rendered during my PhD tenure. I am grateful to Prof. K. Neelakandan for readily agreeing to act my co-guide at Calicut University.

I sincerely thank Dr. S. Chaterjee and Prof. K. P. J. Reddy from IISc for their valuable suggestions and advice on many occasions. I am obliged to Dr. B. R. S. Babu, Head of Physics Department at Calicut University, for his kind assistance during the PhD registration and other related formalities. I must thank Dr. Gopal Hegde for inviting me to Ngee Ann Polytechnic, Singapore. Personally, the visit was a great learning experience for me.

I must thank all my batch-mates and senior students, especially, Dharam, Suresh, Raji, Dilip, Shivarani, and Preeti for being quite considerate and accommodating.

Many people at CREST, including, D.K. Sahu, Parihar, Kemekar, and Ginu were of great help. Not to forget the generosity of the canteen people, security guards and technical staff who made the stay at CREST quite rememberable.

Manoj has been one of the most influential persons around. His indomitable conviction in secular and scientific values have left an indelible impression upon me and in turn compelled me to re-evaluate many of my own beliefs.

I thank Pandey Ji, Methi, Nagaraj, Blesson, and Vigeesh for weekend recreations. Many may not have liked the monotony of vegetarian food that I have often cooked at weekends. But, I presume that the disappointment was quickly forgotten amidst the euphoria of drinking sessions that led to many insightful revelations and healthy debates.

Ravindra (Bhatti) was a very close friend right from my early days in IIA. Many a times his simplicity and remarkable sense of humour helped me to overcome my own distressful moments. Maheswar has been very supportive and helpful all through out and I really thank him for giving me good company in IIA.

My acquaintance with Saigeetha was more of a coincidence. She has been a wonderful and inspiring person. I was immensely benefitted from her witty criticism and refreshing wisdom. I'm also grateful to her for introducing me to the fascinating field of geophysics.

Friends back home, namely – Dimmu, Bipan, Ripu, Surender, Sanju, Rajiv, Rockey and Vikas were quite affectionate and concerned. It is with great pleasure, I acknowledge their wholehearted support and appreciation.

Special thanks to my wife Kanchan who endured my absence without any trace of resentment or complain. Despite my prolonged isolation and total negligence, she displayed a remarkable composure and forbearance.

My younger brother Pawan has been a great source of strength for me. His presence at home, spared me from the burden of domestic responsibilities and hardships and allowed me to focus on my studies.

Finally, I would like to thank my parents for the overwhelming support and encouragement. Their generosity and liberal attitude has made all the difference for me.

Preface

There are several types of optical materials that exhibit nonlinear properties. The research work reported in this thesis is focused on two of its kind, namely, the inorganic photorefractive systems such as $LiNbO_3$ and $BaTiO_3$ and the bacteriorhodopsin; which is a biological molecule. The work presented in this thesis is broadly divided into two parts. The first part of the thesis (*Chapter 1* to *Chapter 4*) deals with the photorefractive effect in $LiNbO_3$ and $BaTiO_3$ crystals and their use in holographic data storage. The second part (*Chapter 5*) deals with the theoretical and experimental studies of bacteriorhodopsin and its applications in all-optical photonic switching. In its entirety, the most appropriate title for this thesis would have been, "***Data Storage and Optical Switching in Photoactive Media***." However, in accordance with University's guidelines, we are compelled to retain the topic of research (approved by the University at the time of registration) as our present thesis title even though the content of this thesis is more extensive.

In *Chapter 1* of the thesis, basics of nonlinear optics and related phenomenon are reviewed. Nonlinear optics is the branch of optics that describes the behaviour of light in nonlinear media –a media in which the polarization **P** responds nonlinearly to the electric field **E** of the light. Higher order polarization terms are responsible for the different types of nonlinear effects. The light-induced refractive index change is a fundamental nonlinear process that occurs in several photorefractive materials. A qualitative discussion on the principle and the physical mechanism of the photorefractive effect is outlined. A concise review of holography based data storage in photorefractive crystals is also presented. The importance and requirements of hight density memories is highlighted subsequently. In the later half of the *Chapter 1*, a brief introduction to all optical switching in nonlinear media is given. The bacteriorhodopsin molecule and its photophysical and absorption properties are briefly described. All the concepts and material discussed in this chapter provide a necessary background for the work presented in the later chapters.

Chapter 2 deals with the characterization of $BaTiO_3$ and $LiNbO_3$ crystals. A short but necessary review of theoretical formulism based on the band transport model and electro-optic effect is presented to facilitate physical understanding of the

phenomenon. The work includes detailed experimental studies of the light-induced absorption and two-wave mixing in undoped and Rh-doped $BaTiO_3$ crystals at different wavelengths and light intensities. Temporal and the steady-state behaviour of light-induced absorption is studied using a familiar pump-probe technique. A two-center charge transport model is proposed to explain the intensity dependence of the absorption coefficients in $BaTiO_3$. Important parameters such as build-up and decay rates, thermal excitation rates, and two-wave mixing gain have been obtained. Diffraction efficiency measurements and grating erasure studies in triply doped Fe:Ce:Ti:$LiNbO_3$ crystals are presented in the end.

Photorefractive crystals are widely used in the area of holographic data storage and related applications. Prior to recording, a data page is usually composed by a pixelated liquid crystal device such as spatial light modulator (SLM). For electrically addressed SLM, light transmittance of individual liquid crystal cell can be controlled separately by a voltage signal applied to individual pixel elements. However, the light transmission characteristics (transmittance versus voltage) of the liquid crystal SLM are highly nonlinear and exhibit a wide range of variations with different parameter settings. In *Chapter 3*, SLM characteristics and its calibration studies are presented. Basic principle and the theoretical background required to model the response of twisted nematic liquid crystal is explained next. A light propagation model for a twisted nematic liquid crystal cell is proposed based on Jones matric calculus. Intensity and phase modulation properties are studied to facilitate its (SLM's) use in data storage applications. In order to minimize the effect of nonlinear distortions, an appropriate preprocessing based on the power–law transformation of input gray scale images is also suggested. A simple and robust technique to determine pixel size and pitch of liquid crystal based SLM is proposed. The new method is based on optical diffraction from pixelated liquid crystal panel that has been modeled as a 2-dimensional array of rectangular apertures. A novel yet simple, two plane measurement technique is implemented to circumvent the difficulty in absolute distance measurement.

General layout of HDSS is presented in the beginning of *Chapter 4*. The page oriented architecture of HDSS allows recording of binary as well as pictorial (grey scale

images) information. Several internal as well as external factors may contribute to the noise, which in turn leads to degradation in the storage performance. Implementation of modulation and error correction codes, therefore, becomes indispensable to maintain the data integrity of the stored information against the system noise. This is also important to ensures a low bit-error-rate (BER) and a high signal-to-noise ratio (SNR) that is necessary to increase the overall storage capacity of the medium. However, the price for the immunity against the noise is paid by adding extra bits of information (overhead) to the source data. The overhead information makes the overall size of the data to be stored very large. One of the ways to circumvent this problem is to use some data or image compression techniques. One of the goals of this Chapter is to develop an image compression scheme for HDSS. The *Chapter 4* also describes the principle of data compression –the features in the image that make the compression possible. Implementation of Haar transform based image compression, followed by the efficient binary conversion of numerical data using Huffman coding, is illustrated with some examples. Experimental details of the HDSS in the lab include a discussion on Fourier image-plane recording and spatial and rotation multiplexing scheme developed for storing multiple pages. A block-based mean and median processing of CCD image is proposed to extract the sequence of 1s and 0s from binary page. Results of holographic recording and retrieval of astronomical images in Fe:Ce:Ti:$LiNbO_3$ are presented in the end.

Chapter 5 discusses theoretical and experimental studies on bR and its applications in all-optical photonic switching. A time-dependent theoretical model based on rate equations for all the photochemical states of bacteriorhodopsin (bR) is developed. A recursive method is adopted to solve the rate equations with explicit temporal and intensity dependence. Simulated results for a thin wild type bR film show that each intermediate state has an optimum population that depends uniquely on incident intensity and time. This model provides an analytical framework for optimization of bR for various electronics and photonic applications. The experimental work on nonlinear absorption based, high contrast, all-optical switching in photochromic bacteriorhodopsin films is presented at the end of *Chapter 5*. The switching action is accomplished by controlling the transmission of a weak probe

beam through bR sample with the help of a strong pump beam illumination at wavelength 532 nm. Switching properties of bR films depends on several experimentally controllable parameters such as probe wavelength, pump beam intensity and pump excitation rates. A comparative study of the switching behavior and other parameters of practical use is carried out at different probe wavelengths (543 nm, 594 nm and 633 nm), beam powers and pump excitation rates. Results are interpreted using a model based on simplified three–level scheme.

Considering the great advancement in the present state-of-art technology, the research in optics and photonics in particular, is likely to play a leading role in future data storage and communication technology. In the context of the work presented in this thesis, the future directions and the possibilities to extend it further, are discussed in *Chapter 6*.

The List of Refereed Publications

1. Ravinder Kumar Banyal and B. R. Prasad, *Light Induced absorption in photorefractive $BaTiO_3$ crystals*, Journal of Applied Physics, **93**, 9466–9469 (2003).

2. Ravinder Kumar Banyal and B. R. Prasad, *Two-wave mixing and light-induced absorption dynamics in Photorefractive $BaTiO_3$ Crystals*, Journal of Indian Institute of Science, **83**, 61–71 (2003).

3. S. Chatterjee, Ravinder Kumar Banyal and B. R. Prasad, *On the resolving power of an echelle grating in the presence of a corrugated wavefront of incidence*, Bulletin of Astronomical Society of India, **31**, 461-463 (2003).

4. Ravinder Kumar Banyal, Gopal Hegde, B. R. Prasad and K. P. J. Reddy, *A time–dependent multistate model for bacteriorhodopsin photocycle*, Current Applied Physics, **5**, 133–138 (2005).

5. A. J. Saigeetha and Ravinder Kumar Banyal, *Alfred Wegener –From Continental Drift to Plate Tectonics,* Resonance, **10**, 43–59 (2005).

6. Ravinder Kumar Banyal and B. R. Prasad, *Pixel size and pitch measurements of liquid crystal spatial light modulator by optical diffraction*, Pramana – Journal of Physics, **65**, 291–296 (2005).

7. Ravinder Kumar Banyal and B. R. Prasad, *High contrast, all-optical switching in bacteriorhodopsin films,* Applied Optics, **44**, 5497-5503 (2005).

Conference Proceedings

1. Ravinder Kumar Banyal, B. Raghavendra Prasad, *Intensity Dependent Absorption Coefficient & Temporal Properties of TWM in Photorefractive $BaTiO_3$ crystals*, India-Japan Workshop on New Materials in Molecular Electronics (NAMME), December 10–11 (2001), p62, National Physical Laboratory, New Delhi.

2. Ravinder Kumar Banyal, B. Raghavendra Prasad, *Two-wave Mixing Dynamics in photorefractive $BaTiO_3$ crystals*, Proc. DAEBRNS National Laser Symposium, November 14-16, (2002), p546, Sri Chitra Tirunal Institute of Medical Sciences and Technology, Thiruvananthapuram, India.

3. Ravinder Kumar Banyal, B. Raghavendra Prasad, *Light-induced Absorption in photorefractive $BaTiO_3$ crystals*, Proc. DAEBRNS National Laser Symposium, November 14-16, (2002), p548, Sri Chitra Tirunal Institute of Medical Sciences and Technology, –Thiruvananthapuram, India.

4. Ravinder Kumar Banyal, Ginu Rajan and B. Ragavendra Prasad, *Pixel size and pitch measurements of liquid crystal spatial light modulator by optical diffraction*, 7th International Conference on optoelectronics, fiber optics and photonics, December 8–11 (2004), p349, Cochin, India.

5. Ravinder Kumar Banyal and B. R. Prasad, *Interferometry based measurements of photoinduced refractive index changes in bacteriorhodopsin films*, XXX Optical Society of India Symposium on Optics and Opto-electronic, January 19–21 (2005), p80, National Physical Laboratory, New Delhi.

Contents

List of Figures

List of Tables

Chapter 1

Introduction

This chapter provides a concise review of the nonlinear optics (NLO), photorefractive (PR) effect and related phenomenon in inorganic crystals. It is also intended to give a general overview of bacteriorhodopsin –a biological molecules that has many useful optical properties. This chapter is not a comprehensive review of the field but rather a specific account of essential theories, concepts and literature surveys that form the basis for the work presented in later chapters. The first section briefly introduces the field of NLO and the role of material polarization responsible for various nonlinear effects. A quantitative discussion on the origin of PR effect, and its basic mechanism are explained in section 1.2. The principle of holographic data storage in photorefractive crystals is outlined in section 1.3. A brief introduction to all optical switching in nonlinear media is presented in section 1.4. Finally, the bacteriorhodopsin molecule and its photophysical and absorption properties are briefly described.

1.1 Nonlinear Optics

Light from an ordinary source does not alter the optical properties of the medium in which it travels. In such a case, the medium is termed as *linear*, whose optical properties i.e., refractive index and absorption coefficient etc., do not depend on light intensity. A linear medium does not allow one light beam to effect the other light beam. Strictly speaking, any linear media may become nonlinear at sufficiently

high light intensity. The reason is that the electric filed associated with ordinary light sources is far too weak to modify any material properties. It is only after the advent of laser in 1960s, which marks the beginning of the field of the NLO, it became possible to obtain highly coherent, monochromatic and intense beam of light [1]. The interaction of strong coherent radiations can greatly modify the optical properties of the material and in addition can give rise to several new optical effects and novel phenomenon. Study of these new effects and the related techniques are the major issues of NLO. These processes generally are called nonlinear effects because their strength typically depends on the square (or some higher power) of intensity rather than simply on the amount of light present. This means that nonlinear effects are weak at low powers, but can become much stronger when light reaches high intensities.

When a light wave propagates through an optical medium, the oscillating electromagnetic field exerts a polarizing force on all the electrons comprising the medium. This produces a polarization response $\mathbf{P}$ of the medium which is linearly proportional to the electric field $\mathbf{E}$ of the light wave. At low illumination level the strength of radiation filed is much smaller than the field that binds electrons to the atom. Based on this assumption of linearity, Maxwell's equations lead to set of linear differential equations in which only terms proportional to $\mathbf{E}$ are involved. As a result there is no coupling between different light beams when they pass through medium.

The optical nonlinearity results from an anharmonic response of the bound electrons driven by optical frequencies of the radiation fields. A significant perturbation of the charge distribution may occur if the radiation field is comparable to the intra-atomic field ($\simeq 10^{11}$ V/m) of the material. Therefore, the relationship between induced polarization and radiation field no longer remains linear. In general, the polarization response of dielectric media to applied optical filed is expressed using a series expansion of the form

$$\mathbf{P} = \epsilon_o \left(\chi^{(1)}\,\mathbf{E} + \chi^{(2)}\,\mathbf{EE} + \chi^{(3)}\,\mathbf{EEE} + \cdots\right) \tag{1.1}$$

where $\chi^{(n)}$ is nth order material susceptibility which is a tensor of rank $n+1$. The first term in Eq. (1.1) is related to the dielectric constant and the refractive index of the medium by $n^2 = \epsilon/\epsilon_o = 1 + \chi$. This term is sufficient to describe all

the observed linear optical properties of the medium, whereas higher order terms are needed to explain most of the nonlinear effects noted below.

The first experiment in NLO was performed by Franken *et al.* in 1962. They demonstrated second-harmonic generation (SHG) in a quartz crystal using pulsed ruby laser [2]. Reports of new phenomena quickly followed once the coherent optical radiation source became readily available. Some of these early observations were, two-photon absorption by Kaiser and Garrett [3], stimulated Raman scattering by Ng and Woodbury [4], third-harmonic generation by Maker and co-workers [5], and anti-Stokes frequency mixing by Terhune and co-workers [6].

Nonlinear effects can be broadly separated into two categories. In first, the nonlinear interactions of light field with medium cause the optical frequency shift of the incident field. The frequency shift can also be realized by external parameter such as electro-optic effect or acousto-optic effect that modulate the optical characteristics of the medium. Well known examples of such type are: harmonic generation, frequency up and down conversion. In the second category, the frequency of the incident light wave is preserved but the nonlinear operations are realized on the spatio-temporal profile of the coherent light. In this case optical Kerr type nonlinearities are exploited for soliton generation, phase modulation, self-focusing, bistable operation, phase conjugation etc.

Most of the materials used in nonlinear optics are birefringent in nature. That is, their refractive index depends on the polarization and direction of propagation of incident light. Therefore, certain phase matching conditions (commonly achieved using angle tuning or temperature tuning) may be required to satisfy for observing nonlinear effects. The following list briefly summarizes first order (linear), second order and third order susceptibility terms and associated linear and nonlinear optical effects.

First order effects

The first order effects are described by the term:

$\mathbf{P}^{(1)}(\omega_1) = \epsilon_o \chi^{(1)}(\omega_1) : \mathbf{E}(\omega_1)$

Which means that, to the first approximation, a monochromatic wave at ω_1 can only induce polarization which produces a secondary wave radiation at the

same frequency. Examples are: reflection, refraction, dispersion, absorption, refractive index, scattering and birefringence etc.

Second order effects

$\mathbf{P}^{(2)}(\omega_3) = \epsilon_o \chi^{(2)}(\omega_3; \omega_1, \omega_2) : \mathbf{E}(\omega_1)\mathbf{E}(\omega_2)$

where $\mathbf{E}(\omega_i)$ is the amplitude of the field at frequency ω_i. The physical meaning of this quantity is that in the second order approximation, the radiation at new frequency ω_3 can be induced by two incident monochromatic waves with frequency of ω_1 and ω_2. The second order susceptibility $\chi^{(2)}$ is a tensor of third rank having $3^2 = 27$ components.

- Second harmonic generation: $\chi^{(2)}(2\omega;\, \omega, \omega)$
- Optical rectification: $\chi^{(2)}(0;\, \omega, -\omega)$
- Parametric mixing: $\chi^{(2)}(\omega_1 + \omega_2;\, \omega_1, \omega_2)$
- Pockel's effect: $\chi^{(2)}(\omega;\, \omega, 0)$

Because of the symmetry restrictions, the even order susceptibilities are zero in materials with inversion symmetry. As a result, these effects are commonly observed in crystals that lack inversion symmetry.

Third order effects

$\mathbf{P}^{(3)}(\omega_4) = \epsilon_o \chi^{(3)}(\omega_4; \omega_1, \omega_2, \omega_3) : \mathbf{E}(\omega_1)\mathbf{E}(\omega_2)\mathbf{E}(\omega_3)$.

The physical meaning of the above expression is that in the third order approximation, the radiation at the new frequency $\omega_4 = \omega_1 + \omega_2 + \omega_3$ can be generated by an intense optical field containing frequency components ω_1, ω_2 and ω_3. Third order susceptibility $\chi^{(3)}$ is a forth-rank tensor having $3^3 = 81$ components. There are several possible combinations in which different fields can be combined. Some of the examples include:

- Third harmonic generation: $\chi^{(3)}(3\omega;\, \omega, \omega, \omega)$
- Non-degenerate four-wave mixing: $\chi^{(3)}(\omega_1 + \omega_2 + \omega_3;\, \omega_1, \omega_2, \omega_3)$
- Stimulated Raman Scattering: $\chi^{(3)}(\omega + \Omega;\, \omega, -\omega, \omega + \Omega)$
- Stimulated Brillouin Scattering: $\chi^{(3)}(\omega - \Omega;\, \omega, -\omega, \omega - \Omega)$

- Degenerate four-wave mixing: $\mathrm{Re}\,\chi^{(3)}(\omega;\,\omega,\omega,-\omega)$
- Two photon absorption: $\mathrm{Im}\,\chi^{(3)}(\omega;\,\omega,-\omega,\omega)$
- DC induced harmonic generation: $\chi^{(3)}(2\omega;\,\omega,\omega,0)$

The $\chi^{(3)}$ effects take place in all materials irrespective of them possessing inversion symmetry. Third-order processes can be observed with electric dipole interactions in materials that have center of symmetry, such as gases, liquids and some solids, since in these materials they are the lowest order non-zero nonlinearities allowed by electric dipole transitions

The wave equation for nonlinear medium can be derived using Maxwell's equations for an arbitrary homogenous dielectric medium [7]:

$$\nabla^2\mathbf{E} - \frac{1}{c^2}\frac{\partial^2\mathbf{E}}{\partial t^2} = \mu_0\frac{\partial^2\mathbf{P}}{\partial t^2} \tag{1.2}$$

Using Eq. (1.1) it is convenient to express $\mathbf{P}$ as a sum of linear and nonlinear parts,

$$\mathbf{P} = \epsilon_0\chi\mathbf{E} + \mathbf{P}_{\mathrm{NL}} \tag{1.3}$$

$$\mathbf{P}_{\mathrm{NL}} = \chi^{(2)}\,\mathbf{EE} + \chi^{(3)}\,\mathbf{EEE} + \cdots \tag{1.4}$$

Substituting Eqs. (1.3) and (1.4) in Eq. (1.2) we get,

$$\nabla^2\mathbf{E} - \frac{1}{v^2}\frac{\partial^2\mathbf{E}}{\partial t^2} = \mu_0\frac{\partial^2\mathbf{P}_{\mathrm{NL}}}{\partial t^2} \tag{1.5}$$

where, $v = c/n$ is the velocity of the light in the medium. The right hand side of the Eq. (1.5) can be identified with a source term which is responsible for generating frequencies other than the frequency of incident light.

The research carried out in the first decade of NLO was basically focused on inorganic materials. This lead to the development and growth optimization of material such as KH_2PO_4, $LiNbO_3$, BBO, $NH_4H_2PO_4$, LBO, BGO, KTP, KTA, BSO, quartz (SiO_2), cadmium selenide (CdSe), cadmium germanium arsenide ($CdGeAs_2$) etc. These crystals continue to play an important role in vast areas of NLO and related applications.

The enhancement of the efficiency of the nonlinear process by appropriate choice of nonlinear optical material constitutes a central concern in all these studies. Apart

from that, the current trends in organic materials, especially the polymeric thin films have shown a greater promise in terms of high damage threshold, large optical nonlinearities, wide transmission and high frequency conversion efficiency [8]. The development in NLO is intimately related with the progress in NLO materials.

1.2 Photorefractive Effect

Photorefractive (PR) effect refers to light-induced refractive index change in optical materials. Photorefractive materials are distinguished from other nonlinear optical materials by their ability to generate large index of refraction changes in response to relatively low light intensity. The optical light intensity determines the speed but not the magnitude of the nonlinearities.

The PR effect was accidently discovered in Bell Laboratories by Ashkin *et al.* in 1966 [9]. They noticed a strange fanning of light beam as it passed through a $LiNbO_3$ crystal. In beginning, this strange behaviour was attributed to some sort of laser induced damaged of the crystal. However, very soon, a *band transport model* based on the photoexcitation and migration of free charges, was proposed to account for it. Later, many inorganic crystals were found to be exhibit PR effect namely, $LiTaO_3$, $BaTiO_3$, KTN, BSO, $BaNaNb_5O_{15}$, $KNbO_3$, $Bi_{12}SiO_{20}$ etc. Since then a lots of experimental and theoretical efforts have been devoted for understanding the physical mechanism responsible for PR effect. A theoretical formulism based on a set of rate equations for electron and trap densities, was provided by Chen [10]. Next major theoretical contribution by Amodei *et al.* in 1971, was the recognition of the fact that thermal diffusion of the free carrier leads to space-charge field [11].

The *band transport model* of PR effect was complete with an important contribution from Kukhtarev who in 1976 derived the expression for space-charge field and complex response time [12, 13]. According to this model, inter-valence impurities are responsible for the PR effect in inorganic crystals. As shown in Figure 1.1, the energy levels of these impurities lie between the band gap of the material. The detailed mechanism of PR effect is illustrated in Figure 1.2. The main steps involved in PR effects can be summarized as follows:

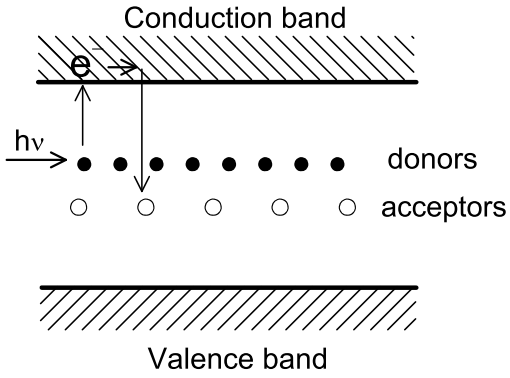

Figure 1.1: Band transport model for PR effect in inorganic crystals.

◇ A crystal is illuminated by a periodic intensity pattern of dark and bright fringes, usually obtained from two interfering coherent laser beams.

◇ In the brighter region, the electrons are photoexcited from the impurity atoms into the conduction band, leaving behind the holes (positively charges impurity ion).

◇ While in conduction band, the electrons can freely move under the influence of drift or diffusion, and eventually recombine with impurity ions in the darker regions. Once back in the impurity level, the electrons are trapped and can no longer move unless re-excited back into the conduction band.

◇ The segregation of electrons in the dark regions and holes in the bright regions of the crystal, creates an internal electric field, known as a *space-charge field*. Since the electrons and holes are trapped and become immobile, the space charge field persists even when the illuminating beams are removed.

◇ The periodic space-charge electric field, in turn, causes periodic modulations of the refractive index of the material via electro-optic effect (the Pockell's effect). The resulting refractive index grating follows the light interference pattern originally imposed on the crystal.

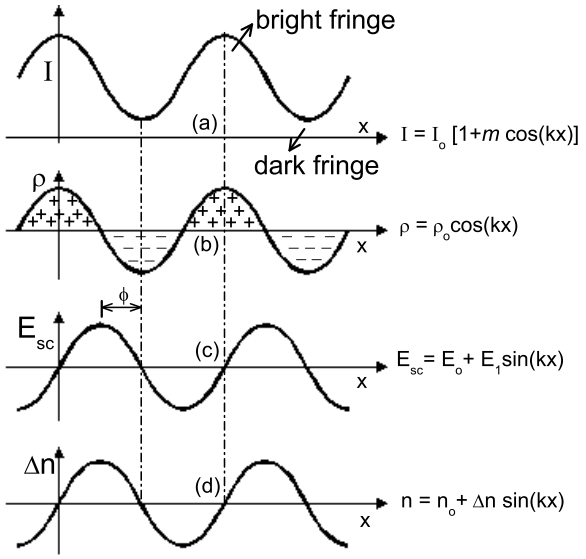

Figure 1.2: Mechanism of PR effect, (a) crystal illumination with sinusoidal light intensity pattern, (b) charge carrier density distribution after photoexcitation and migration, (c) generation of space-charge field and (d) the resulting refractive index modulation.

- ◇ The refractive index grating, like any other grating, can diffract the incident light to re-create the original beam. For example, in the case of a hologram, illuminating the grating with just the reference beam causes the reconstruction of the original signal beam.

One of the important features of the PR effect is the phase shift ϕ that may exists between incident light intensity and the refractive index modulation. For the diffusion dominated charge transport, the space-charge field and thus Δn, is shifted by a quarter of a grating period (equivalent to a phase of $\pi/2$) with respect to the intensity pattern.

In 1980, Feinberg et al. proposed the *hopping model* as an alternate to the charge transport model [14]. According to this model, electrons or holes directly tunnel from one site to another when exposed to optical radiations. As opposed to the deterministic nature of the charge transport model, the physical basis for the hopping model is statistical. However, in the limit of zero external field, both these models lead to identical expression for fundamental Fourier components of the steady-state

space-charge field and the complex response time. The potential applications of PR index include holographic data storage, optical information processing, image amplification, distortion correction using phase conjugation, holographic interferometry and pattern recognition etc. [15–19].

Until 1990 all photorefractive systems were inorganic crystals such as those listed above. The first observation of the photorefractive effect in an organic material was made in 1990 [20, 21]. This was followed in short time by the discovery of photorefractive polymers by Ducharme *et al.* [22]. The early photorefractive systems, polymeric and crystalline, were inefficient compared to inorganic systems but in recent years the efficiency and sensitivity of photorefractive polymers have become equal to inorganic crystals. There are many reasons for pursuing the development of photorefractive polymers. For example, polymers are easily cast into high quality thin films, can be modified easily by chemical doping. Additionally, polymers are compatible with integrated circuit processing techniques, making them potentially useful in integrated optical device applications. Semiconductor materials have also gained much interest due to their high carrier mobilities and sensitivity in infrared region. Some of the PR semiconductor include GaAs, CdS, InP, GaP and CdTe.

1.2.1 Light-induced Absorption in PR Crystals

Normally, the absorption coefficient of a linear medium is independent of the light intensity. However, absorption changes as a function of incident light intensity have been observed in many PR nonlinear materials. The light-induced absorption was first observed in $BaTiO_3$ crystal by Motes and Kim in 1987 [23]. They reported an increase in absorption under continuous wave illumination at typical intensity of 100 kWm^{-2}. The experimental results were interpreted using two different kind of impurity centers involved in absorption process [24]. Later on, the two-center charge transport model was extended to explain the observed sub-linear intensity dependence of photoconductivity in $BaTiO_3$ [25].

1.2.2 Wave Mixing in PR Media

Many of the most interesting and practical applications of PR effect arise due to optical wave-mixing in the PR crystals. In two-wave mixing (TWM), a pair of coherent laser beams intersect inside a PR medium as shown in Figure 1.3(a). If two beams are of same frequency, a stationary interference pattern is formed. The periodic variations in intensity produces periodic modulation in index of refraction. The grating thus formed is usually called as index grating, phase grating or volume grating. Different planes of the volume grating scatter optical light in a similar manner as X-rays are diffracted from a 3-dimensional periodic array of crystal lattice. If λ is the wavelength of light (inside the medium), Λ is grating spacing, θ is the half angle of intersection of two light beams, then the beam diffraction occurs for angles that satisfy Bragg's law:

$$2\Lambda \sin\theta = N\lambda \tag{1.6}$$

$$\text{or} \quad 2k \sin\theta = N\frac{2\pi}{\Lambda} \tag{1.7}$$

where N is an integer representing diffraction order, $k = 2\pi/\lambda$ is the light propagation vector and $K = 2\pi/\Lambda$ is grating wave vector.

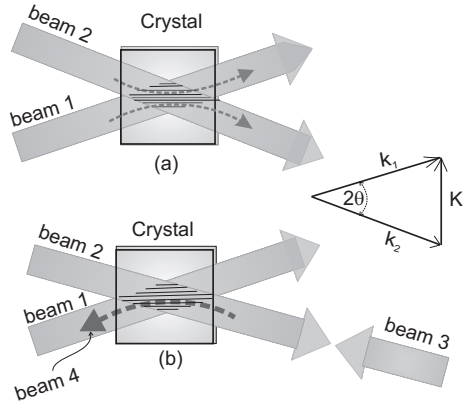

Figure 1.3: Transmission geometry of wave mixing in PR crystal. (a) Two-wave mixing and (b) generation of phase conjugate beam in four-wave mixing.

In Figure 1.3(a), the light wave vectors k_1 and k_2 of two beams are related to grating wave vector by $\mathbf{K} = \pm(\mathbf{k}_1 - \mathbf{k}_2)$. Since the Bragg's conditions are perfectly satisfied, the index grating causes a part of beam 1 to diffract in the direction of beam

2. Similarly, a part of beam 2 is diffracted in the direction of beam 1. Kogelnik first developed the coupled-wave theory for volume holograms in 1969, and also predicted the diffraction efficiency and Bragg selectivity for thick gratings [26]. Staebler and Amodei, in 1972, worked out the coupled mode theory to show that diffusion process could lead to unidirectional energy transfer from one beam to another [27].

As explained in the previous section, the index grating has a finite spatial phase shift ϕ relative to the interference pattern. In PR crystal such as $BaTiO_3$, where the charge transport mechanism is driven by diffusion only process, has $\phi = \pm\pi/2$. In addition, upon diffraction from the index grating, each beam is phase shifted by $\pi/2$. A constructive interference ($\pi/2 - \pi/2 = 0$) between direct beam and diffracted beam results in increase in intensity in one direction. On the other hand, the overall intensity diminishes when the direct beam and the diffracted beams interfere ($\pi/2 + \pi/2 = \pi$) destructively. The question as to which beam gains and which beam looses energy depends on the direction of the c-axes of the crystal and whether the charge carriers are electrons or holes.

Potential applications of TWM includes coherent image amplification, novelty filtering, self-phase conjugation, optical computing beam fanning limiters and neural networks [28–35]. Many relevant material parameters such as the charge mobility, dielectric constant, trap densities, electro-optic coefficients, photoinduction rate etc. can be determined using wave mixing techniques [36, 37]. In coupled-wave theory the nonlinear Eq. (1.5) is often used to derive linearly coupled partial differential equations that govern the wave-mixing dynamics in the nonlinear medium [38].

Four-wave mixing (FWM) is a phenomena arising from the interaction of three coherent optical fields through the third order nonlinear susceptibility which generates a fourth beam. In this method, a nonlinear medium is pumped by two counter propagating laser beams. A new beam can be generated when a signal beam is incindent into the medium. Newly generated beam travels in direction opposite to the signal beam. Figure 1.3(b) shows one of the possible geometries used in FWM. Beam 1 and beam 3 are two counterpropagating pump beams, beam 2 is signal beam and beam 4 is the time-reversed replica of the signal beam. The beam wave vectors satisfy the following relations: $\mathbf{k}_2 = -\mathbf{k}_3$ and $\mathbf{k}_1 = -\mathbf{k}_4$. For

the FWM in PR media, the refractive index grating, written by signal beam and pump beam 2, diffracts the beam 3 to generate the phase conjugate replica of the signal beam. Optical phase conjugation techniques have been extensively used in distortion corrections, real-time holographic imaging, adaptive optics systems, laser amplifiers, novel interferometers and signal propagating in turbulent atmosphere. Many of these applications are extensively discussed in review articles by Pepper *et al.* [17, 18, 39].

1.3 Holographic Data Storage

1.3.1 Holography

Dennis Gabor was the first to invent the holography in 1948 while trying to improve the quality of electron microscope images [40]. In holography, two coherent beams, one is called reference beam and the other is called signal beam (scattered from the object), are required to form the interference pattern. The resulting interference pattern contains both the amplitude and phase information of the object. The intensity of the interference pattern can be recorded by placing an appropriate light-sensitive medium (i.e., photographic film or photorefractive crystal) in the region of interference. This recorded fringe pattern or grating is referred to as a hologram. The recorded hologram when illuminated by the same reference beam can diffract the light in the direction of object beam. The diffracted beam contains both the phase and amplitude information of the original object beam.

In the early stages of the holography, only one beam was used to illuminate both the object and the film [41]. This type of hologram was generally called Gabor-type or in-line hologram. One disadvantage of Gabor-type hologram was that both real and virtual image components were reconstructed simultaneously and along the same direction as the transmitted reference beam. Gabor's holography was limited to film transparencies using a mercury arc lamp as the light source and holograms contained distortions and an extraneous twin image.

Just as in the case of NLO, it was only after the invention of laser that the field of holography was revolutionized. Leith and Upatnieks in 1962 proposed a scheme for

off-setting the direction of incidence of the reference beam in order to spatially separate the locations of the reconstructed images [42,43]. Using the *off-axis* technique the quality of the reconstructed images of a 3-dimensional object was substantially improved. Their pioneering work led to standardization of the equipments used to make holograms. Another major advance in display holography occurred in 1968 when Dr. Stephen A. Benton invented white-light transmission holography while researching holographic television at Polaroid Research Laboratories. The white light hologram could be viewed using an ordinary incandescent light bulb. The particular significance of Benton's invention was the embossing technique which led to mass production of holograms. Embossed holograms are now being used by the advertising, publishing, banking industries, security checks etc.

1.3.2 Volume Holography

The hologram stored in thin photographic films were essentially planar and had two distinct disadvantages [44, 45]. First, the whole process of hologram formation and subsequent development was time consuming, so it could not be utilized in any real time application. Secondly, the planer nature of the hologram recorded on the thin film did not support the angular selectivity. The theory of optical information storage in solids, with density limit V/λ^3, was put forth by van Heerden in 1963 [46]. He postulated that the recording of the interferences pattern inside the 3-dimensional medium can be used as a means for information storage and retrieval. In the year 1968, Chen *et al.* proposed the possibility of using $LiNbO_3$ as storage media [47]. In the following years, holographic recording and read out was also demonstrated in other photorefractive materials [11, 48]. Unlike photographic films, the inherent Bragg selectivity in volume holography, allows the storage and retrieval of multiple holograms. As a result, the information storage capacity can be greatly increased by volume holography.

There is an ever increasing demand on faster and high density memories to process and archive massive amount of data that is generated in weather forecasting, parallel computation, internet and multimedia applications, various remote sensing and on–board missions, medical imaging, astronomical data gathered from ground

or space based observations. Improvement in conventional storage technologies such as semiconductor based hard drives, magnetic tapes, compact disk (CD) and digital versatile disk (DVD) have so far managed to cater the required demands satisfactorily. However, an alternative approach based on volume storage technology may serve better for the future needs owing to its very large data storage density (>1 Tbits/cm^3) and extremely fast data transfer rates (>1 Gbits/s) [49].

The research in holographic data storage began in late 1960s and early 1970s. From historical perspective, development of holographic data storage system has not been very bright. Much of this can be attributed to the lack of enabling technologies (e.g., suitable recording material, monochromatic laser source with sufficient power, and 2-dimensional page composer, detector arrays) in the initial phase. It is only after the emergence of electronics and entertainment industries for consumer market that the liquid crystal displays and charged coupled devices became readily available. The last four decades of literature covers a wide areas of research carried out in holographic data storage. The important contributions comprise –excellent papers on theoretical analysis [50–53], novel architectures [54–58], versatile system designs [59–63], new multiplexing techniques [64–69], implementation of channel and modulation codes [70–75], development of new storage materials [76–78] and several milestones in different prototyping [79, 80].

1.3.3 Principle of Holographic Data Storage

Unlike bit–wise recording in conventional storage systems, the read and write operations in these devices are carried out using page–oriented architecture where several pages of data can be multiplexed within the same volume. Prior to recording, a data page is usually composed by a pixelated liquid crystal (LC) device such as spatial light modulator (SLM). The light transmission properties of each SLM pixel can be controlled independently by applying external voltage. A computer program converts an image or a data into 2-dimensional bit patterns of 1's and 0's. This pattern is transfered onto SLM by electronics circuitry which drive the LC pixels. An expanded laser beam passing through SLM panel would carry the binary patten of 1's and 0's. Holography based storage requires a coherent illumination of SLM by a

laser beam, whereas, incoherent light is sufficient for recording based on two–photon absorption and spectral hole burning [81–83].

The image carrying "object beam" is made to interfere with a plane reference beam. A photorefractive medium placed in the region of interference can store the image or data in the form of refractive index grating described in the previous section. The original page of data can be read at later time by illuminating the medium with the same reference beam that was used to record it. The diffracted beam which is replica of the original object beam can be imaged using a 2-dimensional charged coupled device (CCD). Different multiplexing techniques such as angular multiplexing, rotational multiplexing, shift multiplexing, wavelength multiplexing or a suitable combination of these can be used to store large number of data pages in the same medium [64–69]. In multiplexing, the holographic structure of one page is intermixed with the holographic structure of the other page. *Retrieval of an individual page with minimum cross talk is the consequence of volume nature of recording and its behavior as a highly tuned structure* [84].

1.3.4 Advantages of Holographic memories

Very high read-write speed: The page oriented nature of holographic memories allows the data to be recorded or retrieved in parallel, i.e., an entire data page comprising over a million bits can be written or read simultaneously. This allows the possibility of obtaining a data transfer rates as high as 1 Gb/s [85]. In contrast, the sequential (bit-wise) data read and write operations in conventional memories are far slower.

Rapid access time: Advanced holographic memories would rely on the movement of the light beam using ultra-fast devices such as acousto-optics deflectors or galvanometers. These devices have very short access time in the range 10 μs to 1 ms. Moreover, the angle of a reference beam can be directly adjusted to read a particular hologram from a stack of thousands of holograms without having the need to go in a sequence. In conventional memories systems, the access time is relatively longer due to inertia induced by physical motion of

the read-write head.

High density: Holographic storage can record up to 10 000 number of data pages in the same volume. Each two-dimensional data page can have a capacity over a million bits per page . The projected data density of volume storage is as high as 100 bits $\mu\mathbf{m}^{-2}$, which far exceeds the density in conventional (e.g., 2.5 bits $\mu\mathbf{m}^{-2}$ in DVDs) storage media [73].

Immunity against noise: In conventional storage devices such as hard disk; floppy; CD or DVD, each data bit has a unique location on the surface of the medium. Such data bit may be represented by a local change of some physical property of the medium. A local damage in the medium may cause an irreversible data loss from these locations. In holographic memories, there is no one–to–one correspondence between data bit and the storage location in the medium. Intrinsic nature of hologram allows the information about each data bit to be distributed throughout the recording volume of the medium. The local defect in the medium may cause slight reduction in signal to ratio but the information can still be recovered.

Associative retrieval: It is possible to implement some powerful and novel search capabilities based on optical correlation techniques in holographic memories. If N holograms are multiplexed in a medium, then the diffraction efficiency of a reconstructed hologram depends on the similarity between reading beam and the original recording beams. In associative retrieval, a stack of N holograms is illuminated by a read out beam which carries the search template. A search pattern or template comprises a small portion of the original image that is to be searched among N holograms. Each hologram diffracts some amount of light in the direction of original reference beam. The strength of each reconstructed beam is proportional to the degree of correlation between the search pattern and the content of the page. The array of diffracted beams can be focused and imaged onto the CCD detector for further processing. The highest intensity beam corresponds to the search hit. Since the correlation is performed optically, the parallel search operation become extremely fast. The

feature is unique to holographic memories and has no analog in ordinary data storage system.

1.4 Optical Switching

The unprecedent speed and compact size of modern computers and communication systems heavily rely on the tremendous growth in semiconductor electronics and miniaturization technology. It is now possible to fit over 300 million transistors on a single silicon chip. The present transistor channel length has already shrunk below 100 nm. Further, it is estimated that by 2012 a CMOS or SiGe based chip will comprise almost 10^{10} transistors and will operate at speeds in the order of 10–15 GHz [86]. However, the main bottleneck in semiconductor driven technology will arise from limitations due to dielectric breakdown, hot carriers and short channel effects. Optical integrated circuits and optical interconnections are likely to provide a viable alternative to complexity inherent in conventional electronics. Optical systems have several advantages over their electronic counterparts. For example, low transmission loss, very high bandwidth, total immunity against electromagnetic noise and parallel processing capabilities make them ideal for future needs [87].

A switch is a means to release or establish a path for information flow in a communication channel. The main building block of any optical interconnections and integrated circuit is an optical switch. High-speed photonic switching which forms an essential component of optics based communication network and data processing systems can be realized using electro-optic, opto-mechanical, magneto-optic, and acousto-optic devices. An all–optical switching action can be accomplished by utilizing one optical pulse (pump beam) to control the transmission of a second optical pulse (signal or probe beam) by virtue of their interaction in a nonlinear media [88, 89]. All-optical switching eliminates the need to convert the photonic signal to electrical signal and vice-versa. The current rapid development of high-data-rate fiber-optic communication, and real-time information processing systems have created a need for an all-optical, ultra high-speed photonic switches [90]. Therefore, the requirement of appropriate nonlinear optical materials have gained a significance

role in present research.

Several nonlinear materials having fast response time, high stability and sensitivity at very low light intensity have been broadly investigated for their use in various molecular and photonic devices. These materials include nonlinear inorganic crystals [91,92], polymers [93,94], photorefractive organic compounds [95,96], dense media of two-level atoms [97], and photochromic biological molecules [98]. However, owing to its outstanding optical properties and excellent stability against chemical, thermal and photochemical degradation, bR is one of the most promising and widely studied biomaterial for photonic applications.

1.4.1 Bacteriorhodopsin

Bioelectronics is a subfield of molecular electronics that investigate the use of native as well as modified biological molecules (choromophores, protein etc.) in electronics and photonic devices. In recent years, several biological molecules have been intensively investigated for their use in electronics and photonic applications as an alternative to the existing silicon based devices [99]. The law of natural selection and evolution of biological molecules have conditioned them to perform certain tasks in most optimized and efficient ways. This is one of the main motivations to explore the suitability of these molecules in various photonic device applications.

Bacteriorhodopsin is one such protein molecule that is found in the trans-membrane cell of micro-organism called *Halobacterium hallobium*. This bacterium is usually found in hot and saline environment like sea water and marshland. The surface of *Halobacterium hallobium* contains membrane patches called the purple membrane. The purple membrane is built by replicating in space a hexagonal unit cell using periodic boundary conditions. The main function of bR is to convert light energy into metabolic energy by pumping a proton across the cell membrane whenever the ambient oxygen level goes low [100]. A process that is similar to photosynthesis.

Chemically extracted purple membrane can be easily cast into polymer films or 3D cuvette. The photochromic properties of bR provide the possibility of many applications in optical information processing and storage [82,83]. The use of bR has been proposed and demonstrated for variety of technological applications in optics

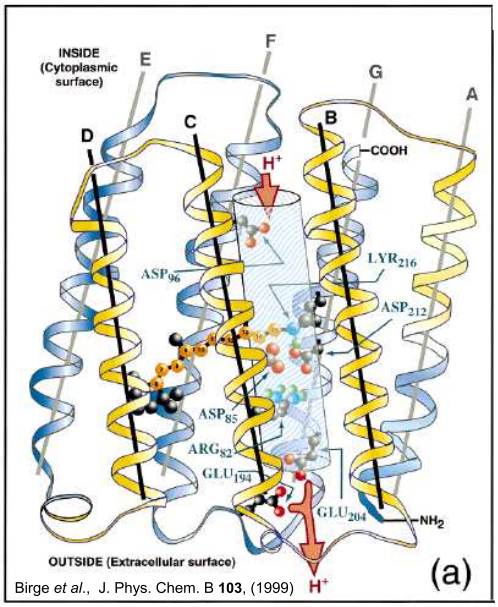

Figure 1.4: Molecular structure of bacteriorhodopsin.

that mainly include data storage [101–104], real–time holography [105], optical display and spatial light modulation [106, 107], optical image processing and nonlinear filtering [108, 109], neural networks [110], logic gates and optical switches [111, 112], applications based on intensity dependent refractive index changes [113, 114], interferometry [115], mode locking in lasers [116], phase conjugation and wave mixing in nonlinear optics [117, 118].

The bR molecule shows a remarkable stability against chemical and thermal degradation in harsh conditions like high temperature, exposure to excessive light fluxes for extended period and large variations in pH values.

1.4.2 Photo-response and Structure of bR

Bacteriorhodopsin is the only protein that is found in crystalline form in nature. It consists of single chain of 248 amino acids which are arranged in 7 helical bundles as shown in Figure 1.4. A light absorbing group called choromophore retinal is embedded inside the helix structure. This pigment converts light energy into chemical energy in a series of molecular events that finally result in migration of hydrogen ion (proton) from intracellular to extracellular side of the membrane. In absence of

any light, bR molecule remains stable in its ground state B, that has a broad absorption band in the visible region. A photocycle is initiated when the bR molecule absorbs a visible light photon around $\lambda \approx$ 570 nm. During the photocycle, molecules passes through several structural transformations states. These intermediates states were initially defined on the basis of time-resolved absorption spectroscopy and were labeled J, K, L, M_I, M_{II}, N, and O.

While in photocycle, bR molecule in a given state can either thermally relax to its neighboring intermediate or can be reverted directly back to B state if photoactivated by a light of suitable wavelength that falls within its absorption band. The phenomenon of photoinduced absorption changes and Kerr-type refractive index changes are the most relevant nonlinear processes that form the basis for almost all the envisaged applications of bR. The photochemical conversion of bR has been investigated and understood fairly well, but, the detailed determination of its structure and molecular mechanism still remains an active area of experimental research.

Chapter 2

Light-Induced Absorption and Wave-mixing in PR Crystals

2.1 Introduction

Photorefractive (PR) effects have been studied in many electro-optic materials. Several research efforts have been devoted for understanding and optimizing the material properties. $BaTiO_3$ and $LiNbO_3$ are two of the most important PR crystals, vastly subjected to experimental and theoretical investigations in past. These crystals belong to perovskite family of ABO_3 type compounds. In the pure or undoped form, both these crystals are electrical insulators. However, when doped with small amounts of impurities, they become semiconducting and their PR properties are significantly enhanced.

$BaTiO_3$ has very high value of electro-optic coefficients, fast response time and excellent phase conjugate reflectivity. Therefore, it is most suitable in applications like real-time holography or optical phase conjugation used in distortion correction in a time varying distortive media. The highest self-pumped phase conjugation reflectivity was reported in $BaTiO_3$ [119, 120]. It can be operated at visible and near-infared regions and is good for cw four-wave mixing with milliwatts optical power. Large electro-optic coefficient allows one to achieve very high gain in two-beam coupling and optical amplification [121].

$LiNbO_3$ is widely used PR material in optoelectronics. Owing to unique electro-

optical, photoelastic, piezo-electric and non-linear properties, a great variety of devices has been developed based upon this material. In addition, the crystal exhibits good mechanical and chemical stability and wide transparency range. The most commonly used dopant in $LiNbO_3$ is Fe^{2+}. It enters the lattice site as Fe^{2+} or Fe^{3+}. In PR process, the Fe^{2+} ions are occupied traps, and Fe^{3+} are empty traps. Beside this a number of other transition metal impurities have also been used for doping. The control both intrinsic defects and impurities offer a wide range of crystal responses. A long storage time, bigger size, large photorefractive sensitivity, broad spectral range and high diffraction efficiency –make $LiNbO_3$ as one of the most attractive material for data storage and photonic applications.

Some of the important physical properties of the two crystals are listed in Table 2.1. The exact values of these properties may vary depending on the concentrations of impurities and other defects [36].

Table 2.1: Some of the important physical properties of the $BaTiO_3$ and $LiNbO_3$ crystals.

Properties	$BaTiO_3$	$LiNbO_3$
Crystal Symmetry	Tetragonal, 4mm	Trigonal, 3m
Lattice Parameters	a=3.992 , c=4.036	a=5.148, c= 13.863
Curie Temp.	-90°C, 9°C, 130°C	1140°C
Density	6.02 gcm^{-3}	4.64 gcm^{-3}
Refractive Index[1]	n_o=2.42, n_e=2.36	n_o=2.29, n_e=2.20
$\Delta n_{\max}$	$10^{-5} - 10^{-3}$	$\approx 10^{-4}$
Dielectric Constant	ϵ_a =3700, ϵ_c =135	ϵ_a =85, ϵ_c =29.5
Non-zero Electro-optic Coefficients[2](pmV^{-1})	r_{13}=19.5, r_{33}=97, r_{42}=1640	r_{33}=30.8, r_{31}=8.6, r_{22}=3.4, r_{51}=28

The phenomenon of light-induced absorption (LIA) and optical wave-mixing in PR materials are well known. The PR effects have been successfully explained by the band-transport model. The relevant features of band-transport model are outlined in section 2.2. The theory of LIA is given in section 2.3. The steady-state and temporal measurements of LIA and two-wave mixing (TWM) in a pure and rhodium (Rh) doped $BaTiO_3$ crystal have been carried out at different wavelengths and intensities of laser light. Experimental results for LIA and TWM are presented

[1] at λ=633 nm

[2] unclamped

in section 2.5. The observed behavior is interpreted in terms of a two-center charge transport model for PR materials. Various model parameters like build-up and decay rates, thermal excitation rates, and two-wave coupling gain have been obtained. The diffraction efficiency measurements and grating erasure studies in triply-doped (Fe:Ti:Ce) $LiNbO_3$ crystals are presented in the last.

2.2 Band-Transport Model

The presence of impurity ions –also called primary or deep centers, is believed to be responsible for the PR effect in inorganic crystals. These impurities are generally transition metal-ions which occur in different valence states. The energy level of such impurities is located in the gap of valence and conduction band. Typical excitation energy for deep centers is $\gtrsim$ 1eV. Therefore, the thermal excitation rate for primary centers is almost negligible. A simplified version of Kukhtarev's model [12] based on single carrier primary centers is shown in Figure 2.1(a). The primary centers are designated by X/X^+, where X/X^+ can be Fe, Cr, Mn, Cu, Co, Ce, Mg or any other ionized impurity in mixed-valence states. This model satisfactorily explains the PR effect in most of the cases. However, it fails to explain the sub-linear dependence of the two-beam coupling coefficients and typical nonlinear dependence of photoconductivity and absorption coefficients at higher intensities in $BaTiO_3$ crystals. Increase in absorption due to illumination of $BaTiO_3$ was first discovered in 1987 by Motes and Kim [23]. In 1988 Brost *et al.* explained this effect by a two-center charge transport model [24].

A two-center model postulates the existence of secondary photorefractive centers (also called shallow traps) that can account for most of these intensity-dependent effects. Figure 2.1(b) shows 2-center model involving two species; X/X^+ as primary centers and Y/Y^+ as secondary centers that are responsible for light-driven charge transfer processes. The existence of shallow traps was confirmed by several experiments using two-wave mixing and light-induced absorption in $BaTiO_3$ [122–125].

To investigate and understand the characteristics of primary and secondary impurities is important both for theory and applications. However, to identify the im-

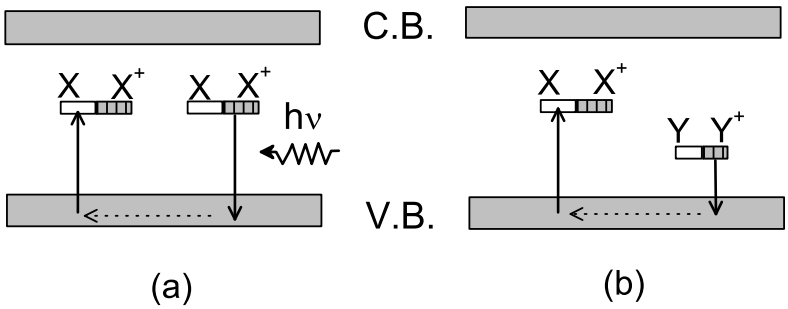

Figure 2.1: Two basic models for charge transfer processes in *p*-type PR crystals. (a) 1-center model with deeply imbedded impurities and (b) 2-center model with deep and shallow impurities.

purity defects that are responsible for PR and light-induced effects is not straightforward. Different methods like measurement of photo-conductivity, temperature and light-induced absorption studies, electron spin resonance (ESR) spectrum and linear absorption spectrum can reveal the information of shallow traps.

2.3 Light-induced Absorption

Light-induced absorption is characterized by the increase in absorption coefficient with laser intensity. It can be induced by uniformly illuminating the crystal with strong pump beam at one wavelength and observed by monitoring the transmission of a weak probe beam through the crystal at different wavelength. It has already been shown that intensity-dependent absorption is consistent with two-center charge transport model [24]. It is based on the assumption that two different impurity centers, each of them occurring in different valence states, are present. The first is deep and second is shallow with respect to the valence band edge. Figure 2.2 shows two-center energy level diagram for *p-tpye* crystal, where, holes are the dominant charge carriers. $N_1\,(N_1^+)$ and $N_2\,(N_2^+)$ are the densities of the empty (filled) deep

and shallow impurities respectively. Whereas, $N_{1T} = N_1 + N_1^+$ and $N_{2T} = N_2 + N_2^+$ are the total deep and shallow center densities. The rate equations governing the

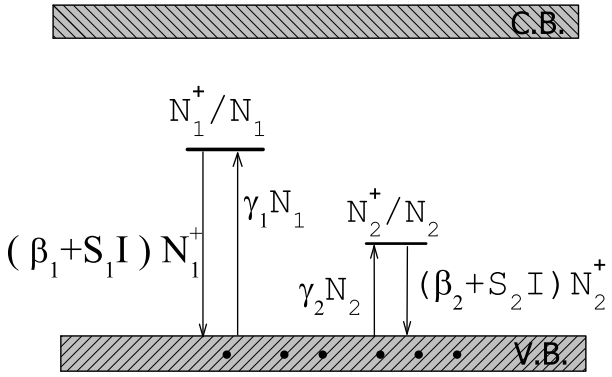

Figure 2.2: Energy level diagram for two-center model in *p-type* $BaTiO_3$ crystal.

charge transport for the deep and shallow levels are [24]:

$$\frac{dN_i^+}{dt} = -(S_i I + \beta_i)N_i^+ + \gamma_i(N_{iT} - N_i^+)n_h, \tag{2.1}$$

$i = 1, 2$

where S is photon-absorption cross section,γ is recombination coefficient, β is thermal ionization rate, I is the laser intensity and n_h is free carrier (hole) density. Subscript $i = 1, 2$ refers to deep and shallow levels respectively. Illuminating the crystal with laser light causes photo-ionization and redistribution of the charges between deep and shallow traps. This results in light-induced absorption change:

$$\Delta\alpha = \sum_{i=1,2} S_i[N_i^+ - N_i^+(0)], \tag{2.2}$$

where $N_i^+(0)$ is dark concentration of filled traps. The charge conservation requires:

$$\sum_{i=1,2} N_i^+ + n_h = N_c, \tag{2.3}$$

where N_c is the density of compensating charge centers that do not participate in PR effect, but required to maintain overall charge neutrality of the crystal. The hole concentration in Eq. (2.3) can be ignored as it remains small compared to the impurity concentration [122]. In the *steady-state* condition, $dN_i^+/dt = 0$, therefore solving Eqs. (2.1)–(2.3) we get,

$$\Delta\alpha = \sum_{i=1,2} S_i[N_i(1 - \frac{S_i I + \beta_i}{\gamma_i A}) - N_i^+(0)], \tag{2.4}$$

where

$$A = \frac{N_1\gamma_2(S_1 I + \beta_1) + N_2\gamma_1(S_2 I + \beta_2)}{(N_1 + N_2 - N_c)\gamma_1\gamma_2}, \tag{2.5}$$

Time evolution of the light-induced absorption in the build up process can be described by [123]:

$$\Delta\alpha(t) = [1 - \exp(t/\tau)], \tag{2.6}$$

$$\tau^{-1} = S_2 I + \beta_2 + \gamma_2 n_h, \tag{2.7}$$

Because of the approximate proportionality between n_h and I, Eq. (2.7) can be rewritten as,

$$\tau^{-1} = aI + \beta_2, \tag{2.8}$$

where a is a factor that is independent of intensity. Eq. (2.8) can be used to determine the thermal excitation rate β_2.

2.4 Two-wave Mixing

A nonuniform illumination is one of the necessary conditions to form space-charge field in a PR medium. Two coherent laser beams as shown in Figure 2.3, are used for creating interference pattern inside the crystal.

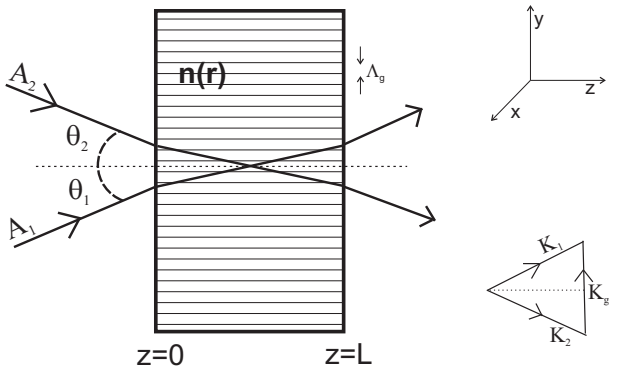

Figure 2.3: The formation of refractive index grating using two-beam interference in PR crystals.

The electric field associated with two beams can be written as,

$$E_{1,2} = A_{1,2} \exp[i(\omega t - k_{1,2} \cdot r)] \tag{2.9}$$

where, A_1 and A_2 are beam amplitudes and ω is angular frequency of the light. The resulting interference pattern can be expressed as,

$$\begin{aligned} I &= |E|^2 = |E_1 + E_2|^2 \\ &= I_0 + I_1 \cos(K_g \cdot r) \qquad (2.10) \\ \text{where} \qquad I_0 &= |A_1|^2 + |A_2|^2 \quad \text{and} \quad I_1 = 2A_2A_1^* \qquad (2.11) \end{aligned}$$

Here $\mathbf{K_g} = \mathbf{k}_1 - \mathbf{k}_2$ is the grating wave vector determined by $\mathbf{k}_1$ and $\mathbf{k}_2$ wave vectors of corresponding beams. Photo-excitation and migration of free charges from brighter region to darker region leads to development of internal space-charge field E^{sc} which is given by [126]:

$$E^{\text{sc}} = i \frac{\frac{k_B T}{q} K}{1 + K^2/K_D^2} m \cos(Kz) \qquad (2.12)$$

where $K_g = |\mathbf{K_g}| = 2\pi/\Lambda_g$ is the magnitude of the grating wave vector, $m = I_1/I_0$ is the intensity modulation index (also known as fringe contrast) and $K_D^2 = q^2 N_C/\epsilon\, k_B T$ is the Debye wave number. The presence of i in Eq. (2.12) indicates a $\pi/2$ phase shift between the intensity pattern and the space-charge field. This phase shift is responsible for the energy coupling that is generally observed in two-wave mixing process in $BaTiO_3$ crystals. The amplitude of space-charge field which causes the PR effect depends only on the intensity modulation index m and not on the total illumination intensity. Additionally, we also note that the space-charge field reaches maximum when $K = K_D$. This fact we can be used to make experimental estimation of acceptor density N_C.

The refractive index grating formed by two-beam interference pattern can be expressed as [38]:

$$n = n_0 + \frac{m}{4} [n_1 \exp[i(\phi - K_g.r)] + \text{c.c.}] \qquad (2.13)$$

where n_0 is uniform refractive index in the absence of light, n_1 is real constant related to maximum index change, $m = I_1/I_0$ is the fringe contrast, ϕ is the phase shift between index grating and light interference pattern. The presence of non-zero phase shift ϕ allows the nonreciprocal energy transfer between the beams.

2.4.1 Electro-Optic Effect in PR Crystals

Two-beam interference pattern described by Eq. (2.10) results in charge segregation between darker and brighter fringes which lead to formation of periodic space-charge field in a PR material. How the space-charge field, in turn, modulates the refractive index of the material via electro-optic effect is explained next.

The propagation of electromagnetic waves in a homogenous medium is completely described by Maxwell's equations [127]:

$$\nabla \cdot \mathbf{D} = \rho \tag{2.14}$$

$$\nabla \cdot \mathbf{B} = 0 \tag{2.15}$$

$$\nabla \times \mathbf{E} = -\frac{\partial \mathbf{B}}{\partial t} \tag{2.16}$$

$$\nabla \times \mathbf{H} = \mathbf{J} + \frac{\partial \mathbf{D}}{\partial t} \tag{2.17}$$

where $\mathbf{E}$ is the electric field vector, $\mathbf{H}$ is the magnetic field vector, $\mathbf{B}$ is the magnetic induction vector, and $\mathbf{D}$ is the electric displacement vector, ρ is the charge density, and $\mathbf{J}$ is the current density. For a nonmagnetic material medium, the field vectors are related by,

$$\mathbf{D} = \epsilon_0 \mathbf{E} + \mathbf{P} \tag{2.18}$$

$$\mathbf{B} = \mu_0 \mathbf{H} \tag{2.19}$$

where $\mathbf{P}$ is the electric polarization of the medium, ϵ_0 the dielectric permittivity, and μ_0 the permeability of the vacuum.

As stated earlier in section 1.1, when electric filed is small compared to intra-atomic field, the electric polarization vector $\mathbf{P}$ is written as,

$$\mathbf{P} = \epsilon_0 \chi^{(1)} \mathbf{E} \tag{2.20}$$

Substituting Eq. (2.20) into Eq. (2.18) gives

$$\mathbf{D} = \epsilon_0(1 + \chi^{(1)})\mathbf{E} \tag{2.21}$$

$$\text{or} \quad \mathbf{D} = \epsilon \mathbf{E} \tag{2.22}$$

where $\epsilon = \epsilon_0(1 + \chi^{(1)})$ is the dielectric permittivity or the dielectric constant of the medium. For anisotropic media, ϵ is a tensor of rank two, whose coefficient are the

elements of a 3×3 matrix. In the principal coordinate, the dielectric tensor has a simplified diagonalized form:

$$\epsilon = \begin{pmatrix} \epsilon_x & 0 & 0 \\ 0 & \epsilon_y & 0 \\ 0 & 0 & \epsilon_z \end{pmatrix} = \epsilon_0 \begin{pmatrix} n_x^2 & 0 & 0 \\ 0 & n_y^2 & 0 \\ 0 & 0 & n_z^2 \end{pmatrix} \tag{2.23}$$

where ϵ_x, ϵ_y, ϵ_z are the principal dielectric constants and n_x, n_y, n_z are principal indices of refraction. The permittivity tensor contains information about how the phase velocity of light waves in nonlinear material varies with the direction of propagation and the polarization of the wave. The energy density associated with an electromagnetic wave is given by [128]:

$$U = \frac{1}{2}\, \mathbf{E} \cdot \mathbf{D} \tag{2.24}$$

Therefore, in the principal axis system Eq. (2.23) becomes:

$$\begin{pmatrix} D_x \\ D_y \\ D_z \end{pmatrix} = \epsilon_0 \begin{pmatrix} n_x^2 & 0 & 0 \\ 0 & n_y^2 & 0 \\ 0 & 0 & n_z^2 \end{pmatrix} \begin{pmatrix} E_x \\ E_y \\ E_z \end{pmatrix} \tag{2.25}$$

so that

$$U = \frac{1}{2} \left(\frac{D_x^2}{\epsilon_0\, n_x^2} + \frac{D_y^2}{\epsilon_0\, n_y^2} + \frac{D_z^2}{\epsilon_0\, n_z^2} \right) \tag{2.26}$$

This equation has the form of an ellipsoid in (D_x, D_y, D_z) coordinates. We can express Eq. (2.26) in the normalized coordinate form as,

$$\frac{x^2}{n_x^2} + \frac{y^2}{n_y^2} + \frac{z^2}{n_z^2} = 1 \tag{2.27}$$

where $x = D_x/\sqrt{2\epsilon_0\, U}$, $y = D_y/\sqrt{2\epsilon_0\, U}$, and $z = D_z/\sqrt{2\epsilon_0\, U}$. Equation (2.27) is known as *index ellipsoid* or *optical indicatrix*. By solving Maxwell's equations for anisotropic media ($\nabla \cdot \mathbf{E} \neq 0$), it can be shown that for any direction of propagation, the medium can support two modes of linear polarizations of light which are orthogonal to each other. The refractive index for the two polarization modes depends upon the direction of propagation. The index ellipsoid also tells us what magnitude and direction of the $\mathbf{D}$ vector must be in order for a wave propagating in a crystal characterized by n_x, n_y, n_z to have an energy density U.

In general, any optical material may fall into one of the three categories, namely,

1. optically isotropic: $n_x = n_y = n_z$
2. uniaxial: $n_x = n_y = n_o$ ordinary index
   $n_z = n_e$ extraordinary index
3. biaxial: $n_x \neq n_y \neq n_z$

Uniaxial crystals are characterized by an unique direction called *optic axis* or c-axis. A ray propagating along optic axis will have same refractive index (n_o) regardless of its polarization. Propagation along any other direction results in o-ray and e-ray having refractive indices n_o and n_e, respectively. The polarization vector for o-ray is perpendicular to the plane containing ray propagation vector **K** and c-axis of the crystal. On the other hand, for e-ray, the polarization vector lies in the plane defined by propagation vector and c-axis and the refractive index is function of angle θ between **K** vector and c-axes:

$$\frac{1}{n_e^2(\theta)} = \frac{\sin^2\theta}{n_e^2} + \frac{\cos^2\theta}{n_o^2} \tag{2.28}$$

Biaxial crystals on the other hand have two optic axis.

In anisotropic crystals, the application of applied electric field can cause a change in dialectic tensor ϵ, and in turn change the refractive index of the medium. This is generally known as the electro-optic effect or Pockel's effect. In PR crystals, the static electric field is produced internally by photo-excitation as explained in previous section. The presence of electric field also modifies the index ellipsoid given by Eq. (1.27) and it no longer remains in principal coordinate system. A new set of principal axis can be found to obtain the principal indices of refraction by appropriate coordinate transformations. In general, the electro-optic effect due to electric field can be expressed as [38]:

$$\Delta\left(\frac{1}{n^2}\right)_{ij} = \sum_{k=1}^{3} r_{ijk}\, E_k^{\mathrm{sc}} \tag{2.29}$$

where E_k^{sc} is the component of space-charge field along kth direction and r_{ijk} is electro-optic coefficients of third rank tensor that has 27 components. Not all the 27 components of the tensor are independent. The permutation symmetry of the two indices i and j, i.e., $r_{ijk} = r_{jik}$, reduces the independent elements to 18.

Depending upon the point group symmetry of the crystal, the number of independent components of electro-optic tensor are further reduced. $LiNbO_3$ and $BaTiO_3$ crystals used in this work, belong to *trigonal* and *tetragonal* class with point group symmetry of $3m$ and $4mm$, respectively. The electro-optic coefficients for $LiNbO_3$ (8 non-zero elements) and $BaTiO_3$ (5 non-zero elements) crystals are listed in Eq. (2.30).

$$\begin{bmatrix} 0 & -r_{22} & r_{13} \\ 0 & r_{22} & r_{13} \\ 0 & 0 & r_{33} \\ 0 & r_{51} & 0 \\ r_{51} & 0 & 0 \\ -r_{22} & 0 & 0 \end{bmatrix} \text{ and } \begin{bmatrix} 0 & 0 & r_{13} \\ 0 & 0 & r_{13} \\ 0 & 0 & r_{33} \\ 0 & r_{42} & 0 \\ r_{42} & 0 & 0 \\ 0 & 0 & 0 \end{bmatrix} \tag{2.30}$$

The refractive index change Δn can be written as,

$$\Delta n = -\frac{1}{2}\, n^3 \left\langle \hat{p} \left| \Delta\left(\frac{1}{n^2}\right) \right| \hat{p} \right\rangle \tag{2.31}$$

where n is the uniform refractive index of the medium and $\hat{p}$ is the polarization vector of incident light. The refractive index change depends on the crystals symmetry, the direction of space-charge field, polarization state of light and the appropriate combination of electro-optic coefficients. This can be illustrated by taking the example of $LiNbO_3$ crystal. The space-charge field for a grating wave vector parallel to z-axis can be written as, $\mathbf{E}^{\mathrm{SC}} = [0 \;\; 0 \;\; 1]^T E^{\mathrm{sc}} \cos(Kz)$, where superscript T denotes transpose of the vector. Let the light be polarized along y-direction, i.e., $\hat{p} = [0\ 1\ 0]^T$. After substituting Eq. (2.29) in Eq. (2.31), the expression for refractive index change becomes:

$$\Delta n = -\frac{1}{2}\, n^3\, r_{13}\; E^{\mathrm{sc}} \cos(Kz) \tag{2.32}$$

To optimize Δn for the index grating requires a proper combination of the orientation of the c-axis and the polarization of the light to yield largest electro-optic coefficient in Eq. (2.32).

2.4.2 Energy Coupling in TWM

A $\pi/2$ phase shift between refractive index grating and illuminating interference pattern leads to energy transfer from one beam to another. This happens because

the phase grating diffracts each beam in direction of other with additional phase shift of $\pm\pi/2$. In one case, diffracted beam interferes destructively ($\pi/2+\pi/2=\pi$) with transmitted beam thereby diminishing the intensity, in other, a constructive interference ($\pi/2$-$\pi/2$=0) between diffracted and transmitted beam leads to increase in energy. For the appropriate orientation of the crystal, the signal beam I_s experiences a gain at the cost of pump beam I_p. Transmission of the signal beam after traversing the crystal length L is given by [36]:

$$\frac{I_s(L)}{I_s(0)} = \frac{[I_s(0) + I_p(0)]\exp[(\Gamma - \alpha)L]}{I_p(0) + I_s(0)\exp(\Gamma L)}, \tag{2.33}$$

The beam coupling gain Γ is defined as,

$$\Gamma = 4\pi^2 \frac{n^3 k_B T}{q\lambda} \frac{\Lambda_d}{\Lambda_d^2 + \Lambda_o^2} r_{\text{eff}}, \tag{2.34}$$

where Λ_d, k_B, T, q, λ are grating period, Boltzmann constant, temperature, electronic charge and light wavelength respectively, and

$$\Lambda_o = \frac{2\pi}{q}\left[\epsilon\epsilon_o \frac{k_B T}{N_E}\right]^{1/2}, \tag{2.35}$$

is Debye screening length, $N_E = NN^+/(N + N^+)$ is effective trap density and ϵ is dielectric constant. Experimentally the photorefractive gain γ_o as measured in laboratory is given by,

$$\gamma_o = \frac{I_s(L)\text{with pump beam on}}{I_s(L)\text{with pump beam off}} \tag{2.36}$$

Therefore, the measurement of γ_o along with Eq. (2.33) provides a direct means of determining Γ. The effective trap density N_E can be estimated using Eq. (2.35), by noting that beam coupling gain Γ in Eq. (2.34) is maximum when $\Lambda_o = \Lambda_d = \lambda/\sin\theta$.

The time constants involved in the grating build up and decay are also important parameters in evaluating the figure-of-merit of photorefractive crystals. Kukhtarev has given a complete analysis of the dynamics of grating formation and decay for continuous wave illumination [12]. Time required to write a refractive index grating depends on the efficiency of charge generation and transport mechanism. A simple expression for the time dependence of space-charge field during the the grating recording is given by,

$$\Delta E^{sc} = mE^{sc}[1 - \exp(-t/\tau_{\text{eff}})], \tag{2.37}$$

Similarly a grating erasure can be accomplished by uniform illumination of the crystal. The decay of space-charge field during the erasure process can be written as,

$$\Delta E^{sc} = I E_o^{sc} \exp(-t/\tau_{\text{eff}}), \tag{2.38}$$

where E^{sc} is the initial amplitude and E_o^{sc} is maximum amplitude of the space-charge field obtained in steady-state, I is the irradiance of erasing beam, m is fringe contrast factor and τ_{eff} is the effective time constant for the crystal response. As in the case of LIA, the τ_{eff} can have multiple components due to the presence of different impurity traps in the crystal. In general the value of τ_{eff} may be a function of different parameters like pump and signal beam intensity, light wavelength, intensity modulation index m, and dark conductivity etc.

2.4.3 Light Diffraction by Volume Grating

The modulated photorefractive space-charge electric field leads to a modulated refractive index grating by means of the electro-optic effect discussed in previous section. If the material is sufficiently thick and the grating modulation is large enough, then such a grating can efficiently diffract a light wave provided that its direction satisfies Bragg phase matching. Upon diffraction from the periodic grating, the Bragg's condition requires that the change of light wave vector be exactly equal to an integral number of grating wave vector i.e., $2k \sin\theta = N K_g$.

For perfect phase matching, i.e., $\theta_1 = -\theta_2 = \theta$, the fraction of power that is transferred into the diffracted beam is given by [12]:

$$\eta_{\text{diff}} = \frac{I_{\text{diffracted}}}{I_{\text{incident}}} = \sin^2\left(\frac{\pi \Delta n\, d}{\lambda \cos\theta_B}\right) \tag{2.39}$$

where d is the thickness of the grating and θ is half-angle between the two beams inside the crystal.

2.5 Experiments and Results

2.5.1 LIA in Undoped and Rh-doped $BaTiO_3$ Crystal

Light-induced absorption was studied in 0°-cut undoped and Rh-doped $BaTiO_3$ crystals. The respective dimensions of crystals ($c \times a \times a$) were, 6.72 × 6.28 × 5.5 mm and 6.6 × 5.8 × 4.2 mm. Change in absorption can be induced at one wavelength

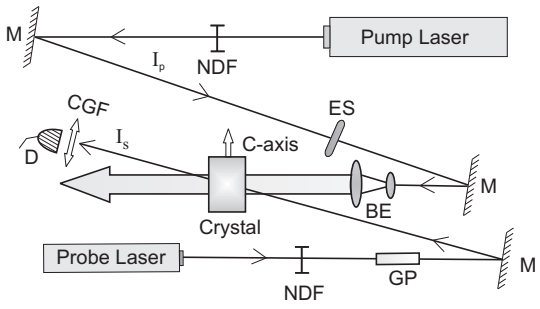

Figure 2.4: Schematic of the experimental setup: M's, mirrors; NDF, neutral density filter; ES, electro-mechanical shutter; GP, Glan laser polarizer; D, detector; BE, beam expander; CGF, colour glass filter; I_p, pump beam; I_s, probe beam.

and observed at different wavelengths. This helps to eliminate the possibility of beam coupling effects that can rise if both beams are coherent. Figure 2.4 shows the schematic for the experimental set-up. An expanded pump beam I_p at wavelength λ_p illuminates the crystal, whereas, a weak signal beam I_s at different wavelength λ_s acts as a probe to study the change in absorption. Pump and probe beam light that used in LIA measurements are listed in Table 2. The small beam-crossing angle

Table 2.2: Light wavelengths and sources used in LIA measurements.

	Wavelength	Source	Model
Probe(λ_s)	633 nm	He-Ne	05-LHR-151; Melles Griot
	543 nm	He-Ne	1208-2; JDS Uniphase
	750 nm	Ti: sapphire	3900S; Spectra-Physics
	800 nm	Ti: sapphire	3900S; Spectra-Physics
Pump(λ_p)	488 nm	Argon-ion	BeamLok^{TM} 2085; Spectra-Physics
	514 nm	Argon-ion	BeamLok^{TM} 2085; Spectra-Physics

($\approx 10°$ ensures a complete and uniform overlap of the beams inside the crystal. The

diameter of the probe beam inside the crystal was ≈ 2 mm. The intensity of the pump beam was varied from $\sim 3\mu\text{Wcm}^{-2}$ to 16 Wcm^{-2} using compensated neutral density filter (Model: 925B; Newport). Pump beam illumination was controlled using electro-mechanical shutter. The transmission of the probe was monitored using computer controlled optical power meter (Model: 4832-C Multichannel Optical Power Meter; Newport).

Both the beams were made o-polarized to minimize the beam fanning and scattering effects which otherwise could be mistaken for absorption. Appropriate colour glass filters along with a small pin hole was used to prevent the scattered light from pump beam entering the detector. Transmission of probe beam was monitored after switching *on* the pump beam at t_0. Figure 2.5(a) shows the transmission of the probe through undoped $BaTiO_3$ crystal as a function of time. Photo-induced change

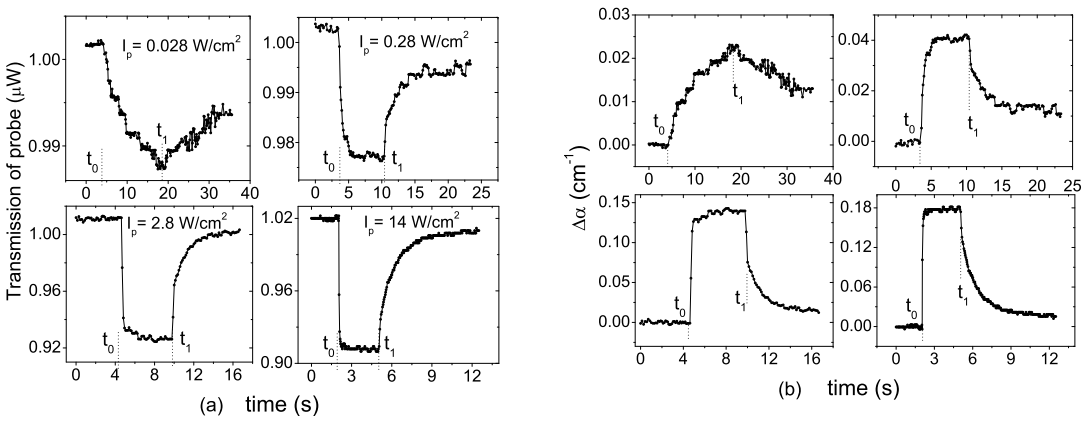

Figure 2.5: (a) Probe beam transmission ($\lambda_s = 633$ nm) through undoped $BaTiO_3$ crystal when illuminated by pump at 514 nm at different intensities and, (b) corresponding LIA change.

in absorption coefficient $\Delta\alpha$ is determined using the relation:

$$\frac{I_s(\text{with } I_p \text{ on})}{I_s(\text{with } I_p \text{ off})} = \exp(-\Delta\alpha L), \tag{2.40}$$

where L is the effective length of the crystal, I_s and I_p are probe and pump beam intensities, respectively. The typical dynamics of LIA is characterized by absorption rise, steady-state and dark-decay. The temporal evolution of LIA change calculated using Eq. (2.40) is shown in Figure 2.5(b).

Absorption build-up curves for both the crystals (e.g. region between t_0 and t_1 in Figure 2.5(b)) follow mono-exponential rise as described by Eq. (2.6). Rise time constant τ was calculated by fitting the experimental data with Eq. (2.6). Figure 2.6 shows the plot of absorption rise time versus intensity of the pump beam. Measure-

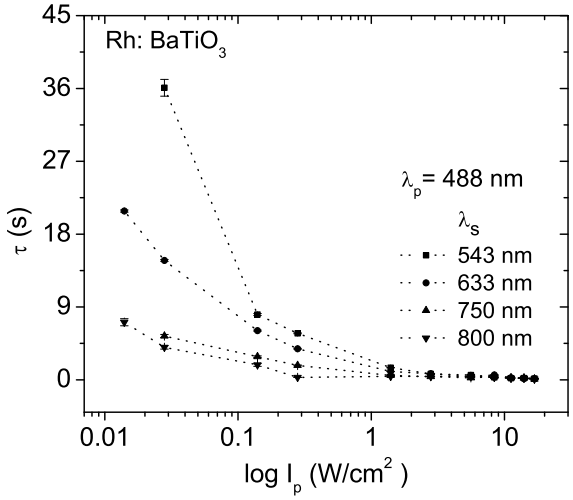

Figure 2.6: Absorption rise time constant τ versus pump beam intensity for Rh:$BaTiO_3$.

Table 2.3: Crystal parameters that best fit the experimental results

Undoped $BaTiO_3$				Rh: $BaTiO_3$		
$N_{1T}=7.0\times10^{16}$ cm^{-3}; $N_1^+(0)=6.9\times10^{16}$ cm^{-3};				$N_{1T}=2.6\times10^{18}$cm^{-3}; $N_1^+(0)=2.57\times10^{18}$cm^{-3};		
$N_{2T}=$ 4.0×10^{16} cm^{-3}; $N_2^+(0)=8\times10^{11}$ cm^{-3};				$N_{2T}=$ 8.0×10^{17}cm^{-3}; $N_2^+(0)=3.8\times10^{14}$cm^{-3};		
$n_h(0)=1.0\times10^6$ cm^{-3}; $\gamma_1=3\times10^{-8}$ cm^{3}s^{-1};				$n_h(0)=$ 8.0×10^5cm^{-3}; $\gamma_1=5\times10^{-8}$cm^{3}s^{-1};		
$\gamma_2=1\times10^{-8}$ cm^{3}s^{-1}; $\beta_1=8\times10^{-3}$s^{-1}				$\gamma_2=2.8\times10^{-8}$cm^{3}s^{-1}; $\beta_1=1.5\times10^{-4}$s^{-1}		
λ_s(nm)	$S_1\times10^{-17}$cm^2	$S_2\times10^{-16}$cm^2	β_2(s^{-1})	$S_1\times10^{-17}$cm^2	$S_2\times10^{-16}$cm^2	β_2(s^{-1})
543	7.0 (2.2)	1.6 (1.0)	10 (5)	5.2 (6.0)	7.0 (4.2)	1.0 (3.2)
633	7.4 (2.2)	1.3 (3.0)	10 (5)	5.3 (2.0)	8.0 (1.4)	0.2 (0.04)
750	1.7 (2.8)	1.0 (2.8)	10 (5)	8.5 (3.0)	3.3 (6.5)	0.1 (0.1)

Note: λ_p = 488 nm (514 nm)

ments of the steady-state LIA changes at different pump and probe wavelengths for both the crystals have also been carried out. The steady-state absorption change $\Delta\alpha$ for the two crystals at different probe wavelengths as a function of I_p is shown in Figure 2.7. Experimental data is represented by the symbols, whereas, the solid lines are theoretical curves calculated using Eq. (2.4). Crystal parameters that best fit our data are given in Table 2.3. Main results are summarized:

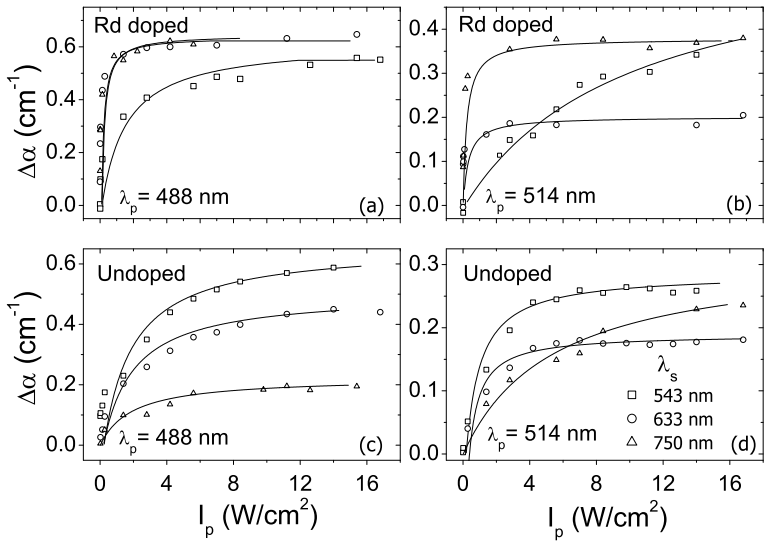

Figure 2.7: Steady-state light-induced absorption change $\Delta\alpha$ versus pump beam intensity at different probe wavelengths. (a)–(b) for Rh-doped and (c)–(d) for undoped $BaTiO_3$ crystal.

- ◇ For both crystals, the absorption cross-section $S(488\,\text{nm}) > S(514\,\text{nm})$. Therefore, the magnitude of the absorption change caused by 488 nm pump is more than the 514 nm pump.

- ◇ Unlike in undoped $BaTiO_3$, $\Delta\alpha$ for Rh:$BaTiO_3$ was found to increases with increases in probe wavelengths, indicating the different origin of secondary centers in both the crystals.

- ◇ The thermal excitation rates β_2 calculated using Eq. (2.8), were found to be $0.1-0.3$ and $0.5-0.6$ sec^{-1} for Rh-doped and undoped $BaTiO_3$ crystals respectively. These values are considerably smaller than the results reported by Brost *et al.* [24] and Buse and Bierwirth [122].

- ◇ As per the theory of LIA described in Ref. [122] and the fact that thermal ionization rate β_2 for undoped crystal is relatively higher than Rh:$BaTiO_3$, the pump beam intensity at which the absorption saturates is higher (see Figure 2.7) for undoped $BaTiO_3$ than the Rh-doped crystal.

Anomalous Absorption in Rh:$BaTiO_3$

A wavelength specific anomalous absorption as shown in Figure 2.8(a), was observed in Rh-doped $BaTiO_3$ crystal [129]. After the pump beam was turned on at $t = t_0$, an unexpected fall in absorption could be noticed in beginning, which is then followed by usual absorption rise. Contrary to the behaviour shown in Figure 2.5(b), a further increase in absorption was observed even after the pump beam was blocked at $t = t_1$.

For clarity, the magnitude of this additional absorption change is denoted by δ and δ' in the Figure 2.8(a). Dependence of δ and δ' on pump intensity is plotted in Figure 2.8(b). A linear change in δ is observed up to $\sim$0.23 Wcm^{-2}, beyond which it remains almost constant and again falls at higher intensities. The anomalous absorption in Rh:BaTiO3 seen only at the 633 nm probe and 514 nm pump, has not been reported earlier.

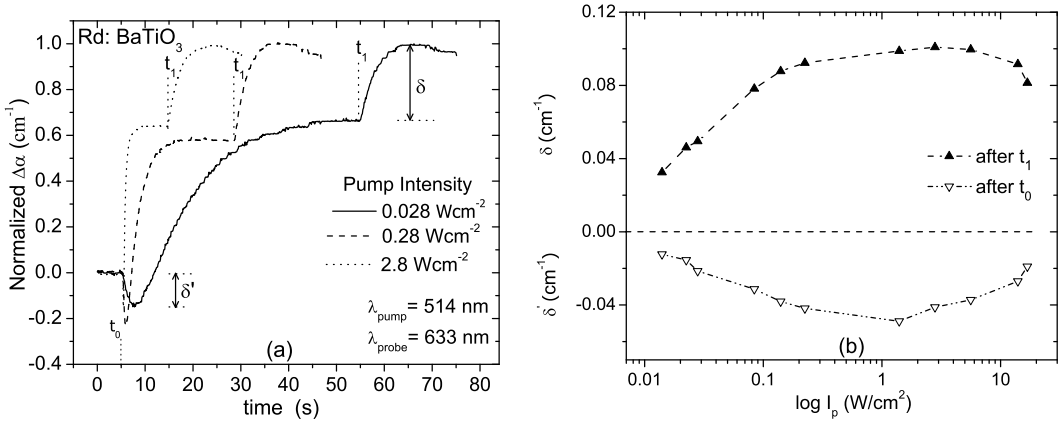

Figure 2.8: (a) Temporal evolution of anomalous absorption change in Rh:$BaTiO_3$ and (b) plot of anomalous absorption variations versus I_p .

The physical mechanism responsible for this particular behavior is not very clear. But, it is speculated that immediately after the pump beam is turned on, a gradual rise in temperature causes an increase in the thermal excitation rate of the secondary traps. Therefore, the number density of available filled traps that can absorb probe photons is also reduced. This results in decreases in absorption as shown in the Figure 2.8. The decline in absorption continues for sometime until a thermal equilibrium is attained within the crystal. Similarly, an increase in ab-

sorption after blocking the pump beam is a consequence of the drop in the thermal excitation rate of the secondary traps. Temperature-dependent absorption studies in past have shown that rise in temperature may cause decrease in absorption and vice-versa [125, 130]. However, there is no strong evidence against the possibility of wavelength-specific crystal defects which could possibly lead to similar results.

Absorption Decay

The dark-decay of LIA is associated with the loss of shallow and deep trap population by thermal ionization. In general, the dark decay process of LIA can be described by a double exponential function as,

$$\Delta\alpha(t) = a_0 + a_1 \exp(-t/\tau_1) + a_2 \exp(-t/\tau_2), \tag{2.41}$$

where τ_1 and τ_2 are the fast and slow decay time constants, respectively. A typical

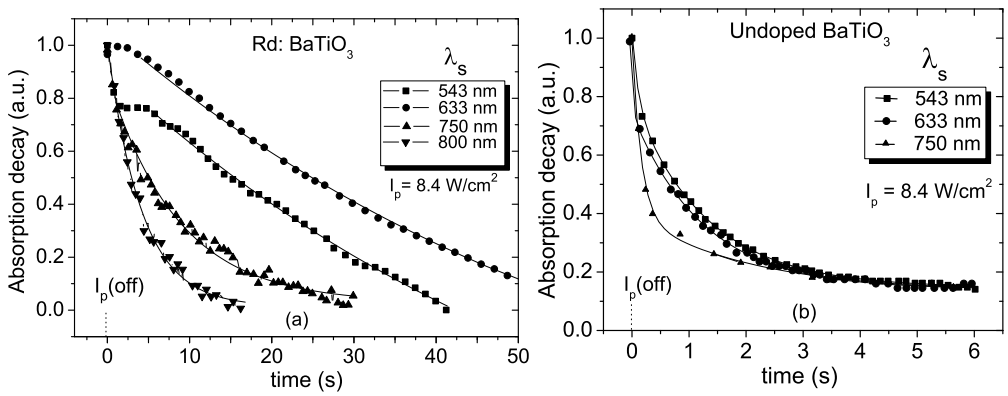

Figure 2.9: Typical dark-decay process of light-induced absorption change observed at 488 nm pump and different probe wavelengths (a) for Rh:$BaTiO_3$ and (b) for undoped $BaTiO_3$. The symbol refers to measured results and solid curves are exponential fit to the experimental data.

dark-decay of $\Delta\alpha$ (normalized to it's maximum value) after blocking the pump beam at $t = 0$ is shown in Figure 2.9. From the dark decay measurements of LIA in Rh-doped $BaTiO_3$, it can be noticed that the dark decay process, at 543 nm probe and 488 nm pump, occurred in two separate steps. It showed an initial fast relaxation having two time constants $\tau_1 \sim 50$ ms and $\tau_2 \sim 0.7$ s, followed by a slow

relaxation with longer time constant ~ 60 s. At 633 nm probe wavelength, a slow mono-exponential decay with $\tau_2 \sim 62$ s alone was observed. Decay at wavelengths 750 nm and 800 nm was again found to be mono-exponential with $\tau_2 \sim 7.25(6.25)$ s and $\tau_2 \sim 5.82(5.42)$ s respectively at 488 nm (514 nm) pump. This indicates that at longer wavelength(≥ 633 nm) only one shallow level contributes to the LIA. The values reported by Brost and Motes [131], and Kaczmarek *et al.* [132] for 6–10 s, and Corner *et al.* [133] for 7 s are in close agreement with these measurements. This origin of decay is attributed to $Rh^{4+/5+}$ levels [134].

Table 2.4: Decay time constants for undoped $BaTiO_3$ at 488 nm (514 nm) pump.

λ_s (nm)	τ_1(s)	τ_2(s)
543	0.1 (0.12)	1.25 (1.3)
633	0.13 (0.12)	1.5 (1.4)
750	0.57 (0.53)	(—)

For undoped $BaTiO_3$ crystal we observed double exponential decay at 543 nm and 633 nm probe wavelengths. Whereas, the decay at 750 nm and 800 nm was mono-exponential. The reported values of two decay constants by Song *et al.* [135] closely match with our results recorded in Table 2.4. It should be pointed out that the observations of different time constants need not necessarily be identified with different shallow traps as the local heating of the crystal at different pump wavelengths can give rise to different thermal excitation rate for the same shallow level.

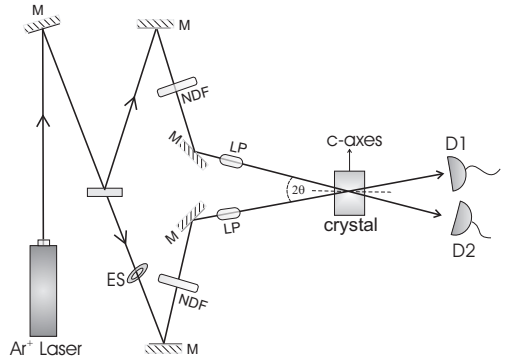

Figure 2.10: Experimental layout for two-wave mixing in PR crystals.

2.5.2 Two-wave Mixing Studies in $BaTiO_3$

A standard set up for two-wave coupling is shown in Figure 2.10. The direction of the c-axis of the crystal is chosen so that the energy is transferred from the pump beam to the signal beam. To write a refractive index grating, the path difference between the two interacting beams is kept well within the coherence length of the laser. The external beam-crossing angle 2θ was fixed at 35^o and photorefractive gain γ_o was measured at different intensity ratios $m = I_p/I_s$ by varying I_s at fixed pump power.

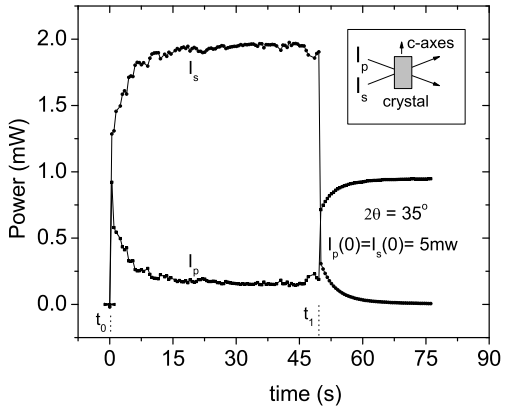

Figure 2.11: Two-wave energy coupling in Rh-doped $BaTiO_3$ crystal at 488 nm.

The energy exchange in two beam coupling in Rh:$BaTiO_3$ crystal can be seen in Figure 2.11. Figure 2.12 shows the plot of γ_o as a function of m. The gain was also measured at different beam-crossing angles at fixed m. The optimum beam-crossing angles that corresponds to maximum gain for Rh-doped and undoped $BaTiO_3$ crystals were found to be $\approx 30^o$ and $\approx 40^o$, respectively. The grating decay was monitored by putting the signal beam off at t_1 as shown in Figure 2.11. Further analysis of the data revealed that rise and decay of grating have bi-exponential form with two time constants. Again, the origin of different time constants can be attributed to the presence of deep and shallow impurity centers. Grating buildup and decay time scales observed in TWM are not very different from that found in absorption buildup and decay processes. Therefore, it will not be inappropriate to assert that absorption dynamics governs the TWM dynamics of the crystal to a

great extent [136].

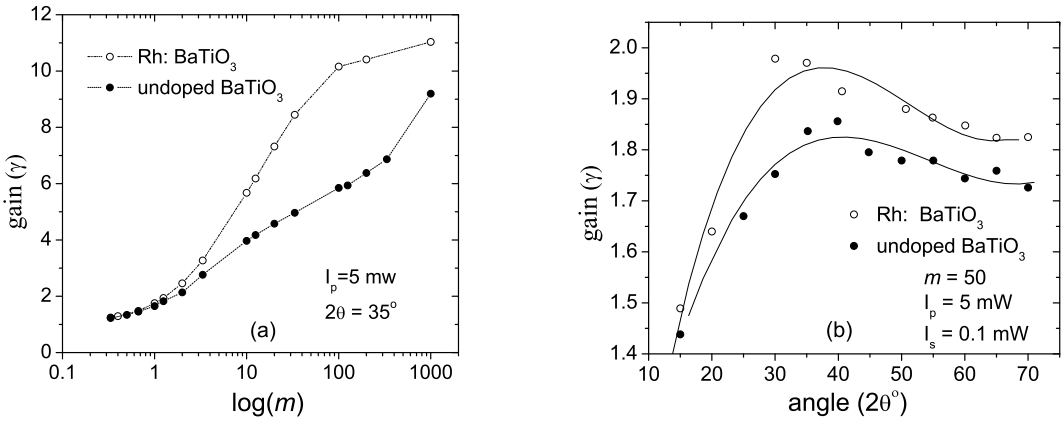

Figure 2.12: (a) Plot of gain vs intensity ratio m (b) gain vs beam-crossing angle measured at 488 nm.

2.5.3 Diffraction Efficiency Measurements in Fe:Ce:Ti-doped $LiNbO_3$

The unidirectional energy transfer by two-wave mixing does not occur in PR materials in which the phase shift is either zero or π. In $LiNbO_3$ crystals, the charge transport mechanism is driven by diffusion as well as strong photovoltaic effect [137]. As a result, the phase-shift between interference pattern and the refractive index grating is approximately π [138]. Therefore, ordinarily, the grating written in $LiNbO_3$, diffracts both the writing beams equally without preferential exchange of energy.

Diffraction efficiency measurements were made using conventional TWM experimental set-up shown in Figure 2.10. The crystal used was a 0°-cut, triplly-doped (Fe=0.05%; Ce=0.02% and Ti=0.02%) $LiNbO_3$. It was grown by Czochralski technique. All sides of this crystal (size=1cm^3) were polished to optical quality. Same crystal was later used for holographic data storage (Chapter 4).

In all the experiments, the laser power for both the beams at the input face of the crystal was fixed, i.e., $I_1(0) = I_2(0) = 5\,\mathrm{mW}$. Parametric studies of grating build-up, erasure and diffraction efficiency (η_{diff}) were carried out at 488, 514 and

532 nm. The details of respective laser sources are given in the appendix. Two experimentally investigated cases are:

Case 1:- η_{diff} as a function of grating spacing Λ_g. The grating spacing Λ_g was varied by changing the beam-crossing angle over a range of 10°−90°. In this case, the crystallographic c-axis of the crystal was normal to the bisector of the two beams, i.e., $\widehat{\text{c}}$-axis || K_g.

Case 2:- η_{diff} as a function of ϕ, where ϕ is angle between c-axis and grating wave vector K_g. In this case, the beam-crossing angle was fixed at 30° and ϕ was varied from −30° to 30° by rotating the crystal about the vertical axis.

In both cases, η_{diff} was measured by momentarily blocking ($\approx$ 100 ms) one of the writing beams with an electronic shutter in regular intervals ($\approx$ 3 min) of time. Diffraction efficiency of dynamic grating was calculated using Eq. (2.39).

Figure 2.13(a) shows a typical evolution of η_{diff} in TWM measured at three different wavelengths.

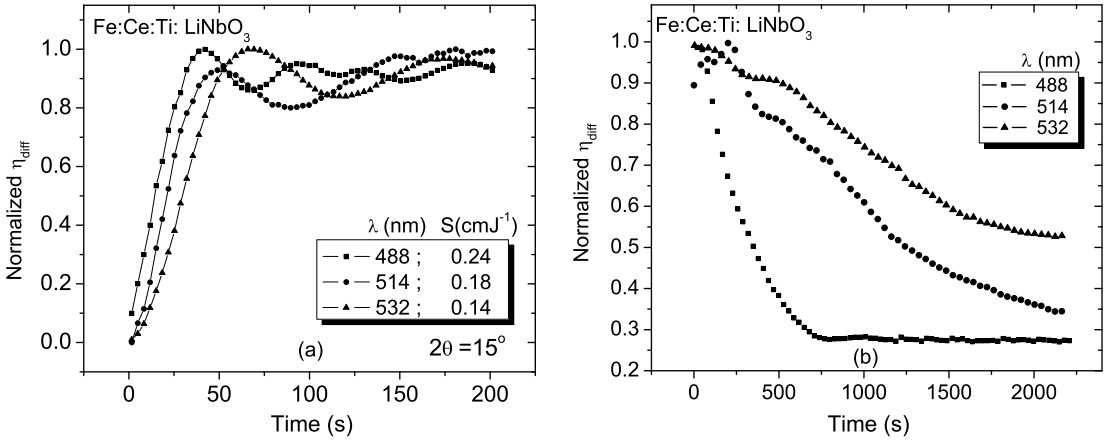

Figure 2.13: (a) Evolution of diffraction efficiency and (b) grating erasure curves in the presence of uniform beam illumination.

The oscillatory behaviour of diffraction efficiency is worth consideration. In recent studies, Ren *et al.* has observed a similar diffraction oscillations in Ce:Cu:LiNbO_3

Table 2.5: Diffraction efficiency measurements in Fe:Ce:Ti-doped $LiNbO_3$ crystals.

S. No.	case 1		case 2	
λ (nm)	η_{diff}(max)	t_{ss} (s)	η_{diff}(max)	t_{ss} (s)
488	60%	35-160	67%	35-170
514	66%	45-240	65%	60-300
532	83%	60-360	70%	120-420

crystal [139]. The physical origin of oscillations has been attributed to strong beam-coupling effects in weakly oxidized crystals, where more electrons participate in PR grating formation. This leads to index grating of strong modulations with large beam coupling and if the medium is considerably thick, the diffraction may oscillate. On the other hand, the doping centers in strongly oxidized crystals contain fewer electrons, which produces a grating of low index modulation and hence negligible beam coupling. In such case, the diffraction efficiency increases monotonically during the grating recording.

Table 2.6: Diffraction efficiency and sensitivity in several $LiNbO_3$ crystals doped with different impurities.

Crystals	λ (nm)	η_{diff}(%)	S(cmJ^{-1})	References
In:$LiNbO_3$	780; 488 †	8	0.003	[140]
Ce:Cu:$LiNbO_3$	633; 390 †	32	0.022	[141]
Fe:Mn:$LiNbO_3$	633; 404 †	25	0.033	[76]
Ce:Mn:$LiNbO_3$	633; 404 †	2.5	0.020	[76]
Tb:Fe:$LiNbO_3$	532 ‡	55	0.1	[142]
Pr:$LiNbO_3$	390; 850 †	50	0.013	[143]
Y:Fe:$LiNbO_3$	503 ‡	60	—	[144]
Fe:$LiNbO_3$	514 ‡	50	—	[145]
Fe:Ce:Ti:$LiNbO_3$	488, 514, 532 ‡	60–83	0.14–0.24	present studies

† Two-color holography; ‡ One-color holography

One of the main drawbacks of lithium niobate is its low recording speed compared to other PR crystals. The measure of recording speed is usually given by sensitivity S which is defined as [146],

$$S = \frac{1}{I_R\, d}\left|\frac{\partial\sqrt{\eta_{\text{diff}}}}{\partial t}\right|_{t=0} \tag{2.42}$$

where I_R is the recording intensity, d the crystal length. Eq. (2.42) basically represents the recording slope of the square root of the diffraction efficiency η_{diff} at $t = 0$.

For the three curves shown in Figure 2.13(a), the respective S values measured at 488 nm, 514 nm and 532 nm are; 0.24, 0.18 and 0.14. Typical η_{diff} and S reported in literature for normal and two-color holographic recording in $LiNbO_3$ crystals with different dopants are listed in Table 2.6. Regardless of the nature of the impurities, recording at the shorter wavelengths clearly seems to increase the sensitivity.

The grating erasure was studied by switching one of the writing beam *off* after the grating was written. The diffracted beam was continuously monitored with optical power meter. Figure 2.13(b) shows a typical grating erasure with one of the writing beam *on*. The variation of η_{diff} with beam-crossing angle is shown in

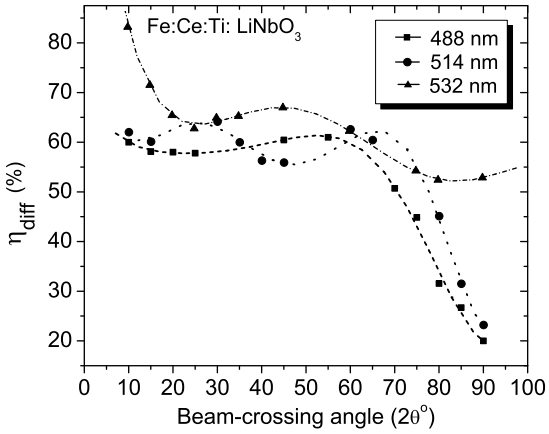

Figure 2.14: Variation of diffraction efficiency with beam-crossing angle. Experimental data is represented by different symbols, whereas broken curves are just visual guide through experimental data points.

Figure 2.14. Maximum diffraction efficiency $\eta_{\text{diff}}(\text{max})$ and typical time scales t_{ss} to reach the steady-state value are recorded in Table 2.5. The main points to note, are:

- Diffraction efficiency is the direct measure of the grating strength. While the maximum diffraction efficiency, $\eta_{\text{diff}}(\text{max}) \approx 83\%$, was observed at longer wavelength, i.e., 532 nm, the recording speed was faster at shorter wavelength 488 nm. This is because the grating period is larger at longer wavelength ($2\Lambda_g \sin\theta = N\lambda$) and therefore, the free charges need more time to migrate.

- From the oscillatory behaviour of diffraction, it may be concluded that the

optimum time for recording a hologram is the time it takes to reach the first maxima.

- From the diffraction efficiency measurements, the estimated values of refractive index change for the present crystal is, $\Delta n \approx 10^{-5}$. Therefore, Eq. (2.32) implies a space-charge field of the order of 10^2 kVm^{-1}.

- Grating decay is relatively slower even in the presence of uniform beam illumination. It can be seen from the erasure curves (Figure 2.13) that the grating has not decayed even to 10% of its initial value within the observation time of 20-30 minutes. Especially, the grating recorded at 532 nm has very slow erasure rates. For example, a single hologram recorded at 532 nm can be read out nearly 200,000 times using a 5 mW beam with 10 ms duration -before the grating decays to 50% of its original value. This is extremely useful feature for realizing non-volatile holographic memories.

2.6 Conclusion

Steady-state and temporal measurements of LIA and TWM have been carried out in undoped and Rh-doped $BaTiO_3$ crystals. Various parameters pertaining to the temporal and steady-state behavior of LIA have been obtained at different wavelengths and intensities of laser light. The observed behavior is interpreted in terms of two-center charge-transport model for PR materials. The rate equations were solved to derive an analytical expression for steady-state absorption changes. Various model parameters like build-up and decay rates, thermal excitation rates, and two-wave coupling gain have been obtained and compared with the earlier studies. Theoretical calculations based on a two-center charge transport model agree well with the experimental results which supplement the earlier studies carried out using PR $BaTiO_3$ crystals. The LIA can greatly influence the dynamics of two-wave mixing and holographic grating recording in photorefractive crystals. Therefore, the effect of LIA needs to be properly understood and incorporate in any device application based on photorefractive crystals.

An unusual absorption in Rh:$BaTiO_3$ is reported at 514 nm pump and 633 nm probe wavelength. In light of two-center charge transport model it can be argued that light-induced thermal effects create (new) or activate (already existing) impurity traps that are highly wavelength specific in terms of their energy levels and absorption cross-section. However, This needs to be probed separately by performing temperature dependent absorption studies.

Finally, the results of diffraction efficiency, sensitivity and grating erasure studies in triplly-doped Fe:Ce:Ti:$LiNbO_3$ crystal are presented. From the observed diffraction efficiency (60-80%) and slow erasure rates of PR grating, the crystal seems to be well suited for non-volatile optical memories.

Chapter 3

Modulation Properties of the Spatial Light Modulator

3.1 Introduction

Liquid crystal (LC) based spatial light modulators (SLM) are devices that function as a reusable transparencies capable of modulating the light according to a fixed spatial pattern. As the name suggests, liquid crystals are materials which exhibit properties intermediate to the solid and the liquid state of matter. The initial research in LC technology was mainly driven by the electronic consumer industry meant for the developing various projection displays, computer screens, liquid crystal television [147–151]. The increasing versatility and low cost of LC spatial light modulators (LC-SLM) have lead to research in scientific areas ranging from optical correlation, beam steering, matched filtering, polarization control to optical data processing, wavefront correction using adaptive optics etc [152–160].

SLM is one of the most important system components in holographic data storage system (HDSS). It is used for composing a data page prior to the storage [161]. While LC-SLM present a straight forward and practical solution for spatial modulation (amplitude or phase) of light for HDSS system, these are limited both in terms of spatial resolution and also bit depth that determines the available grey scale range [162]. Moreover, the light transmission characteristics (intensity versus voltage response) of LC-SLM are highly nonlinear and exhibit a wide range of variations with

different parameter settings. Most often there is no *a priori* information about the dependence of intensity and phase modulations on various parameters like brightness and contrast control, threshold voltage, polarization orientation of incident light etc. In this chapter, the modulation properties of a commercially available LC-SLM are presented. The SLM response at various parameters would help to locate an optimum range of operation that is required to suit its usage in HDSS. Therefore, if the SLM is 'biased' to a optimum operating point (governed by relative orientation of the polarizer and the analyzer and appropriate brightness and contrast settings) that lies within the maximum linearity of the response curve, then over a certain grey level range the SLM will provide a square law mapping of incremental change in incident light amplitude into incremental change of amplitude transmittance. Experimentally obtained various intensity modulation curves are best described either by power-law or sigmoidal functions. Based on the power-law transformation, an appropriate pre-processing of input grey scale images for page oriented holographic data storage applications is also suggested.

In section 3.2, the basic principle and theoretical background required to model twisted nematic liquid crystal (TNLC) cell is explained. Experimental details, results and the discussion are given in section 3.3. In the last section 3.4, a simple technique for the determination of pixel size and pitch of LC based SLM is presented. The proposed method is based on optical diffraction from pixelated LC panel that has been modeled as a 2-dimensional array of rectangular apertures. A novel yet simple, two plane measurement technique is implemented to circumvent the difficulty in absolute distance measurement.

3.2 Theory and Background

SLM usually consists of 2-dimensional array of densely packed pixel elements called LC cells. A coating of transparent electrode allows voltage to be applied across any individual cell. The nematic LC material that fills the gap between two parallel glass plates has layers of elongated molecules. These molecules exhibit orientational order within the cell and have anisotropic optical properties similar to uniaxial crystals

[163]. The optical axes of such a system is parallel to the molecular orientation, which is also known as molecular director. The inner surface of the glass plates have groove pattern etched with certain orientations so that the LC molecules are also aligned along the direction of groove pattern.

In parallel aligned LC cell, the two glass plates have groove pattern along same direction. Therefore, all the molecules in different layers maintain same orientation throughout cell.

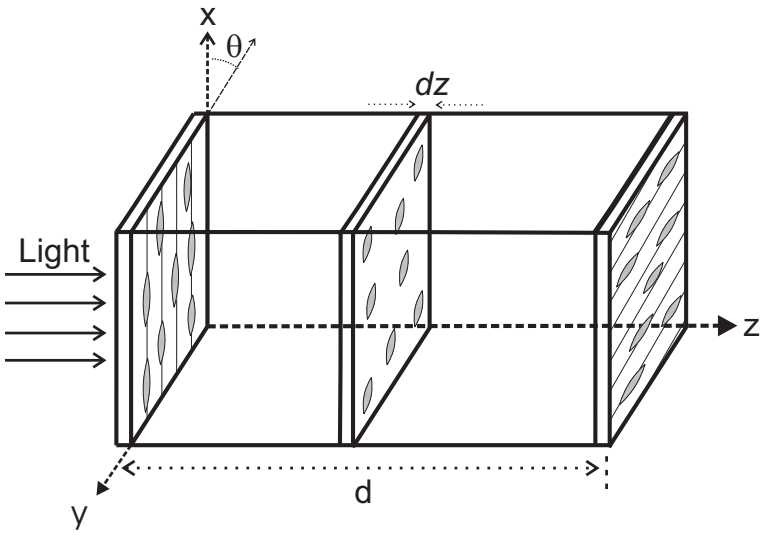

Figure 3.1: A geometrical construction of a twisted nematic liquid crystal cell showing three layers of molecules progressively rotated in x-y plane along the cell thickness.

In twisted nematic liquid crystal, the groove pattern on two glass plates is oriented in different directions. Therefore, the orientation of the molecules in TNLC between two glass plates rotates gradually from one plate to another in a helical fashion through an angle α. This angle is called the twist angle. A typical geometry of a 90° TNLC cell is shown in Figure 3.1. The light transmission properties of each cell can be controlled using externally applied voltage signal.

In the *off-state* (zero voltage applied to LC cell), an incident light beam linearly polarized along molecular director (or perpendicular to molecular director) at the input face will undergo a polarization rotation exactly equal to the twist angle. If the polarization vector of the input light is oriented along any other direction, then due to birefringence, the optical wave propagating in z direction will have two normal

polarization modes in (x, y) plane. These are known as extraordinary (e-ray) and ordinary (o-ray) ray having the index of refraction as n_e and n_o, respectively. The resulting output light, therefore, will have an elliptical polarization. In short, the optical activity and birefringence properties of TNLC are used for controlling the polarization as well as phase of the light beam.

For all practical purposes, the propagation of light through a TNLC cell is described by Jones calculus. In this approach the entire LC cell of length d is divided into several wave plates of elementary thickness dz whose optical axes is rotated progressively along the length. The overall Jones matrix of linearly twisted anisotropic LC cell is given by [164, 165]:

$$\mathbf{M}_{\mathrm{LC}} = \mathbf{R}(-\alpha) \begin{pmatrix} \cos X - i\frac{\beta}{2}\frac{\sin X}{X} & \alpha\frac{\sin X}{X} \\ -\alpha\frac{\sin X}{X} & \cos X + i\frac{\beta}{2}\frac{\sin X}{X} \end{pmatrix} \tag{3.1}$$

where

$$X = \sqrt{\alpha^2 + \left(\frac{\beta}{2}\right)^2}, \tag{3.2}$$

β, the phase retardation. The rotation matrix $\mathbf{R}(\cdot)$ for the coordinate transformation is given by,

$$\mathbf{R}(\cdot) = \begin{bmatrix} \cos(\cdot) & \sin(\cdot) \\ -\sin(\cdot) & \cos(\cdot) \end{bmatrix} \tag{3.3}$$

If an electric field is applied between the two plates, all the molecules experience a tilt along the field direction. Therefore, the plane of molecular orientation no longer remains confined to x-y plane and the effective rotation angle seen by input light also decreases. The tilt angle of the molecules depends on the strength of applied voltage. The relationship between tilt angle θ and applied r.m.s voltage V is given by [166]:

$$\theta = \begin{cases} 0, & V \leq V_{th} \\ \frac{\pi}{2} - 2\tan^{-1}\left[\exp\left(-\frac{V-V_{th}}{V_o}\right)\right], & V > V_{th}, \end{cases} \tag{3.4}$$

where V_{th} is the threshold voltage below which no tilt occurs and V_o is the access voltage at which the tilt angle is 49.6°. For a tilt angle θ, the extraordinary index of refraction now becomes:

$$\frac{1}{n^2(\theta)} = \frac{\cos^2\theta}{n_e^2} + \frac{\sin^2\theta}{n_o^2} \tag{3.5}$$

The phase retardation β between two propagating modes can be expressed as,

$$\beta = \frac{2\pi}{\lambda} \left[n(\theta) - n_o \right] d, \tag{3.6}$$

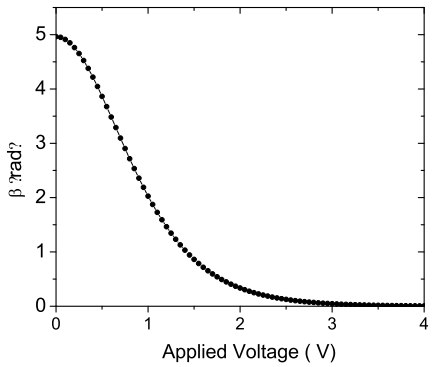

Figure 3.2: Plot of calculated phase retardation versus applied voltage.

The retardation is maximum in off state ($\theta = 0$ and $n(\theta) = n_e$) and decreases monotonically towards 0 when the tilt angle approaches 90°. Figure 3.2 shows the plot of phase retardation β calculated using Equations (3.4)-(3.6). The typical parameters used in calculations are: $n_o = 1.55$, $n_e = 1.6$, $d = 10\,\mu$m, $\lambda = 633.\,$nm. If the applied field is sufficiently large then all the molecules will be tilted by 90° along the field direction. In this case, the polarization of the input light will not change as the LC molecules now would behave like isotropic materials.

3.2.1 Modelling

The Jones matrix analysis can be used to predict the intensity and phase modulation of properties of the twisted LC cell. A common scheme used for studying the modulation properties of the LC–SLM is to sandwich it between a polarizer and an analyzer as shown in Figure 3.3. Here, θ_1, θ_2 and ψ are the arbitrary angles that the axes of polarizer, analyzer and molecular director at the input face make with the lab vertical. The direct use of Jones calculus results in:

$$\mathbf{E}_{\text{out}} = \mathbf{M}_{\text{eff}} \mathbf{E}_{\text{in}} \tag{3.7}$$

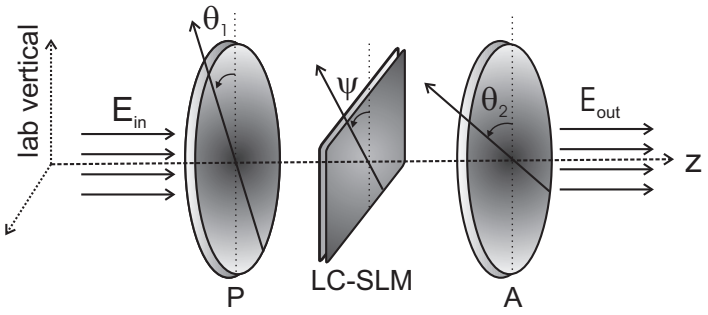

Figure 3.3: Basic configuration showing the orientation of the polarizer P, the twisted nematic LC–SLM and the analyzer A.

where $\mathbf{E}_{\text{out}} = [E_x \quad E_y]^T$; $\mathbf{E}_{\text{in}} = [\cos\theta_1 \quad \sin\theta_1]^T$ are the Jones vector for input and output radiation fields, respectively, and $\mathbf{M}_{\text{eff}}$ is the effective Jones matrix of the entire system given by,

$$\mathbf{M}_{\text{eff}} = \mathbf{R}(-\theta_2)\cdot\mathbf{A}\cdot\mathbf{R}(\theta_2)\cdot\mathbf{R}(-\psi)\cdot\mathbf{M}_{\text{LC}}\cdot\mathbf{R}(\psi)\cdot\mathbf{R}(-\theta_1)\cdot\mathbf{P}\cdot\mathbf{R}(\theta_1) \tag{3.8}$$

The rotation matrix $\mathbf{R}(\cdot)$ is already defined in Eq. (3.3). In the laboratory coordinate system the Jones matrix for the polarizer and the analyzer is:

$$\mathbf{P} = \mathbf{A} = \begin{bmatrix} 1 & 0 \\ 0 & 0 \end{bmatrix}. \tag{3.9}$$

The expression for transmitted intensity can be written as,

$$T = |\mathbf{E}_{\text{out}}|^2 = |E_x|^2 + |E_y|^2 \tag{3.10}$$

Two special cases of interest for intensity transmittance can be obtained by setting $\theta_2 = \theta_1$ for the parallel orientation $T_{||}$ and $\theta_2 = \theta_1 + 90°$ for a crossed orientation $T_\perp$ of the polarizer and the analyzer. After the algebraic simplification of Eq. (3.8), the corresponding intensity transmittance for the two configurations can be written as,

$$T_{||} = \left[\cos X\cos\alpha + \frac{\alpha}{X}\sin\alpha\sin X\right]^2 + \left(\frac{\beta}{2X}\right)^2 \sin^2 X\cos^2(\alpha - 2\theta_1 + 2\psi) \tag{3.11}$$

and

$$T_\perp = \left[\cos X\sin\alpha - \frac{\alpha}{X}\cos\alpha\sin X\right]^2 + \left(\frac{\beta}{2X}\right)^2 \sin^2 X\sin^2(\alpha - 2\theta_1 + 2\psi) \tag{3.12}$$

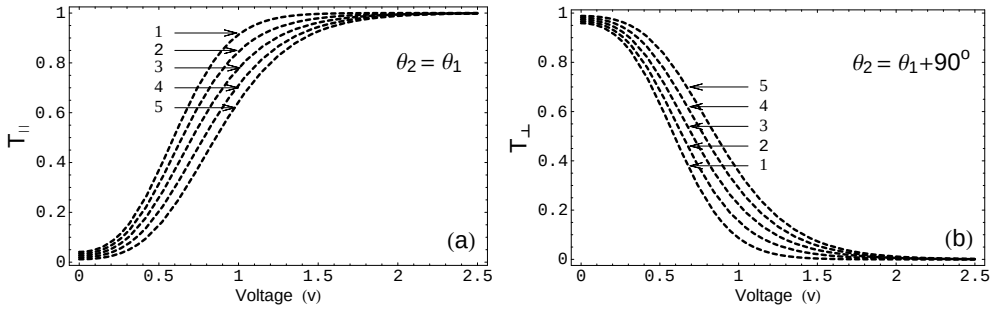

Figure 3.4: Calculated transmittance (a) for parallel and (b) for crossed configuration. Curve 1-5 correspond to $\theta_1 = 0, \frac{\pi}{12}, \frac{\pi}{8}, \frac{\pi}{6}$, and $\frac{\pi}{4}$, respectively.

As shown in section 3.3.1, the Eqs. (3.11) and (3.12) can be used to determine the physical parameters like twist angle α, the orientation of molecular director ψ at the input face and maximum phase retardation

The transmittance as a function of applied voltage for different settings of θ_1 is calculated using Eqs. (3.11) and (3.12). Figure 3.4(a) and Figure 3.4(b) show the simulated results for transmittance in parallel and crossed configuration of the polarizer and the analyzer. The experimental results obtained in section 3.3 are in good conformity with the model.

It is clear from the section 3.2 that the application of voltage not only effect the polarization rotation property of the LC cell (there by resulting in intensity modulation) but also significantly modulates the phase of optical field as the tilt angle varies from 0° to 90°. Therefore, in a TNLC, a certain amount of cross-coupling between intensity and phase modulations in inevitable.

Figure 3.5 shows the dependence of intensity transmittance on phase retardation β. A phase-only modulation can be realized over a region where the transmittance does not vary appreciably. For example in Figure 3.5, when $\theta_1 = 45°$ in crossed configuration, the transmittance of the device is $\geqslant 90\%$, for $\beta \geqslant 5.4$ rad. Which in turn, from Eq. (3.6), requires $\beta_{\max} \geqslant 5.4$ or $\frac{2\pi}{\lambda}\Delta n\, d \geqslant 5.4$. Due to small cell thickness d and low value of birefringence $\Delta n \approx 0.1$, most of the SLMs are not designed to meet these condition. In practice, a pure phase modulation is achieved easily using parallel aligned nematic LC-SLM.

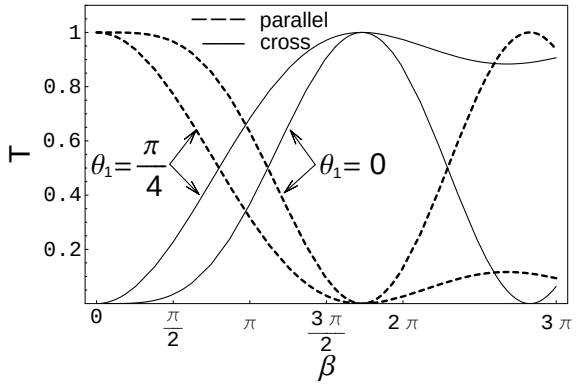

Figure 3.5: Dependence of transmittance on β.

3.2.2 Nonlinearities and Corrections

The nonlinear response of variety of devices used in imaging system can severely degrade the image quality. In that context, SLM used in various optical information processing is also not an exception. However, it is possible to mitigate the effect of nonlinearities by certain transformation techniques applied to the input signal.

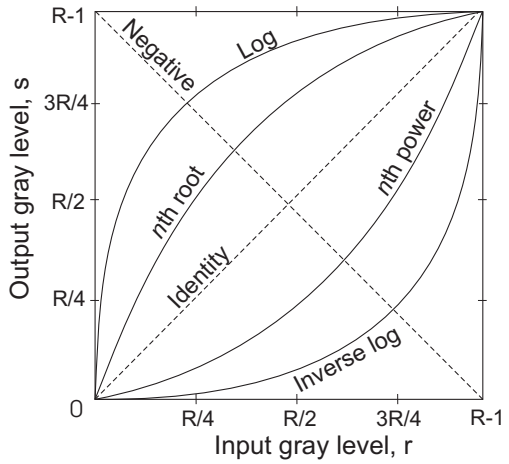

Figure 3.6: Sketch of basic grey–level transformation in the range [0, R-1].

Here the discussion is confined only to pre–processing of grey scale digital images that is required to compensate for SLM nonlinearities. Mathematically, the spatial domain transformation for an input image $f(i, j)$ can be expressed as,

$$Y(i, j) = \mathcal{T}[X(i, j)] \tag{3.13}$$

where $Y(i,j)$ is the processed image and $\mathcal{T}$ is an operator on f defined over some neighbourhood of (i,j). For any point (i,j) when the neighbourhood is of the size 1×1 (single pixel), $\mathcal{T}$ becomes a grey–level transformation that maps the pixel value r at $X(i,j)$ into pixel value s, at $Y(i,j)$. In other words,

$$s = \mathcal{T}(r) \tag{3.14}$$

In general, any imaging device can be modeled based on its input/ouput mapping response curves. For example, the input/output relationship between grey levels under three different transformations (linear, logarithmic and power–law) is shown in Figure 3.6. For the spatial light modulator the response curves can be calculated using the model presented in previous section or determined experimentally as shown in the next section. The required pre–processing and corrections can be accomplished by applying a suitable inverse transformation.

3.3 Experimental Details

The SLM in lab is an electrically addressed LC2002 model from HoloEye Photonics. The device consists of a twisted nematic LC panel (Sony LCX016AL–6; active area: $26.6\times20.0\,\mathrm{mm}^2$; number of pixels: 832×624; pixel pitch: $32\,\mu$m) and driver electronics that can be plugged directly to output of the graphics card of a PC. Therefore, the direct access to input signal and bias voltage applied to the individual cells of the LC panel is not available. Image parameters like brightness and contrast settings can be controlled using the driver software over a range from 0–255. However, there is no a priori information about the dependence of modulation properties on the brightness and the contrast control.

3.3.1 Determination of the Physical Parameters

It is necessary to first accurately determine the various unknowns like the twist angle α, the orientation of the molecular director ψ w.r.t. laboratory coordinate system and the maximum phase retardation $\beta_{\max}$. As shown in Figure 3.3, LC–SLM was inserted between the Glan laser polarizer and the analyzer that were mounted on a

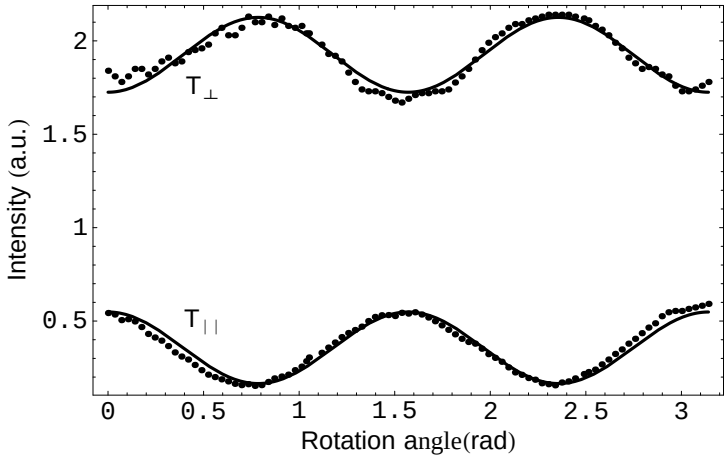

Figure 3.7: Transmitted intensity in crossed ($T_\perp$) and parallel ($T_\parallel$) orientations of the polarizer and the analyzer. The dots represent the experimental data and the solid curves are the best fit of the model.

360° rotational stage and had extinction ratio $< 10^{-5}$. An expanded and collimated He–Ne laser beam at 632.8 nm was used to back illuminate the SLM in *off–state*. For a fixed polarizer orientation θ_1, the analyzer was rotated through 0 to 360° and the transmitted light intensity was monitored using computer controlled optical power meter (Model: 4832-C Multichannel Optical Power Meter; Newport). Same procedure was repeated for every orientation of the polarizer in step of 1° from 0 to 360°. According to the theory of TNLC given in previous section, a null in transmitted intensity occurs when the polarizer is oriented along the director axes of the molecules at the input face, that is, $\theta_1 = \psi$ and $\theta_2 = \theta_1 + \alpha$. The measured values of twist angle α and director orientation ψ were found to be $90° \pm 0.5°$ and $45° \pm 0.5°$, respectively. The experimental procedure given in reference [167] is followed to determine $\beta_{\max}$. That is, the polarizer and the analyzer were rotated simultaneously while aligned in parallel or in crossed configuration. Therefore, the transmitted intensity as a function of rotation angle can be predicted by Eqs. (3.11) and (3.12). A comparison between the model and the experimental data that was taken at every 5° rotation interval, is shown in Figure 3.4. Having found α and ψ already, a nonlinear best parameter fit of the Eqs. (3.11) and (3.12) is used to determine average $\beta_{\max} \approx 4.45$ rad.

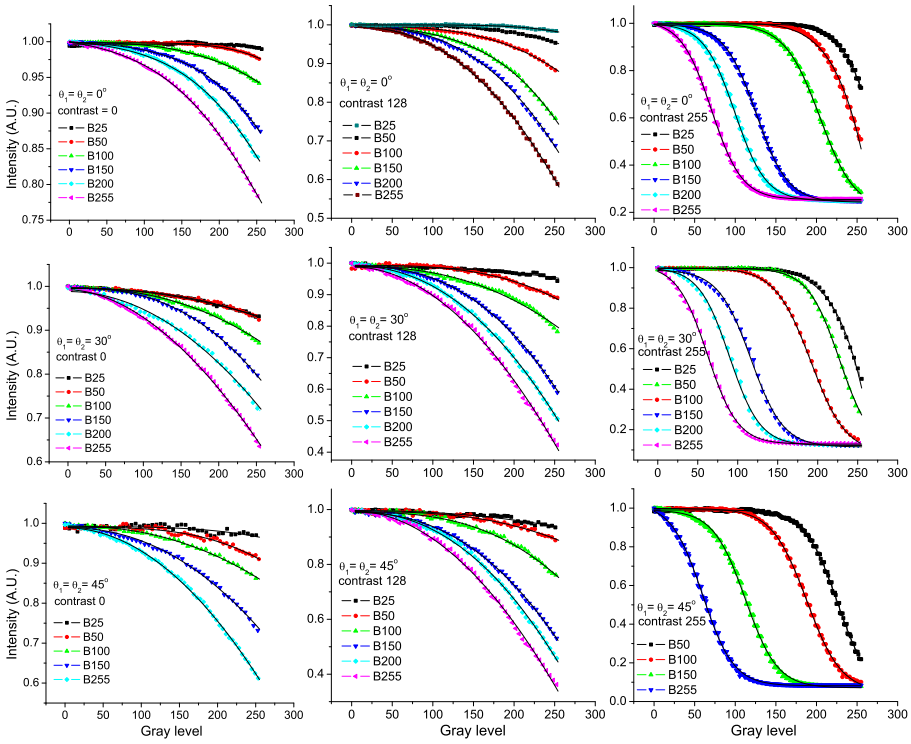

Figure 3.8: Normalized intensity modulation curves in crossed configuration of the polarizer and the analyzer. The curves identified with different symbols correspond to different brightness (B25, B50,.. etc.) settings.

3.3.2 Intensity Modulation Curves

In this section, the optical transmission properties of LC-SLM in *power-on* state are studied. The r.m.s. voltage signal that drives individual LC cells is proportional to the pixel grey level in the image. In addition to it, the intensity and phase modulation also depend on the brightness and contrast setting and also on the relative orientation of the polarizer and the analyzer. The intensity modulation was studied by electronically addressing the SLM with several *plane* images. Here, *plane* image means, an image with one shade or intensity.

A computer programme was written to sequentially address a set of 51 *plane* images with grey level varying progressively from 0–255 in steps of 5. An expanded laser beam illuminates the central portion (500 × 500 pixels) of LC panel and the variations in transmitted intensity were recorded simultaneously using computer controlled large area photodetector. The measurements were made at several bright-

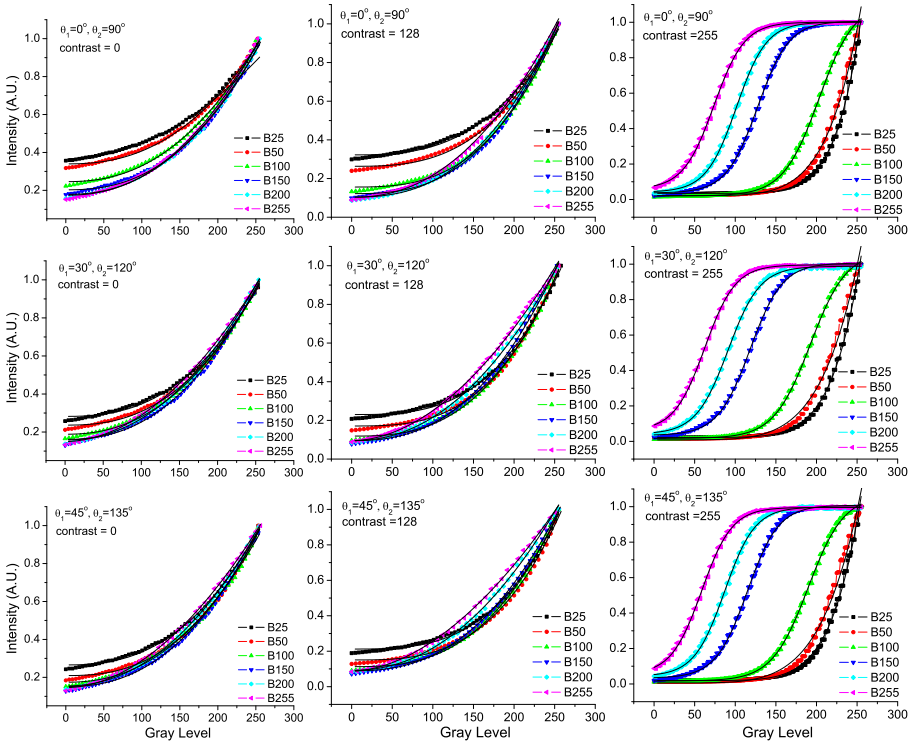

Figure 3.9: Normalized intensity modulation curves in parallel configuration of the polarizer and the analyzer. The curves identified with different symbols correspond to different brightness (B25, B50,.. etc.) settings.

ness and contrast settings. Some of the representative curves for crossed and parallel configurations of polarizer and analyzer are shown in Figures 3.8 and 3.9, respectively. The measured data is represented by different symbols, whereas thin lines are the nonlinear curve fitting using power-law or sigmoidal function. *Intensity modulation depth*(IMD) can be defined as the difference in the transmitted intensity at grey level 255 and 0, that is, $|T(\mathrm{GL}=255) - T(\mathrm{GL}=0)| \times 100\%$.

Table 3.1: Intensity modulation depth (%) at different brightness and contrast settings in parallel configuration of the polarizer and the analyzer.

	B25			B150			B255		
θ_1	C0	C128	C255	C0	C128	C255	C0	C128	C255
0°	65	70	82	90	98	100	85	91	93
30°	75	79	100	87	92	92	87	91	91
45°	76	81	100	87	93	92	87	92	91

Note: The prefix B and C stand for brightness and contrast, respectively.

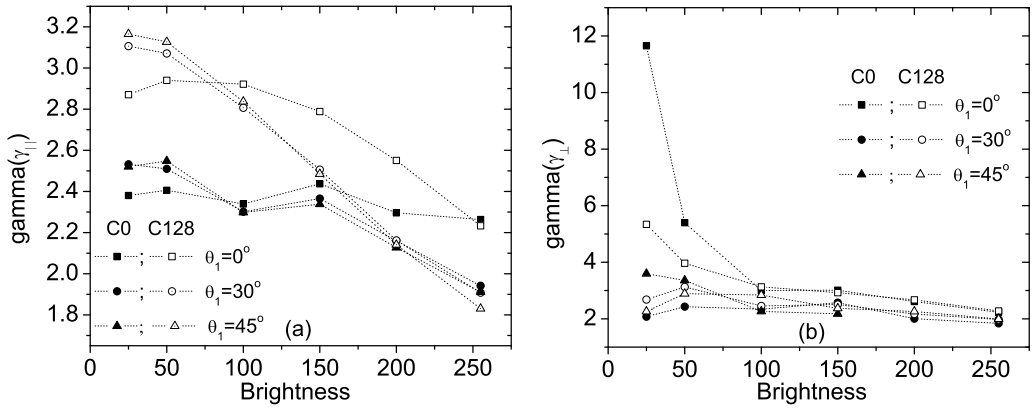

Figure 3.10: Plot of power-law exponent gamma (γ) versus brightness control as a function of orientation and contrast settings for (a) the parallel and (b) the crossed configurations. Filled and open symbols correspond to contrast setting of 0 and 128, respectively.

From practical point of view the configuration that gives an intensity modulation depth of 100% is most desirable. A brief comparison between Figure 3.8 and Figure 3.9 shows that the maximum IMD in crossed orientation of the polarizer and the analyzer is only around 85%, whereas it is possible to achieve IMD$\simeq$ 100% in the parallel configuration, also indicated in Table 3.1.

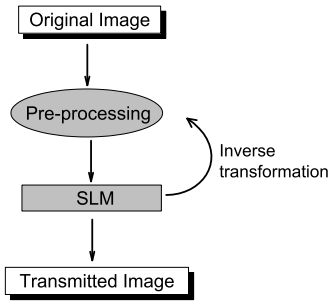

Figure 3.11: A general schema to correct the nonlinear response of the SLM by applying appropriate pre-processing technique to the original image.

The measured data (except for brightness $B > 50$ and contrast=255) for transmitted intensity can be approximated by the power-law response of the LC–SLM. Therefore, in terms of grey level transformation described in section 3.2.2, the power-law response can be expressed as,

$$s = a + b\, r^{\gamma} \tag{3.15}$$

where a, γ are real positive constants and $b > 0\,(b < 0)$ for parallel (crossed) configuration. For all the cases $\gamma > 1$, which implies that the response of LC–SLM is such that it maps a wider range of low input grey-levels into a narrow range of output values, and the opposite being true for higher input grey-levels. This essentially amounts to decrease in overall brightness and increase in contrast in the bright areas at the expense of the contrast in dark area. The γ values calculated by experimental data fitting using Eq. (3.15) are shown in Figure 3.10. The nonlinear response of the SLM can be corrected by appropriate pre-processing of the input images. The inverse transformation would require to expand low grey-level ranges while compressing the higher-level ranges. A general schema for such an approach is outlined in Figure 3.11.

To this end, let the response of SLM for a given configuration be characterized by some γ. Using Eq. 14, the inverse power-law transformation $\mathcal{T}$ can be chosen so that $s = r^{1/\gamma}$.

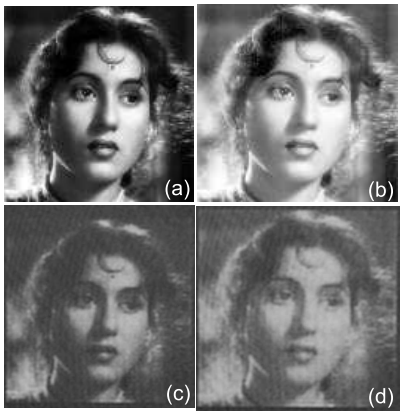

Figure 3.12: (a) Original image of *Madhubala*, (b) transformed image with $\gamma = 2.5$, (c) SLM output corresponding to original input image and (d) SLM output corresponding to transformed input image.

To demonstrate the effect of nonlinearities, 8-bit grey scale images were addressed onto the SLM placed between a crossed polarizer and analyzer. The transmitted image was captured by CCD camera placed behind the SLM. As shown before, the SLM pixels have a sublinear transmission response at low input grey-level range. Therefore, the transmitted image appears more darker than the original. For exam-

ple, Figure 3.12(a) shows the original (128 × 128 pixels) image of *Madhubala* that was addressed onto the SLM without any pre-processing. The darkening effect due to nonlinearities is clearly seen in the SLM transmitted image. Here, the brightness and contrast setting of the SLM was 128. This corresponds to $\gamma \approx 2.5$. Using the inverse power-law transformation, Figure 3.12(a) was transformed into Figure 3.12(b) by up-scaling the region of darker shades in the image. The improvement in SLM's response is clearly visible in Figure 3.12(d). A similar inference can be drawn for

Figure 3.13: (a) Original *Lena* image, (b) transformed image, (c) SLM output for the original image and, (d) SLM output for the transformed image.

Lena image shown in Figure 3.13. A small loss in visual image quality in both the cases was due to the low quality of polaroid sheet.

It is to be noted from Figures 3.8 and 3.9 that the intensity modulation curves for contrast setting 255 and brightness $B > 50$ do not follow power-law function. The response of LC–SLM in this regime is somewhat similar to H & D curves for photographic emulsion that can be described by a sigmoidal function of the form:

$$s = s_b + \frac{s_t - s_b}{1 + \exp[-(r - r_o)/w]} \tag{3.16}$$

where s_b, and s_t are two asymptotic values at small and large r. The curve crosses over between two asymptotic values in a region of r whose approximate width is w and which is centered around r_o. Visual representation of these parameters is shown in the Figure 3.14.

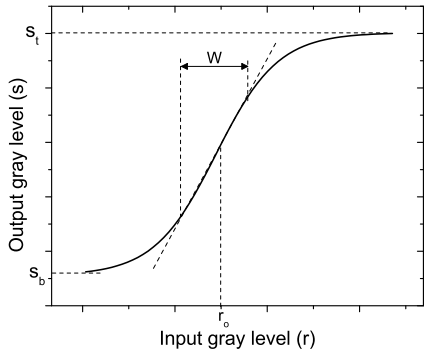

Figure 3.14: Sigmoidal function response of the LC–SLM when contrast = 255 and brightness $B > 50$.

The response of LC2002 around r_o is almost linear, however, the width w is rather small. The best parameter fits of sigmoidal function are recorded in Table 3.2.

Table 3.2: Best parameter fit of sigmoidal function for crossed (parallel) configuration.

θ_1	brightness	s_t	s_b	r_o	w	$r(20\%s)$	$r(80\%s)$
0°	100	1.12(1.00)	0.02(0.21)	204.2(203.2)	22.2(21.7)	172.4(174.1)	233.9(234.3)
	150	1.01(0.99)	0.04(0.24)	127.4(125.7)	19.4(19.1)	100.6(98.5)	154.2(152.9)
	200	1.00(1.00)	0.04(0.25)	101.4(99.3)	18.7(19.1)	75.5(72.8)	127.3(125.8)
	255	1.00(1.01)	0.06(0.25)	73.7(70.7)	18.9(18.8)	47.5(44.6)	99.8(96.7)
30°	100	1.08(1.00)	0.02(0.08)	192.3(191.6)	22.4(22.3)	161.2(160.3)	223.4(222.1)
	150	1.00(0.99)	0.03(0.11)	118.3(116.2)	19.9(20.3)	90.7(88.0)	146.8(144.4)
	200	0.99(1.00)	0.04(0.12)	91.1(89.7)	19.6(19.1)	63.8(63.1)	118.3(116.2)
	255	0.99(1.01)	0.06(0.13)	62.4(62.1)	18.8(19.0)	36.3(35.8)	88.5(88.4)
45°	100	1.07(1.00)	0.02(0.05)	189.6(187.9)	22.2(21.4)	158.9(158.2)	220.4(217.5)
	150	1.00(0.99)	0.03(0.07)	114.7(112.3)	19.4(19.8)	87.8(84.9)	141.5(139.7)
	200	1.00(–)	0.04(–)	86.8(–)	18.7(–)	60.8(–)	112.7(–)
	255	1.00(1.02)	0.05(0.08)	58.6(59.6)	18.8(19.1)	32.5(33.1)	– (86.1)

3.3.3 Phase Modulation

For a TNLC shown in Figure 3.1, when the polarization vector of the incident field is parallel to the molecular director, the applied voltage not only effect the optical activity of the medium but also changes the refractive index from n_e to n_o as can be envisaged from Eq. (3.5). Therefore, the phase of the e-wave propagating through

the cell is modulated significantly as the tilt angle varies from 0° to 90°. The refractive index of the incident o-ray, however, remains unchanged regardless of the tilt angle.

Digital interferometry based fringe-shift method was used to measure the phase modulation properties of the LC-SLM. Experimental setup to measure the phase changes δ while driving the LC-SLM at different grey level is shown in Figure 3.15. The transmission axes of the polarizer was aligned parallel to the molecular director at the input face of LC-SLM to ensure the propagation of light as e-ray alone.

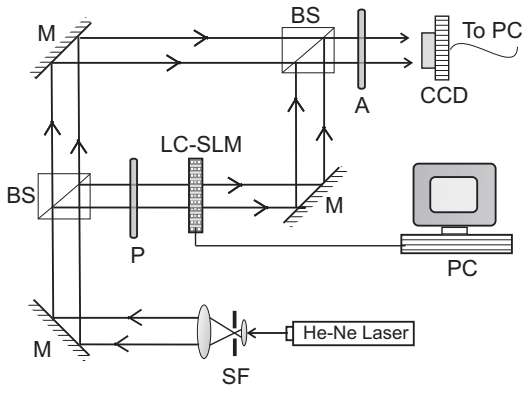

Figure 3.15: The Mach–Zehnder interferometric setup used in phase retardation measurement of LC–SLM. SF: Spatial Filter; M: mirrors; BS: beam splitters; P: polarizer; A: analyzer; CCD: charge coupled detector.

The interferometer was adjustment to obtain a straight line fringe pattern that remains stable during the measurements. As in the case of intensity modulation, several 8-bit grey scale images were addressed onto the LC-SLM and the corresponding fringe pattern was captured by a CCD camera (Pulnix TM-1320-15CL; number of pixels: 1300×1030; pixel size: $6.7 \times 6.7\,\mu$m). The procedure was repeated at different *brightness* and *control* settings. The high-frequency fringing effect due to coherent illumination of CCD is removed by low-pass Fourier filtering of the image data. Fringe shift can be seen clearly in Figure 3.16 that shows three sets of interference pattern recorded on the CCD at different grey scale images.

The phase retardation δ between two arms of Mach-Zehnder interferometer can

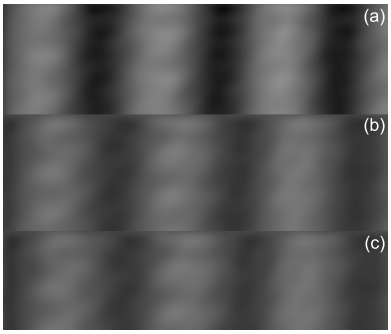

Figure 3.16: Fringe pattern recorded at: (a), 0 (b) 100, and (c) 250 grey levels, respectively.

be calculated using relation [168]:

$$\delta = \frac{\Delta}{\Lambda} \text{ (rad)} \tag{3.17}$$

where Δ is the fringe shift obtained by comparing the line profiles of the interferograms and Λ is fringe period.

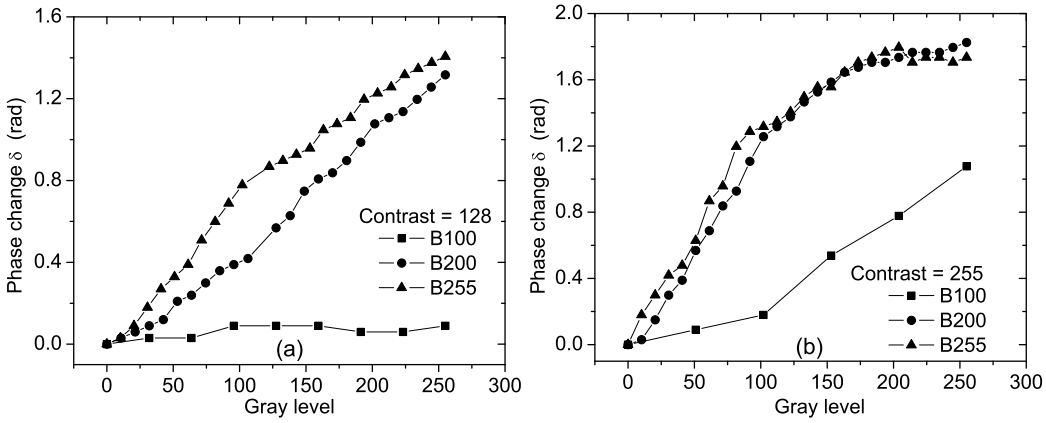

Figure 3.17: Plot of phase retardation δ versus grey level for LC2002 model.

The plot of phase retardation versus input grey level is shown in Figure 3.17. The maximum phase retardation obtained in *on-state* is $\delta \approx 1.8$ rad. This value is considerably smaller than the $\beta_{\max}$ obtained in *off-state*. This inadequacy is partly due to the complex electronics involved in driving the LC–SLM and also the fact that the tilt angle θ is not linear (due to the boundary effects) throughout the cell thickness. The relatively low values of δ also suggests that the device is better suited for applications that required intensity modulations, although, the accompanying phase changes, however small, cannot be decoupled.

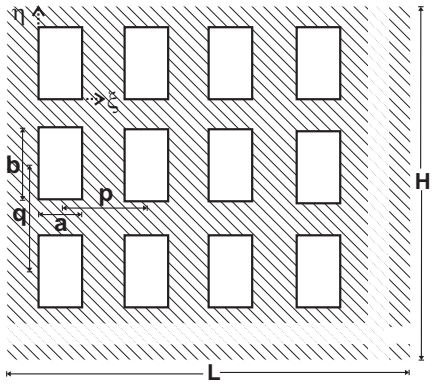

Figure 3.18: A typical geometry of two-dimensional LC panel.

3.4 Measurement of Pixel Size and Pitch

Another important figure of merit of SLM is spatial resolution that is determined by the size and total number of cells in the panel [169]. Present developments of LC technology have focused on increasing their pixel resolution through reduction in panels' thickness and their pixel pitch. In majority of the applications, ideally one would like to have an array of square pixels having equal pitch in horizontal and vertical directions. However, some departure from square pixel shape and pitch may result due to the manufacturing constraints and environmental changes like temperature or mechanical stresses. As shown in next section, a simple diffraction based measurements can be used effectively to discern any meaningful variations from square pixel shape and also horizontal and vertical pitch.

3.4.1 Theoretical Description

The two-dimensional pixelated array of LC panel can be formed by repeating an elementary rectangular aperture of size $(a \times b)$ spaced p and q apart in (ξ, η) plane, respectively, as shown in Figure 3.18. Mathematically it is obtained by the convolution operation between rectangle and comb functions as [170]:

$$t_A(\xi,\eta) = \frac{1}{pq}\left[\text{rect}\left(\frac{\xi}{a}\right) * \text{comb}\left(\frac{\xi}{p}\right)\right]\text{rect}\left(\frac{\xi}{L}\right) \times \left[\text{rect}\left(\frac{\eta}{b}\right) * \text{comb}\left(\frac{\eta}{q}\right)\right]\text{rect}\left(\frac{\eta}{H}\right) \tag{3.18}$$

where, $*$ designates the convolution operation, rect$(\cdot)$ and comb$(\cdot)$ functions have their usual definitions given in Ref [170]. The terms within square brackets in Eq. (3.18) represent step and repeat function which is truncated by finite sized window rect(ξ/L) and rect(η/H). The complex amplitude transmittance of the aperture in Eq. (3.18), when illuminated by a plane monochromatic light of wavelength λ and unit–amplitude, is given by,

$$E_A(\xi,\eta) = t_A(\xi,\eta) \tag{3.19}$$

The field distribution at any point $P(x,y)$ on the screen placed at a distance z away from the aperture plane is given by Fresnel–Kirchhoff diffraction formula [127]:

$$E_o(x,y) = \frac{1}{\mathrm{i}\lambda}\int_{-\infty}^{+\infty}\int_{-\infty}^{+\infty}\frac{\mathrm{e}^{\mathrm{i}kr}}{r}E_A(\xi,\eta)\mathrm{d}\xi\mathrm{d}\eta \tag{3.20}$$

In the far field (Fraunhofer) approximation, Eq. 3.20 becomes:

$$E_o(x,y) = \frac{\mathrm{e}^{\mathrm{i}kz}\mathrm{e}^{\mathrm{i}\frac{k}{2z}(x^2+y^2)}}{\mathrm{i}\lambda z}\mathcal{F}\left\{E_A(\xi,\eta)\right\} \tag{3.21}$$

where

$$\mathcal{F}\left\{E_A(\xi,\eta)\right\} = \int_{-\infty}^{+\infty}\int_{-\infty}^{+\infty}E_A(\xi,\eta)\,\mathrm{e}^{-2\pi\mathrm{i}(f_x\xi+f_y\eta)}\mathrm{d}\xi\mathrm{d}\eta \tag{3.22}$$

is the fourier transform of the transmitted field immediately behind the aperture and $f_x = x/\lambda z$, $f_y = y/\lambda z$ are the spatial frequencies in x and y directions, respectively. Substituting Eq. (3.19) into Eq. (3.22) and using convolution theorem and similarity property of the fourier transforms, the following expression is obtained:

$$\begin{aligned}\mathcal{F}\left\{E_A(\xi,\eta)\right\} = abLH\,&[\mathrm{sinc}(af_x)\mathrm{comb}(pf_x)] * \mathrm{sinc}(Lf_x)\\ &\times[\mathrm{sinc}(bf_y)\mathrm{comb}(qf_y)] * \mathrm{sinc}(Hf_y)\end{aligned} \tag{3.23}$$

Finally, the intensity distribution of the diffraction pattern at the screen is given by,

$$\begin{aligned} I(x,y) &\simeq |E_o(x,y)|^2\\ &= \left|\mathcal{F}\left\{E_A(\xi,\eta)\right\}\right|^2\end{aligned} \tag{3.24}$$

A typical simulation of the intensity diffraction pattern of LC panel is shown in Figure 3.19, where, the pixel size and the pitch are related to modulating sinc and

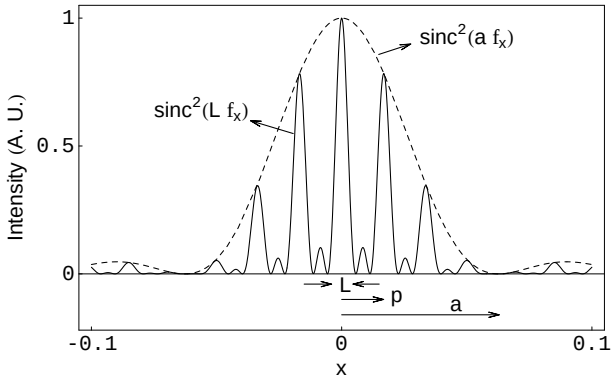

Figure 3.19: Diffraction pattern simulation of LC panel in x-direction.

comb functions, respectively. The influence of different components of LC panel is clearly seen in the diffraction pattern. Now the pixel size can be determined from the condition for minima, i.e., $af_x = 1$ and $bf_y = 1$. Similarly, the expressions for the pitch can be written as,

$$p = \frac{1}{f_x} = \frac{\lambda z}{x}, \text{ and} \tag{3.25}$$

$$q = \frac{1}{f_y} = \frac{\lambda z}{y} \tag{3.26}$$

As expected, the scale inversion from diffracting elements in aperture plane ($L > p > a$ in Figure 3.18) and the width of corresponding intensity peaks in diffraction plane ($1/a > 1/p > 1/L$ in Figure 3.19) is the direct consequence of the Fourier theory.

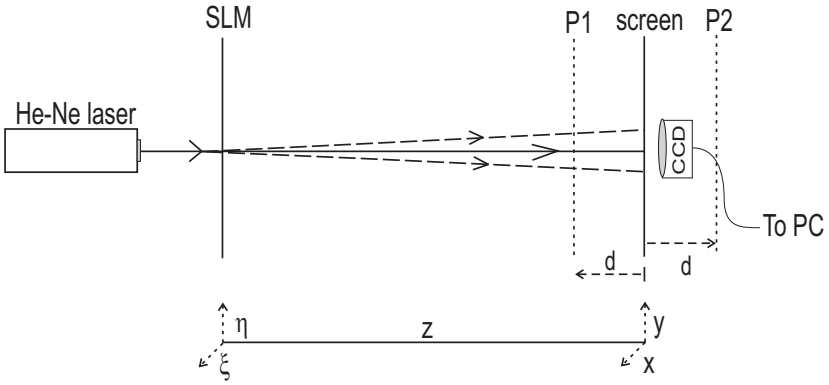

Figure 3.20: Basic layout of experimental setup.

3.4.2 Experimental Technique and Results

The basic experimental schematic to perform the optical diffraction based measurements is shown in Figure 3.20. The SLM is placed at aperture plane $(\xi, \eta, 0)$ and illuminated by normally incident He–Ne laser beam at 543 nm. The diffraction pattern is captured by a computer controlled CCD camera (Pulnix TM-1320-15CL; number of pixels: 1300×1030; pixel size: $6.7 \times 6.7\,\mu$m) placed at a distance z in (x, y) plane. A precise alignment and positioning of all the elements was ensured before making the measurements.

The data was digitally processed and analyzed using National Instruments IMAQ Vision and LabVIEW softwares. In each measurement, 20 frames were captured and averaged to minimize the random noise in detection process. The fringing effect due to coherent illumination of CCD is removed by low pass fourier filtering of the image data. Figure 3.21 shows one of the CCD images of the diffraction pattern obtained after averaging and filtering operation. Discrete artifacts present in the Figure 3.21 are due to downsizing of the image for display purpose. The desired accuracy in distance measurement from aperture plane to the screen may not be possible because of the non availability of an instrument to measure the distance accurately over a longer distance. Further, the hinderance caused by SLM and CCD housing assembly results in an additional uncertainty in determining the exact object and image planes. This limitation is overcome by recording the diffraction pattern at two different planes denoted by P1 and P2 in Figure 3.20. The CCD camera (without imaging lens) is mounted on a micron accuracy translation stage which has a maximum range of 10 mm. If the plane P1 and P2 are at distance $z-d$ and $z+d$, respectively, from the aperture, then the modified expression for pitch (Eq. 3.25) at plane P2 and P1 can be written as,

$$p = \frac{\lambda(z+d)}{x_2} \text{ and} \tag{3.27}$$

$$p = \frac{\lambda(z-d)}{x_1}, \tag{3.28}$$

respectively. By eliminating the z dependence from Eqs. (3.27) and (3.28), the expression for pitch becomes:

$$p = \frac{2\lambda d}{x_2 - x_1} \tag{3.29}$$

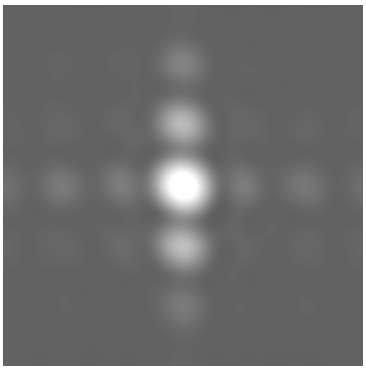

Figure 3.21: CCD image of the LC diffraction pattern after averaging and low pass filtering.

A similar expression obtained for the pitch in y–direction is $q = 2\lambda d/(y_2 - y_1)$. Figure 3.22 shows the intensity line profile along y–direction for a diffraction pattern that is recorded at two different planes at a distance $z+d$ and $z-d$. A centroid detection algorithm was used to locate the intensity peaks and pixel distances in secondary maxima. The pitch values p and q measured in two directions are 31.8 ± 1.3 μm, and 36.8 ± 1.7 μm, respectively. The direct measurement of pixel dimensions a and b from the CCD image was not possible. That is because, the threshold for

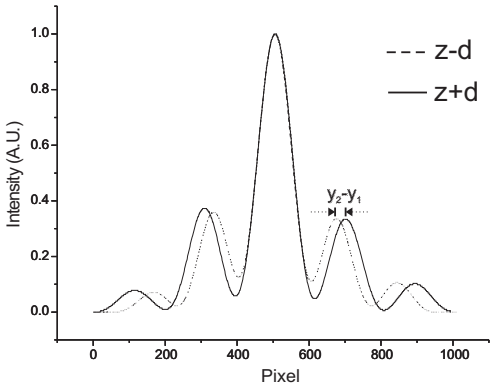

Figure 3.22: Intensity line profile of a diffraction pattern along y-direction, recorded at two different planes that are 10 mm apart.

intensity minima of the modulating $\text{sinc}^2(\cdot)$ function cannot be determined uniquely due to unavoidable background noise. Therefore, a nonlinear best parameter fit

together with measured values of p and q is used to obtain $a \approx 28.6\,\mu$m, and $b \approx 31.6\,\mu$m.

The apparent discrepancy between the square pixel pitch ($\approx 32\,\mu$m) specified by the manufacturer and the experimentally measured values is partly due to anisotropic stress caused by the ambient temperature variations and the protective housing assembly around LC panel. It is also to be noted that the refractive index of LC material and the finite thickness of LC cell have not been taken into account. This, however, will not alter the diffraction pattern in any significant way.

3.5 Conclusions

Spatial light modulator is an important component of the holographic data storage system. The commercially available LC-SLM are usually meant for display applications. The use of SLM in holographic data storage is constrained by several factors such as limited bit depth, finite contrast, pixel size and cross-coupling of phase and amplitude modulations. Therefore, it is imperative to quantify some of these properties in order to optimized the storage performance. In this chapter we have presented the experimental studies pertaining to the operational characteristics of LC-SLM as a function of several parameters. The light transmission properties of TNLC cell were medelled according to the theory presented in the section 3.2. The main conclusions are as follow:

The polarization rotation and birefringence properties of TNLC make it suitable for the intensity and/or phase modulation of the light. However, due to small cell thickness and birefringence, a pure phase-only modulation cannot be realized in TNLC.

The experimentally ascertained values of twist angle for LC2002 model was $\alpha = 90^\circ \pm 0.5^\circ$. The angle of molecular director with respect to lab vertical was found to be $\psi = 45^\circ \pm 0.5^\circ$.

Theoretical and experimental results indicate a highly nonlinear (input/output) response the SLM. This inference can be drawn from the light transmission

properties of the SLM presented in section 3.3.2. In addition, the brightness and contrast settings strongly influence the modulations characteristics of LC2002 model. Intensity modulation curves corresponding to different brightness and contrast control are best described either by the power-law or Sigmoidal functions. The power-law index (γ) can be used to correct the effect of SLM nonlinearities. This can be achieved by applying the inverse-gamma correction to the input grey scale images before addressing to the SLM.

Finally, a simple optical diffraction based technique was implemented to measure the pixel size and pitch of a LC based SLM. Further, the difficulty to measure the distance z in conventional diffraction based experiment is circumvented by two–plane measurements of diffraction pattern which is more accurate and easier to implement. The variations in pixel size and/or pitch can seriously degrade the performance in certain applications where one to one imaging of SLM and CCD pixel is most desired [84, 171]. Any significant departure from a square shaped pixel can be helpful in evaluating the suitability of the LC based SLM for holographic data storage system and adaptive optics based wavefront corrections.

Chapter 4

Holographic Data Storage and Image Compression

Introduction

At basic level, a hologram is a record of the spatial interference pattern formed by mixing of two coherent laser beams. One of the recording beams which carries spatial information is labeled as *object* beam. The other is a plane beam normally distinguished by its particular direction of travel and labeled as *reference* beam. The object beam is reconstructed by illuminating the recorded hologram with the reference beam and vice-versa. In a thick storage medium, the reconstruction becomes very sensitive to the particular angle of incidence of the reference beam, which allows multiple pages to be recorded in the same volume. The data pages can be recorded sequentially, by simultaneously illuminating the photosensitive material with the object beam and its unique reference beam. Each hologram can be a read-out independently by associated reference beam.

A pixel is a smallest unit in a digital image. Associated with each pixel is a number, in the interval $[0, L]$, representing grey level ranging from black (0) to white (L). In a binary image, the pixel value is either 0 or 1. For a *n-bit* grey scale image, a pixel can have value anywhere between 0 (black) and $2^n - 1$ (white). For example, in a 8-bit grey scale image, a pixel may have any integer value between 0 and 255.

A holographic data storage system (HDSS) works fundamentally on a page-oriented architecture that has a tremendous potential to store pictorial (gray scale images) as well as binary data. An optical replica of binary or a grey scale data page is created by liquid crystal based spatial light modulator (SLM).

A general layout of HDSS in shown in Figure 4.1. Two possible schemas exist to store data holographically. An input grey scale images that has more than two brightness levels per pixel can be directly loaded (route I) onto the SLM to compose the object beam. Such a scheme is useful for storing visual images where the quantitative information in the image are not very critical. The direct storage of grey images also improves the over all capacity and the read-out rate of the HDSS without additional complexity [172].

In the second scheme (route II), the integer array of pixel values constituting the *source data* is extracted from the input image. The source data is then encoded into binary form i.e., a sequence of 1s and 0s to form a binary data page. Several

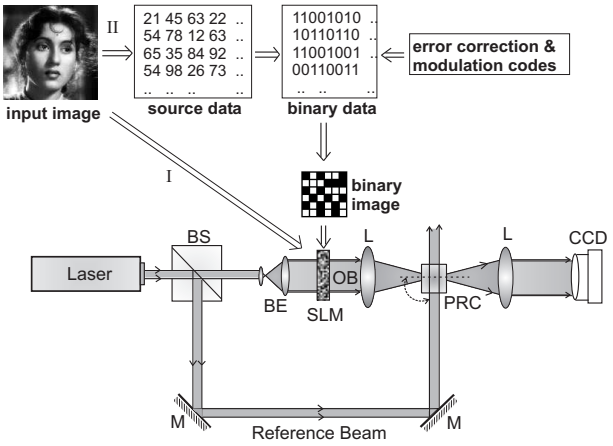

Figure 4.1: A general layout of holographic data storage system.

advanced and powerful error correction codes (ECC) and modulation codes can be implemented to mitigate the effect of noise in the binary data. In fact these coding techniques have become indispensable part of all data storage and communication systems. The ECC and modulation codes are briefly described in section 4.1.

One of the goals of this chapter is to illustrate the image compression scheme for HDSS. In section 4.2, the basic data redundancies that make image compression

possible, are described. The Haar transformation based image compression and its implementation using matrix algebra is explained subsequently. Huffman encoding of binary data is explained next. Image compression algorithm was developed and quantitative results obtained for some of the test images are presented. A block-based mean/median approach is suggested to distinguish between logical 1s and 0s in a CCD captured image. The experimental scheme developed for HDSS is presented in section 4.3.1. The storage of binary and grey scale astronomical images in Fe:Ce:Ti doped $LiNbO_3$ crystal is demonstrated, respectively, in sections 4.3.2 and 4.3.3.

4.1 Error Correction and Modulation Codes

Noise and error sources are mechanisms through which information is either corrupted or lost while recording and/or retrieving the data. For example, packing data bits more densely bring them too closer to each other's proximity such that their boundaries begin to merge. This leads to destructive influence of inter-symbol interference (ISI). In addition, by increasing reading, recording and transfer rate results in distorted data readout. The error is usually quantified by a term known as bit-error rate (BER), defined as the ratio of number of error bits in the output stream to the total number of data bits in the input stream. In a typical storage media, the raw BER is around $10^{-3} - 10^{-4}$. However, the acceptable standard for BER in the present storage devices is of the order of $\approx 10^{-12}$ or better.

The error detection and correction codes are designed to impart certain degree of immunity to the data bits against the noise. It is accomplished by selectively introducing redundant bits into the source data prior to storage. These additional bits (also called overheads) allow detection and correction of bit errors in the retrieved data from the noisy environment. The overhead cost associated with ECC is characterized by the code rate: k/n, where k is source data bits and n is code word length. The coding redundancy is measured by the number of extra bit i.e., $n-k$. Main examples of ECC codes are: parity checks code, Hamming code, Reed-Muller code, Reed-Solomon code and Turbo code [173].

In page oriented data storage system, the occurrence of some of the bit patterns contribute more noise than others. In addition, certain bit pattern may be more suitable for a given detection scheme. Therefore, the purpose of modulation codes is to permit the appearance of selective patterns in the binary data page and inhibit the pattern that are more prone to noise. In a $p : q$ modulation code; p is the length of source bits and $q-p$ is the number of extra or overhead bits required to achieve the desired modulation. The overhead is usually described in terms of code ratio, $p/q < 1$.

The error correction and modulation codes, though extremely useful in preserving the data fidelity, have undesirable effects on the storage capacity of the medium due to increased overhead rates. The effective storage capacity of the system drastically reduces due to inclusion of overhead data. One of the ways to overcome this limitation is to compress the source data before applying the ECC and modulation codes. Efficient data compression algorithms can effectively compensate for the overhead penalty paid in ECC and modulation coding. The objective of data compression is to reduce the number of bits required to convey the useful information in a source data. The data compression is possible because most real-world data is statistically redundant. The implementation of Several ECC and modulation codes for holographic memories have already been demonstrated in the past [63, 70–72, 74, 174]. Without taking further recourse to ECC and modulation codes, the next section explains the principle of image compression.

4.2 Image compression

An image is a two-dimensional representation of some physical data or signal which conveys some meaningful information. The image compression addresses the issue of reducing the amount of data required to represent a digital image. Most of the natural images have certain statistical properties which can be exploited to achieve the compression. Different amount of data may be used to convey the same information. In that sense, the extraneous data that does not provide any new or extra information leads to data redundancy. The underlying basis of the reduction

process is to remove the data redundancy. In most of the digital images, three types of data redundancies can be identified. These are: interpixel redundancy, coding redundancy and psychovisual redundancies.

Interpixel redundancy arises from the correlation among the pixels due to structural or geometrical similarities between the objects in the image. In such a case, it is possible to approximate a pixel value from the neighbouring pixels. The interpixel redundancy in an image can be reduced by transforming the two-dimensional pixel array into a more efficient and often nonvisual format. This is discussed in section on Haar transform.

Usually in a digital image, the number of bits used for the representation of each pixel is constant for all the pixels, regardless the value of the pixel and the frequency of occurrence of that value in the image. In most of the natural images, certain grey levels are more likely to occur than others. Which means the histograms of most of the images are non-uniform. This is illustrated in Figure 4.2, where four different images are shown along with their respective histograms. An image will contain a *coding redundancy* if the grey levels are encoded in such a way that uses more code symbol or bits than absolutely necessary to represent a grey level. For example, a natural binary coding assigns fixed number of binary bits to encode both the most and the least probable grey levels. The coding redundancy can be overcome by *variable-length* encoding, where, fewer number of bits are assigned to more probable grey level values than the less probable ones. Huffman coding discussed in later section, is an example of variable-length coding.

The human visual system does not have equal sensitivity for all the visual information in an image. Therefore, information that are redundant for visual perception, give rise to *psychovisual redundancy.* For example, human eye cannot distinguish between a 16-bit and a 24-bit grey scale or colour image. The reduction of psychovisual redundancy may results in quantitative loss of information.

An image is represented as a 2-dimensional array of integers, each integer representing the brightness level at a given point. Mathematical transformations can be applied to an image so as to obtain information that are not readily available in the original image. There are several types of transformations. Most commonly

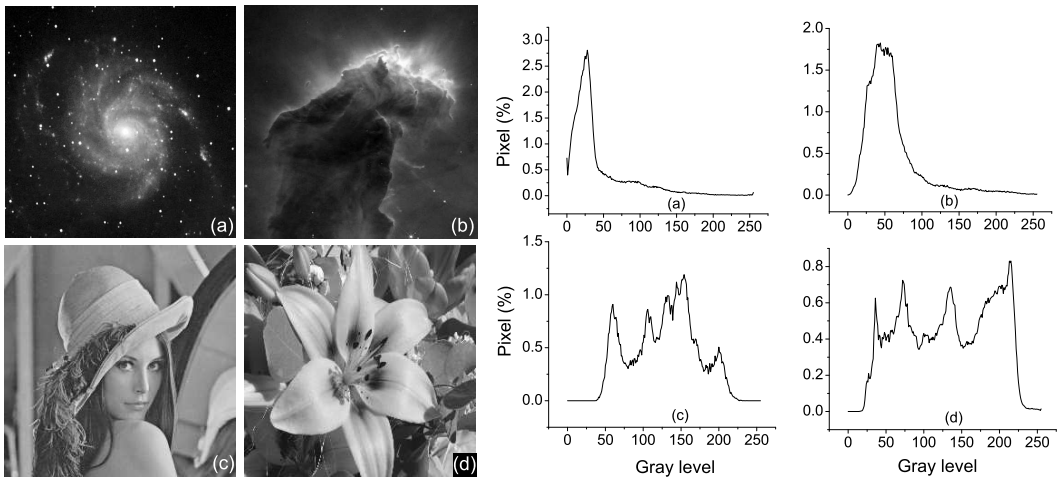

Figure 4.2: Gray scale images and their corresponding histograms distribution (a) M101 galaxy, (b) Eagle nebula, (c) Lena image and (d) Lily flower.

known discrete Fourier transform (DFT) are used for extracting frequency domain information from the data. Another example is the discrete cosine transform (DCT) which is extensively used in JPEG image compression and MPEG video compression [175, 176].

In last few years, the research in wavelet transform has made a tremendous impact in medicine, astronomy, geophysics and information theory [177]. The wavelet transform has been proved particularly useful in image compression and progressive transmission of the digital images over internet [178,179]. Wavelets are functions defined over a finite interval with average value of zero. Therefore, in wavelet transform a function is represented as a superposition of a set of wavelets or basis functions.

The main advantage of wavelet transforms over other more traditional decomposition methods (like the DFT and DCT) is that the basis functions associated with a wavelet decomposition typically have both low and high frequency support. The basis functions with low frequency support are effective for representing slow variations in an image while the basis functions with high frequency support can efficiently represent sharp transitions (i.e., edges). The basis functions associated with traditional transforms such as DFT and DCT, cannot handle simultaneously the slow and fast frequency spatial variations in the same image.

4.2.1 Image Compression Using the Haar Transform

Although there are numerous number of wavelet transforms available, but the Haar transform (also known as H-transform or the S-transform) is commonly employed and simple to implement in data compression techniques. The method is to first apply the appropriate Haar transformation to the image data to obtain transformed data. The transformed data contains large number of small or zero–valued coefficients which are often easier to code than the original data itself. Here, the discussion is confined to practical implementation of Haar transform for compressing digital images. The mathematical formulism and relevant details are discussed in several texts available on the subject [180–182].

Method of *averaging and differencing*

The Haar transform exploits the statistical redundancy or pixel correlation present in the natural images to achieve data compression. It uses a very simple method of *averaging and differencing* to manipulate the image data. The following example illustrates the the process of *averaging and differencing*:

y	128	120	124	132	124	120	112	116
y_1	124	128	122	114	4	-4	2	-2
y_2	126	118	-2	4	4	-4	2	-2
y_3	122	4	-2	4	4	-4	2	-2

Average Coefficients (sum of pair/2)
Detail coefficients (difference of pair/2)

Let y be an array of 8 numbers listed in the above table. The first four entries in row y_1 (shown in dark grey) corresponds to the pairwise average of numbers in y, whereas, the second four entries (shown in light grey) are the difference of each pair divided by 2. In other words, it is the difference between the first number in each pair and the corresponding average. The process of *averaging and differencing* is repeatedly applied to the *average coefficients* of previous row without altering the *detail coefficients*. Finally, in row y_3 there is only one average coefficient and rest

all are *detail coefficients*. Three steps were needed to obtain y_3 from y. In general, n number of steps are required to achieve *averaging and differencing* of an array of length 2^n.

Matrix Algebra for *averaging and differencing*

Computationally, the three-stage transformation from y_1 to y_3 can be carried out more efficiently with matrix algebra. That is,

$$\begin{aligned} y_1 &= A_1 \cdot y \\ y_2 &= A_2 \cdot y_1 \\ y_3 &= A_3 \cdot y_2 \end{aligned} \tag{4.1}$$

where A_1, A_2 and A_3 are 8×8 Haar matrices defined as:

$$A_1 = \begin{pmatrix} 1/2 & 0 & 0 & 0 & 1/2 & 0 & 0 & 0 \\ 1/2 & 0 & 0 & 0 & -1/2 & 0 & 0 & 0 \\ 0 & 1/2 & 0 & 0 & 0 & 1/2 & 0 & 0 \\ 0 & 1/2 & 0 & 0 & 0 & -1/2 & 0 & 0 \\ 0 & 0 & 1/2 & 0 & 0 & 0 & 1/2 & 0 \\ 0 & 0 & 1/2 & 0 & 0 & 0 & -1/2 & 0 \\ 0 & 0 & 0 & 1/2 & 0 & 0 & 0 & 1/2 \\ 0 & 0 & 0 & 1/2 & 0 & 0 & 0 & -1/2 \end{pmatrix};$$

$$A_2 = \begin{pmatrix} 1/2 & 0 & 1/2 & 0 & 0 & 0 & 0 & 0 \\ 1/2 & 0 & -1/2 & 0 & 0 & 0 & 0 & 0 \\ 0 & 1/2 & 0 & 1/2 & 0 & 0 & 0 & 0 \\ 0 & 1/2 & 0 & -1/2 & 0 & 0 & 0 & 0 \\ 0 & 0 & 0 & 0 & 1 & 0 & 0 & 0 \\ 0 & 0 & 0 & 0 & 0 & 1 & 0 & 0 \\ 0 & 0 & 0 & 0 & 0 & 0 & 1 & 0 \\ 0 & 0 & 0 & 0 & 0 & 0 & 0 & 1 \end{pmatrix} \text{ and}$$

$$A_3 = \begin{pmatrix} 1/2 & 1/2 & 0 & 0 & 0 & 0 & 0 & 0 \\ 1/2 & -1/2 & 0 & 0 & 0 & 0 & 0 & 0 \\ 0 & 0 & 1 & 0 & 0 & 0 & 0 & 0 \\ 0 & 0 & 0 & 1 & 0 & 0 & 0 & 0 \\ 0 & 0 & 0 & 0 & 1 & 0 & 0 & 0 \\ 0 & 0 & 0 & 0 & 0 & 1 & 0 & 0 \\ 0 & 0 & 0 & 0 & 0 & 0 & 1 & 0 \\ 0 & 0 & 0 & 0 & 0 & 0 & 0 & 1 \end{pmatrix}$$

Each column in the matrix is a Haar basis, which are orthogonal to each other. The set of operations in Eq. (4.1) can all be carried out in just one step:

$$y_3 = y \cdot W, \tag{4.2}$$

where $W = A_1 \cdot A_2 \cdot A_3$ is called transformation matrix. Since each column of A_is that comprise W are orthogonal to every other, the matrices are also invertible, i.e., $W^{-1} = A_3^{-1} \cdot A_2^{-1} \cdot A_1^{-1}$. Therefore, the original data can be recovered using inverse transformation:

$$y = y_3 \cdot W^{-1} \tag{4.3}$$

4.2.2 An Example

Now a more realistic example of an 8-bit grey scale image of the Eagle Nebula is considered. A 8×8 pixel block extracted from Eagle Nebula is shown in Figure 4.3. Each square is shaded according to its grey level value.

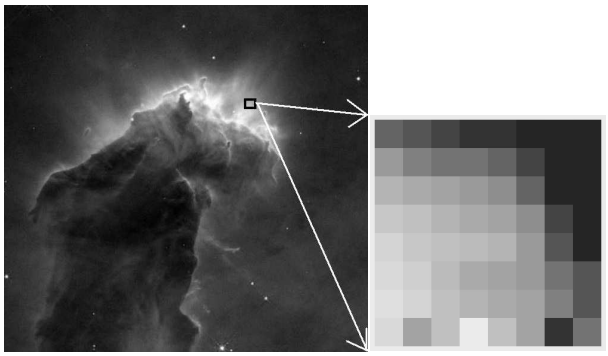

Figure 4.3: A 8×8 pixel block extracted from Eagle Nebula.

The corresponding 8×8 pixel matrix P is:

$$P = \begin{pmatrix} 115 & 114 & 113 & 112 & 112 & 110 & 106 & 103 \\ 119 & 117 & 116 & 116 & 115 & 113 & 109 & 105 \\ 122 & 121 & 120 & 119 & 118 & 115 & 111 & 108 \\ 125 & 124 & 122 & 121 & 120 & 118 & 113 & 110 \\ 127 & 125 & 124 & 123 & 122 & 119 & 114 & 111 \\ 128 & 126 & 123 & 121 & 120 & 119 & 116 & 114 \\ 129 & 127 & 124 & 122 & 121 & 120 & 117 & 114 \\ 128 & 120 & 124 & 132 & 124 & 120 & 112 & 116 \end{pmatrix}$$

The row transformed matrix Q is obtained by right multiplying P by transformation matrix W.

$$Q = \begin{pmatrix} 110.62 & 2.87 & 1.00 & 3.25 & 0.50 & 0.50 & 1.00 & 1.50 \\ 113.75 & 3.25 & 1.00 & 3.50 & 1.00 & 0.00 & 1.00 & 2.00 \\ 116.75 & 3.75 & 1.00 & 3.50 & 0.50 & 0.50 & 1.50 & 1.50 \\ 119.12 & 3.87 & 1.50 & 3.75 & 0.50 & 0.50 & 1.00 & 1.50 \\ 120.62 & 4.12 & 1.25 & 4.00 & 1.00 & 0.50 & 1.50 & 1.50 \\ 120.87 & 3.62 & 2.50 & 2.25 & 1.00 & 1.00 & 0.50 & 1.00 \\ 121.75 & 3.75 & 2.50 & 2.50 & 1.00 & 1.00 & 0.50 & 1.50 \\ 122.00 & 4.00 & -2.00 & 4.00 & 4.00 & -4.00 & 2.00 & -2.00 \end{pmatrix}$$

After getting the row transformed matric Q, a similar transformation can be applied to columns by left multiplying Q with W^T. The result is:

$$T = W^T \cdot P \cdot W = \begin{pmatrix} 118.19 & 3.66 & 1.09 & 3.34 & 1.19 & 0.00 & 1.12 & 1.06 \\ -3.12 & -0.22 & 0.03 & 0.16 & -0.56 & 0.37 & 0.00 & 0.56 \\ -2.87 & -0.37 & -0.12 & -0.12 & 0.12 & -0.12 & -0.12 & 0.12 \\ -0.56 & 0.00 & 0.81 & -0.06 & -0.75 & 1.12 & -0.12 & 0.75 \\ -1.56 & -0.19 & 0.00 & -0.12 & -0.25 & 0.25 & 0.00 & -0.25 \\ -1.19 & -0.06 & -0.25 & -0.12 & 0.00 & 0.00 & 0.25 & 0.00 \\ -0.12 & 0.25 & -0.62 & 0.87 & 0.00 & -0.25 & 0.50 & 0.25 \\ -0.12 & -0.12 & -2.25 & -0.75 & -1.50 & 2.50 & -0.75 & 1.75 \end{pmatrix}$$

Threshold and Rounding-off

The new matrix T is called the Haar transformed matrix. The coefficients with low values in Haar transformed matrix T correspond to those regions in the original image where pixel to pixel variations are small. To exploit the real power of Haar transform for data compression, two more steps are needed. First, round off the real coefficients in T to nearest integer and second, select an appropriate threshold ε and set all the coefficients in T to zero whose absolute value is below ε. Let $|\varepsilon| = 2$ This will result in new matrix S:

$$S = \begin{pmatrix} 118 & 4 & 0 & 3 & 0 & 0 & 0 & 0 \\ -3 & 0 & 0 & 0 & 0 & 0 & 0 & 0 \\ -3 & 0 & 0 & 0 & 0 & 0 & 0 & 0 \\ 0 & 0 & 0 & 0 & 0 & 0 & 0 & 0 \\ 0 & 0 & 0 & 0 & 0 & 0 & 0 & 0 \\ 0 & 0 & 0 & 0 & 0 & 0 & 0 & 0 \\ 0 & 0 & 0 & 0 & 0 & 0 & 0 & 0 \\ 0 & 0 & -2 & 0 & 0 & 3 & 0 & 0 \end{pmatrix}$$

The matrix S is called *sparse matrix* because most of its elements are zeros. Forcing too many detail coefficients to zero may cause the image degradation as will be seen later. However, it becomes much easier to store or transmit the sparse matrices. For example, in present case we only need to store 7 nonzero coefficients along with their position indices as compared to 64 numbers in original matrix. Apart from storing the coefficients and their indices there are several other ways to store the sparse matrices efficiently [183, 184]. But the next question of immediate concern is: how well the original matrix P can be reconstructed from the sparse matrix S? Applying the inverse transformation given by Eq. (4.3), i.e., $P' = W \cdot S \cdot W^{-1}$, we get

$$P' = \begin{pmatrix} 116 & 116 & 116 & 116 & 111 & 111 & 105 & 105 \\ 116 & 116 & 116 & 116 & 112 & 111 & 105 & 105 \\ 122 & 122 & 122 & 122 & 116 & 117 & 111 & 111 \\ 122 & 122 & 122 & 122 & 116 & 117 & 111 & 111 \\ 125 & 125 & 125 & 125 & 120 & 120 & 114 & 114 \\ 125 & 125 & 125 & 125 & 120 & 120 & 114 & 114 \\ 127 & 127 & 126 & 120 & 120 & 120 & 114 & 114 \\ 123 & 123 & 124 & 130 & 120 & 120 & 114 & 114 \end{pmatrix}$$

The matrix P' is a fairly good approximation of the original matrix P, considering the enormous reduction in the number of nonzero entries in S. The algorithm is applied to the entire image by taking 8×8 pixel block at a time. For this algorithm to work, the image size $(M \times N)$ should be divisible by the size (8×8) of Haar matrices. Zero padding may be required for the images which do not meet this criteria.

Loss–less and Lossy Compression

Image compression is generally divided into two categories: loss-less and lossy compression. If the reconstructed image is identical to the original image then the compression is lossless, otherwise it is called lossy compression.

$$\varepsilon = \begin{cases} 0 \text{ then } S = T \text{ results in loss–less compression,} \\ > 0 \text{ some of the elements of } T \text{ are reset to zero} \\ \qquad \text{which leads to image distortion or lossy compression.} \end{cases}$$

The degree of compression is measured by reduction ratio r as,

$$r = \frac{\text{Number of non–zero entries in transformed matrix } T}{\text{Number of non–zero entries in } S} \tag{4.4}$$

In the case of lossy compression, the reconstructed image is only an approximation to the original. The difference between the original and reconstructed image is referred to as approximation error or distortion. Although there are many criteria to quantify distortion, but, the most commonly used are *root-mean-square* error $E_{\text{rms}}(i,j)$ defined as [185]:

$$E_{\text{rms}}(i,j) \quad = \quad \left[\frac{1}{MN}\sum_{i=1}^{M}\sum_{j=1}^{N}[f(i,j) - f'(i,j)]^2\right]^{1/2}; \tag{4.5}$$

where, $f(i,j)$ is an input image and $f'(i,j)$ is an approximate image obtained after compression.

A programming code was written in LabVIEW (see appendix) to implement the Haar transformed based image compression algorithm. The main function of the program is to:

- extract the 2-dimensional array of pixel values from a grey scale image,
- apply the Haar transform to the image data,
- reset the coefficients of Haar transformed matrix to zero according to specified threshold ε,
- apply the inverse Haar transform to reconstruct the image and
- calculate the reduction ratio r and the *root-mean-square* error.

Four test images namely, M101 galaxy, Eagle nebula, Lena and Lily (flower) were chosen to illustrate the effect of thresholding ε on the visual image quality, compression ratio r, *root-mean-square* error E_{rms} and average code length L_{Avg}. The size of each image was 524×524 pixels. The reconstructed images at $\varepsilon = 1, 10, 25, 50$ threshold are shown in Figure 4.4. A severe degradation in form of discrete blockiness can be noticed at higher thresholds. Therefore, the compression ratio has to be compromised to keep the image quality within acceptable limit.

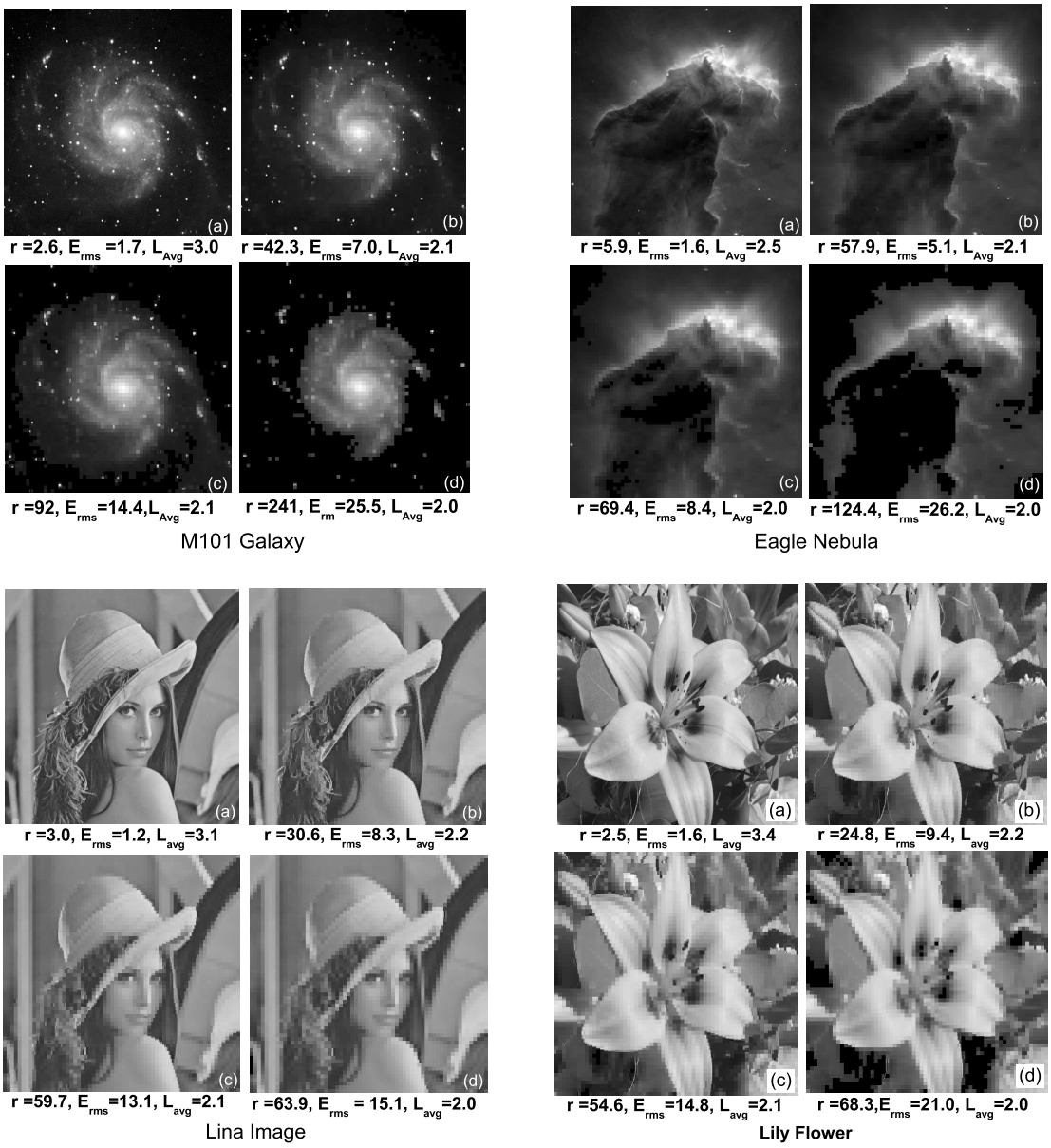

Figure 4.4: The effect of threshold ε on r, E_{rms}, L_{Avg} (bits/pixel) and the visual image quality of four representative images. (a) $\varepsilon = 1$, (b) $\varepsilon = 10$, (c) $\varepsilon = 25$ and (d) $\varepsilon = 50$.

The computed variation of r and E_{rms} with threshold ε is shown in Figure 4.5. The effect of compression can be more disastrous when the images cannot be evaluated just based on visual assessment. Apart from visual quality, the astronomical images, for example, are also subjected to rigorous and systematic quantitative analysis. The astrometric measurements of point sources may require sub–pixel positional accuracy. The accuracy in photometric measurements of astronomical objects is sometimes limited only by sky background and detector response. The presence of noise in the images makes the compression less effective and inefficient. This is particularly true with astronomical images.

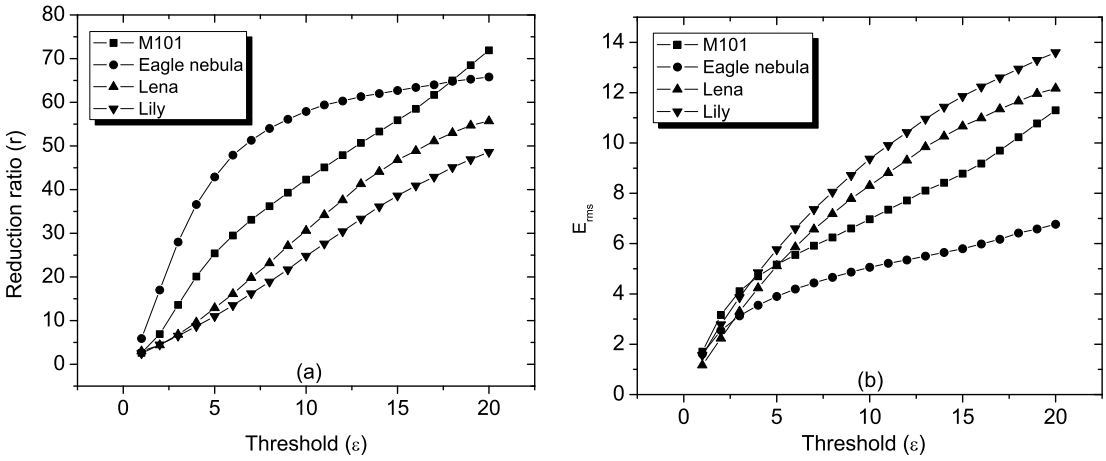

Figure 4.5: The variation of (a) reduction ratio r and (b) root-mean-square error E_{rms} with threshold ε.

Except for occasional extended sources, a typical astronomical image consists of a flat background and scattered point sources. The sky background is forced to a constant value once the threshold is applied. This leads to the possibility of loosing information about the objects that are near detection limit. In addition, the information about the local variations in sky brightness may be lost. All these can severely limit the accuracy of photometry and astrometry of the faint objects. Despite of all these limitations, astronomical images can still be compressed efficiently due to very high degree of inter-pixel correlation compared to other natural images [186–188].

4.2.3 Binary Encoding

At most basic level the data storage and transmission take place in binary form, i.e., the data is converted into a stream of 1s and 0s prior to transmission or storage. To increase the storage capacity and transmission speed, it is important to minimize the number of bits that represent a signal or an image. For example, in natural or fixed length binary coding, a 256×256 pixel, 8-bit grey scale image would require $256 \times 256 \times 8 = 524288$ bits to store or transmit the image.

Symbol (G.L.)	8-bit binary code
11	00001011
246	11110110
125	01111101
31	00011111

Is it possible to reduce the total number of bits representing a image or a signal? The question has been partly answered while discussing the coding redundancy. Consider some arbitrary pixel values (e.g., 11, 246, 125, 31) shown in the first column of the above table. The corresponding 8-bit binary code is listed in second column of the table. The greyed out 0's to the left of each code, constitute fixed length coding redundancy. These bits are not required for decoding the binary number back to decimal form. The fixed length coding redundancy can be lifted using *variable length encoding*. The most prominent examples of variable length encoding are Huffman and arithmetic coding [189, 190]. The Huffman coding is briefly introduced in the next section. The process of reducing the coding redundancy from a Haar transformed image (discussed in previous section) will be extended further.

Huffman Coding

Huffman coding is an error-free, loss-less coding. It uses variable length encoding to give smallest possible bit rate i.e., the number of bits per grey level. The goal is to assign lesser number of bits to most frequently occurring grey levels in the image and more bits to the grey levels that appear less frequently.

This is much easier to demonstrate by taking a hypothetical case of an image. Let's denote the six grey levels (sometimes also called source symbols) of the image by $x_1, x_2, \ldots x_6$. Next the normalized histogram (the number of pixels with a given grey level/total number of pixels in the image) of the image is calculated. This gives the probability p_i of

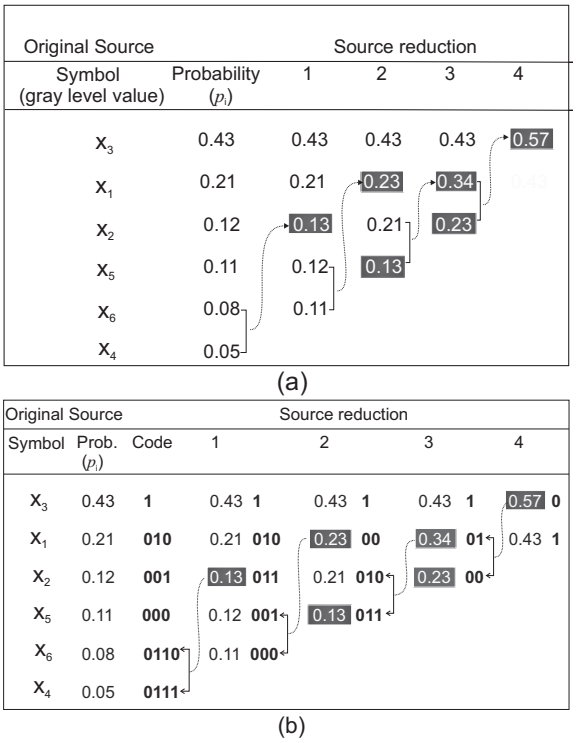

Figure 4.6: Example of binary Huffman coding (a) source reduction process and (b) assigning binary codes to the source symbols.

occurrence of ith grey level. Arrange the probabilities p_is and their corresponding source symbols in the descending order as shown in Figure 4.6(a). The *reduction process* begins by adding probabilities of two least probable grey levels –in this case 0.08 and 0.05. Sort p_i s again to get the entries in column 1 under the source reduction. The process of adding last two numbers and rearranging them in next column after sorting, is repeated until only two entries are left. For clarity, in Figure 4.6 , the added probabilities are highlighted by grey boxes around. In the present example, the last reduction process has resulted in 0.57 and 0.43 in column 4 under the source reduction.

Once the source reduction is complete, the next step is to assign `0` and `1` bit to the two numbers left in last reduction process. To begin with, the choice of selecting the number and the corresponding bit is arbitrary. For example, in Figure 4.6(b), bit `0` was assigned to 0.57 and bit `1` was assigned to 0.43. Noticing that 0.57 was obtained by adding the last two number 0.34 & 0.23 in 3rd reduction process. So the code `01` for 0.34 and `00` for 0.23 is derived by appending `1` and `0` bit to the right of the code of 0.57, i.e., `0`. Again the choice was arbitrary. The process of appending either 0 or 1 to the right of previous

code in the subsequent steps continues until each source symbol is uniquely encoded. All the steps are clearly indicated in Figure 4.6(b).

Now consider Huffman encoded data stream of 1s and 0s. Each symbol have variable number of bits. So how to separate one symbol from the next? The answer lies in the unique prefix property of each source code, That is, no code is a prefix to any other code. Therefore, decoding is trivial as long as the coding table is available. The average code length L_{avg} for Huffman encoded data can be calculated using the following formula [185]:

$$L_{\text{avg}} = \sum_{i=1}^{n} p_i(\mathrm{x}_i)\; l_i(\mathrm{x}_i) \tag{4.6}$$

where, n is number of source symbols or grey levels in the image, p_i is the probability of occurrence, and l_i is the code length of symbol x_i . As an example, Huffman encoded binary data stream: $0111010011001101\cdots$ corresponds to symbols $\mathrm{x}_4, \mathrm{x}_1, \mathrm{x}_6, \mathrm{x}_6, \mathrm{x}_3 \cdots$ in Figure 4.6(b). Therefore, the average code length is:

$$\begin{aligned} L_{\text{avg}} &= \sum_{i=1}^{6} p_i(\mathrm{x}_i)\; l_i(\mathrm{x}_i) = 0.43\times 1 + 0.21\times 3 + 0.12\times 3 + 0.11\times 3 + 0.08\times 4 + 0.05\times 4 \\ &= 2.27 \text{ bits/pixel} \end{aligned}$$

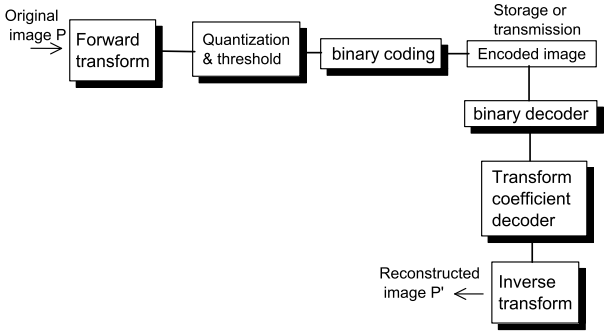

Figure 4.7: Flow diagram showing the image compression scheme for HDDS.

A Huffman coding algorithm was developed using *Mathematica* for reducing the Haar transformed image data to an optimized binary codes. The calculated average code length L_{Avg} bits/pixels for the four test images is also indicated in Figure 4.4.

A brief summary of image compression scheme for HDSS discussed so far is outlined in the flow diagram shown in Figure 4.7.

4.3 Data Storage

4.3.1 Experimental Scheme

A *transmission geometry* for holographic data storage where two recording beams were incident on the same face of the storage medium, is shown in Figure 4.8. The description of main components used in storage geometry is as follows:

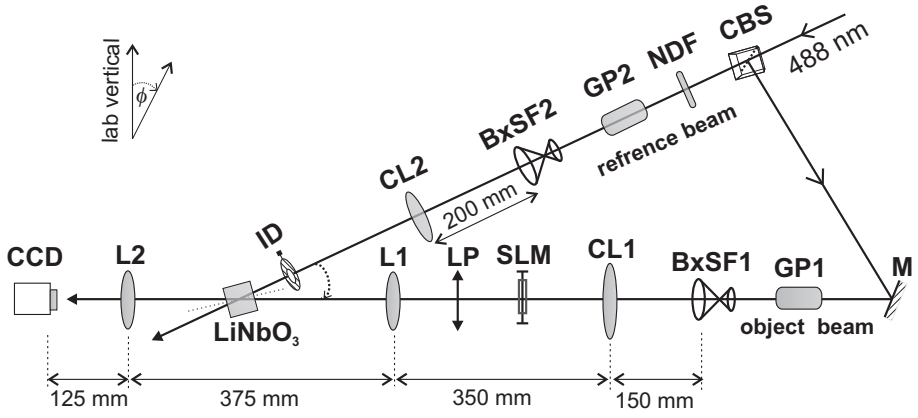

Figure 4.8: The schematic diagram of holographic data storage system in the lab.

CBS: a non-polarizing Cube Beam Splitter that splits the laser beam into object and reference beams

NDF: a compensating Neutral Density Filter required to equalized the object and the reference beam intensities

GP1: Glan laser Polarizer (extinction ratio $> 10^{-6}$) with transmission axis at $-45°$ with lab vertical

GP2: Glan laser Polarizer (extinction ratio $> 10^{-6}$) with transmission axis along lab vertical

BxSF1: three axis Beam eXpander and Spatial Filter assembly with 40x microscope objective and 5 μm pin hole

BxSF2: three axis Beam eXpander and Spatial Filter assembly with 20x microscope objective and 10 μm pin hole

CL1: Collimating Lens (diameter = 50.8 mm and focal length = 150 mm)

CL2: Collimating Lens (diameter = 25.4 mm and focal length = 200 mm)

SLM: Spatial Light Modulator –the page composer

LP: Linear Polarizer (extinction ratio $> 10^{-5}$, diameter = 50.8 mm) with transmission axis at $+45^{\circ}$ with lab vertical

L1: achromatic doublet Lens (diameter = 38.1 mm, focal length = 250 mm)

L2: achromatic triplet Lens (diameter = 38.1 mm, focal length = 125 mm)

CCD: Charge Coupled Device camera

ID: Iris Diaphragm

Both, the SLM and the CCD camera were independently controlled by separate computers. The SLM was a 832×624 pixel array addressed by analog signal produced by the video graphics card of the PC. The CCD camera was placed on a x-y translation stage that had independent tip, tilt and rotation controls. CCD and SLM pixels are on $\approx 7\,\mu$m and $\approx 32\,\mu$m grid, respectively. The SLM and CCD pixel sizes differ by over a factor of 4. Therefore, one-to-one matching between the SLM and the CCD pixels was ruled out. In the present optical set-up, the spatially modulated SLM beam was demagnified by half. Even then, only central $\approx 540 \times 430$ SLM pixels could be seen by CCD camera. The angle between the object beam and the reference beam was $\approx 25^{\circ}$. Figure 4.9 shows the actual photograph of HDSS taken during the experiment.

Fourier Image–Plane Recording Geometry

In the recording scheme shown in Figure 4.8, the lens L1 takes the Fourier transform of the object beam. The crystal is placed at the Fourier image-plane where the reference beam interferes with the Fourier-transformed object beam. The lens L2 performs the inverse Fourier transforms before imaging the object beam back onto the CCD camera. The hologram recording in Fourier image-plane geometry has two distinct advantages over direct image-plane recording [79]. First, the Fourier transform of an image is confined into

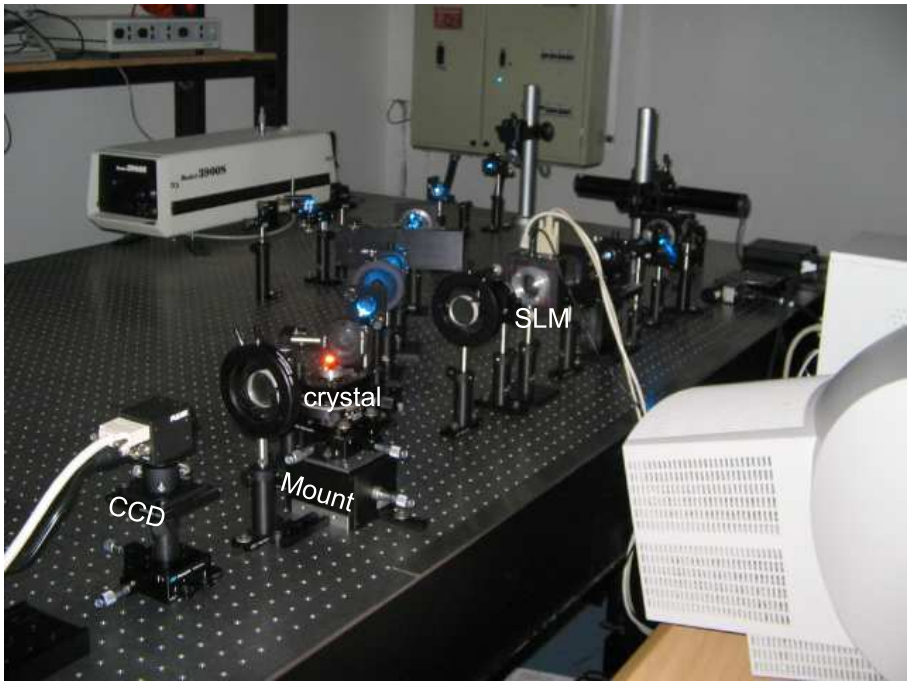

Figure 4.9: A photograph of holographic data storage and retrieval system in the lab.

a very small region which result in a high storage density. Second, the recording in Fourier image-plane geometry is less sensitive to mechanical vibrations and hence more preferable.

This geometry has one severe drawback due mainly to the highly nonuniform distribution of light at the Fourier image-plane [170]. The strong low frequency components near center, saturate the recording material locally, whereas, the finer details of the image that are present in high frequency components, are poorly registered. Eventually, the quality of reconstructed image suffers from undesired low-pass blur and distortions. The problem of strong dc component in the present case, is partly avoided by placing the recording material not exactly at the Fourier image-plane, but slightly away from it.

Spatial and Rotational Multiplexing

The crystal was mounted on a modular platform that was designed to store multiple data pages using spatial and rotational multiplexing. The platform comprises a rotational mount seated on a x–y translation stage, which in turn was placed on a vertical stage. The motion of each stage was controlled by independent actuators with micron level accuracy. The storage medium was a 0° cut Fe:Ce:Ti doped $LiNbO_3$ (size = $10\,\text{mm} \times 10\,\text{mm} \times 10\,\text{mm}$). The crystal was divided into 18 (9×2) spatial locations as shown in Figure 4.10. The front-

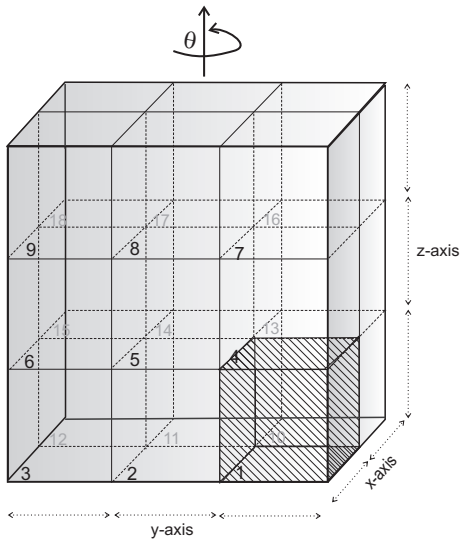

Figure 4.10: Partition of the crystal to implement spatial and rotational multiplexing.

half of the crystal that faces the recording beams contains the spatial blocks marked from 1–9. One such block is shown by cross-hatched region designated by 1. The spatial blocks in the rear-half are marked from 10–18. Since the angle between object and reference beams was fixed at $\approx 25°$, the overlap region between two interfering beams remains fixed in space. Therefore, the spatial multiplexing was achieved by positioning different spatial blocks of the crystal into the beam overlap region using $x-y$ micro-positioning linear stages. A stack of holograms can be recorded at a given block location by incrementally rotating the crystal about the vertical axis. In a simple addressing scheme, each stored image can be identified by a unique dyad (R, θ), where R is index designating spatial location and θ is rotational position during the hologram recording at R. In the present case, R varies from 1–18 and θ from $1° - 6°$.

4.3.2 Storage of Binary Images in Fe:Ce:Ti $LiNbO_3$

This section illustrates the storage of compressed binary data in photorefractive Fe:Ce:Ti $LiNbO_3$ crystal. In hologram writing, the incident laser beam was divided into two equal parts at the cubic beam splitter. A spatially filtered object beam ($\lambda = 488$ nm) was collimated by a 50 mm diameter lens. The collimated beam overfills the SLM aperture. This helps in maintaining beam uniformity across the beam. The lens L1 takes the Fourier transform of the object beam. To prevent the local saturation of the medium due to intense dc term, the crystal was place ≈ 1.5 cm behind the Fourier image-plane.

Table 4.1: Details of formatted binary pages.

Image	size (blocks)	L_{avg} (bits/pixel)	$c_{\min}$
M101 galaxy	129×129	4.23	-60
Eagle nebula	123×123	3.93	-48
Lena	138×138	5.21	-59
Lily	145×145	5.34	-51

Here, we have taken a resized version (64×64 pixel) of the original (512×512 pixel) four test images that were shown Figure 4.2. To store the compressed binary image data

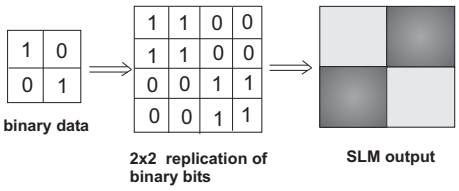

Figure 4.11: Representation of binary data on SLM using 2×2 replication of original bits.

holographically, a binary data page was composed as follows:

- ▷ The image data was Haar transformed as explained in section 4.2.
- ▷ For loss-less compression, the threshold ε was set to zero.
- ▷ The negative coefficients in Haar transformed data were up-shifted (made positive) by adding a number $c_{\min}$ to each coefficient, where $c_{\min}$ was largest negative coefficient in the Haar transformed data.
- ▷ *Up-shifted* Haar coefficients were replaced by corresponding minimum length binary codes obtained using Huffman encoding method. The resulting 1-dimensional bit stream had N elements.
- ▷ Huffman encoded streams of 1s and 0s was partitioned into two-dimensional square page of size $l \times l$. Here, $l = \sqrt{N}$. For l to be an integer, N needs to be padded with additional 0s.
- ▷ Each data bit on SLM was represented by 2×2 replication of original binary bits as shown in Figure 4.11. SLM pixels were transparent for white blocks representing 1s and opaque for greyed-out blocks representing 0s. Table 4.1 shows the details of formatted binary page for each test image.

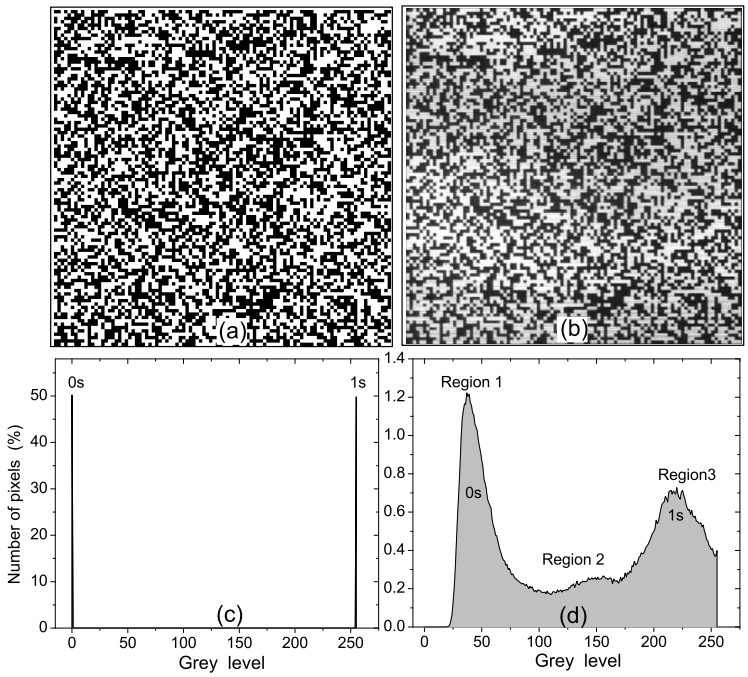

Figure 4.12: (a) The input binary image, (b) binary image displayed on SLM, (c) histogram of input binary image and (d) histogram for SLM displayed binary image.

In order to erase the previously written gratings, the crystal was continuously heated at about 190°C for more than 12 hours in a temperature controlled oven. Several experimental tests were performed with randomly generated binary images of different size to develop a reliable method to extract bit information from the recorded images. One of the methods is described next.

Distinguishing Logical 1s and Logical 0s

SLM transforms the binary data page into an array of bright and dark blocks in the object beam. Ideally, the SLM and associated optics should modulate the object beam to give best possible contrast and uniformity. That is, the logical 1s should corresponds to high intensity blocks (bits) while the logical 0s should result in completely dark blocks. However, several factors such as detector noise, scattering due to material imperfection, interpixel and interpage interference, lens abberations, SLM and CCD pixel mismatch etc., cause light to enter from brighter regions to darker regions. Therefore, the output of a CCD detector is an array of integers proportional to cumulative light intensity arriving at each of the pixel in the sensor. As a result, a binary images captured by CCD would

show a continuous brightness distribution.

Figure 4.12(a) shows a randomly generated 100×100 block size binary image with two brightness levels which are easily distinguishable in the histogram shown in Figure 4.12(c). The binary image was transferred onto the object beam by SLM. The CCD captured image is also shown in Figure 4.12(b). The corresponding histogram in Figure 4.12(d) shows a bimodal distribution of grey levels. Three dominant regions can be distinguished clearly: The *region 1* corresponds to low intensity pixels (logical 0s) in the image, while the *region 3* indicates high intensity pixels of logical 1s. The logical state of pixels belonging to *region 2* cannot be ascertained clearly due to its overlap with region 1 and region 3. In other words, unlike input binary image, the CCD image does not have unique intensity threshold to distinguish logical 0s and logical 1s.

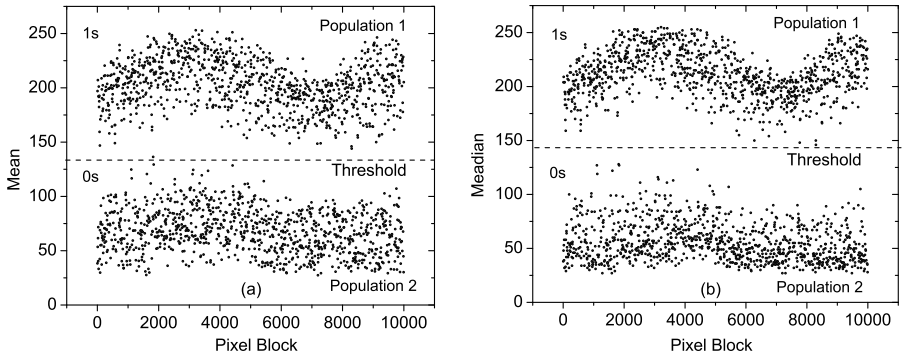

Figure 4.13: Block-wise (a) mean and (b) median distributions of the CCD captured SLM image.

Block-based Mean and Median Distribution

In order to reconstruct the original data, it is imperative to clearly distinguish the logical 1s and 0s from the CCD output of the binary image. As described above, a simple intensity based pixel thresholds technique is ineffective to achieve the desired goal. The block-based statistics apparently gives more reliable results. Each block (white/black) in the binary page such as shown in Figure 4.12 was imaged onto a group of, say, $m \times n$ CCD pixels. In the present case, it was 9×9 CCD pixels. The CCD image was block-processed. That is, the intensity *mean* and the *median* were calculated for each 9×9 pixel block of CCD image. The block-wise *mean* and the *median* distribution of the CCD image is shown in Figure 4.13(a)–(b), respectively. In both cases, two sets of population –belonging to logical 1s and logical 0s, are clearly distinguishable. All the blocks above (below) a mean/median

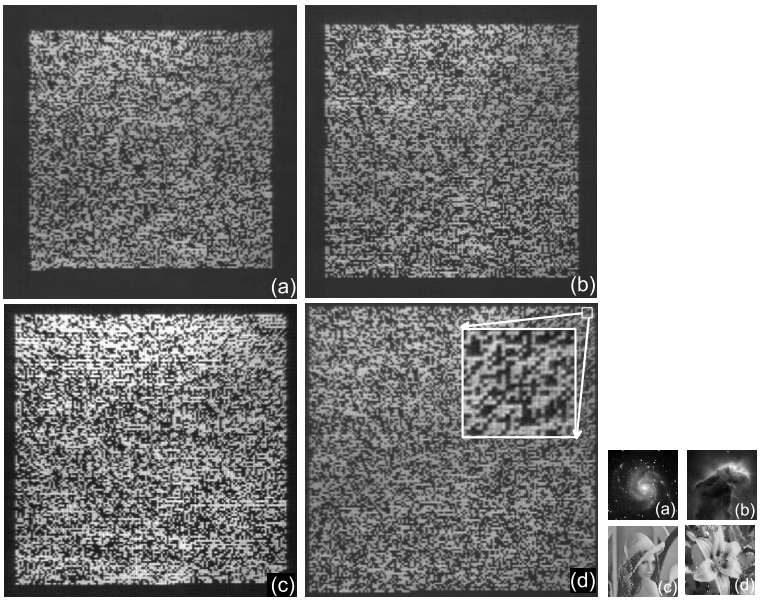

Figure 4.14: Retrieved binary pages of (a) M101 galaxy, (b) Eagle nebula, (c) Lena and (d) Lily. The reconstructed (64×64 pixel size) images after the binary decoding are shown in the right.

threshold belong to logical 1s (logical 0s). Since the two populations are widely separated, the selection of discrimination threshold can be made without any ambiguity.

Finally, the binary pages for the four test images were recorded holographically at different location in the crystal. All experimental conditions were identical to those described in section 4.3.1. The retrieved set of binary data pages is shown in Figure 4.14. The inset in Figure 4.14 (d) also gives a closer view of a small portion in the image. The original images (shown in the right) were recovered without loss after decoding the retrieved binary data. The main steps involved in reconstruction are as follow:

- ▷ The retrieved data pages were block-processed using a programming code written in *Mathematica* and Huffman encoded sequence of 1s and 0s was reconstructed.
- ▷ Using Huffman decoding algorithm, the binary sequence was re-mapped to obtain *up-shifted* Haar transformed data.
- ▷ $c_{\min}$ was subtracted from the up-shifted coefficients to unfold the negative Haar coefficients.
- ▷ Subsequently, inverse Haar transformation was applied to recover the original images.

4.3.3 Storage of Astronomical Images in Fe:Ce:Ti:$LiNbO_3$

A holographic data-base of 106 astronomical images was created in 18 spatial locations of the crystals. The multiplexing scheme has already been described in Figure 4.10. Each spatial location contains a stack of 6 image holograms recorded by rotating the crystal about an axis perpendicular to the plane of recording beams. The minimum angular separation between subsequent holograms was $\Delta\theta \approx 1^{\circ}$. Recording exposure time for each image was around 4-5 minutes. Later, the stored holograms were read-out using CCD camera and transferred into the computer hard disk. During the read and write operations, the laser input power was fixed at 0.5 W. Figure 4.15 shows every third and sixth raw image retrieved from each of the 18 hologram stacks. The original images were downloaded from different resources available on the internet. The corresponding details of images shown in Figure 4.15, are listed in Table 4.2.

A few noteworthy observations are:

- ▷ Due to uniform exposure time, the fainter images are recorded poorly as compared to brighter ones. The weakly recorded images are more likely to be erased during subsequent read/write operations. For example, image 9, 13, 18, 30 in Figure 4.15 were partly erased after a weeks time. This problem can be eliminated by selecting a *weighted exposure* time schedule that takes into account the energy content in the image. That is, at a given laser power, the exposure time will be inversely related to the image brightness.

- ▷ In many astronomical images the brightness level of different image features varies over a large range. That is, an image may contains several brighter as well as faint objects. The grating formation time of the crystal is a nonlinear function of input intensity. Therefore, when writing a hologram, a nonlinear response of the crystal may cause over saturation of the brighter objects in the image in a relatively short time, while the dim objects in the image are yet to be recorded. As a consequence, the brighter features in the retrieved image, appear bleached out or over-exposed (e.g., image 12, 25 and 27 in Figure 4.15). An appropriate gamma correction of the input image prior to recording would help curtailing the selective saturation.

- ▷ The quality of raw images retrieved from the crystal can be improved by various digital image processing means. For example, the interference pattern present in image 4, 10 and 28 of Figure 4.15 can be removed by band-pass filtering in Fourier

domain. Likewise, the pixel-to-pixel random noise can also be minimized using local averaging or Gaussian filtering of the image pixels in spatial domain.

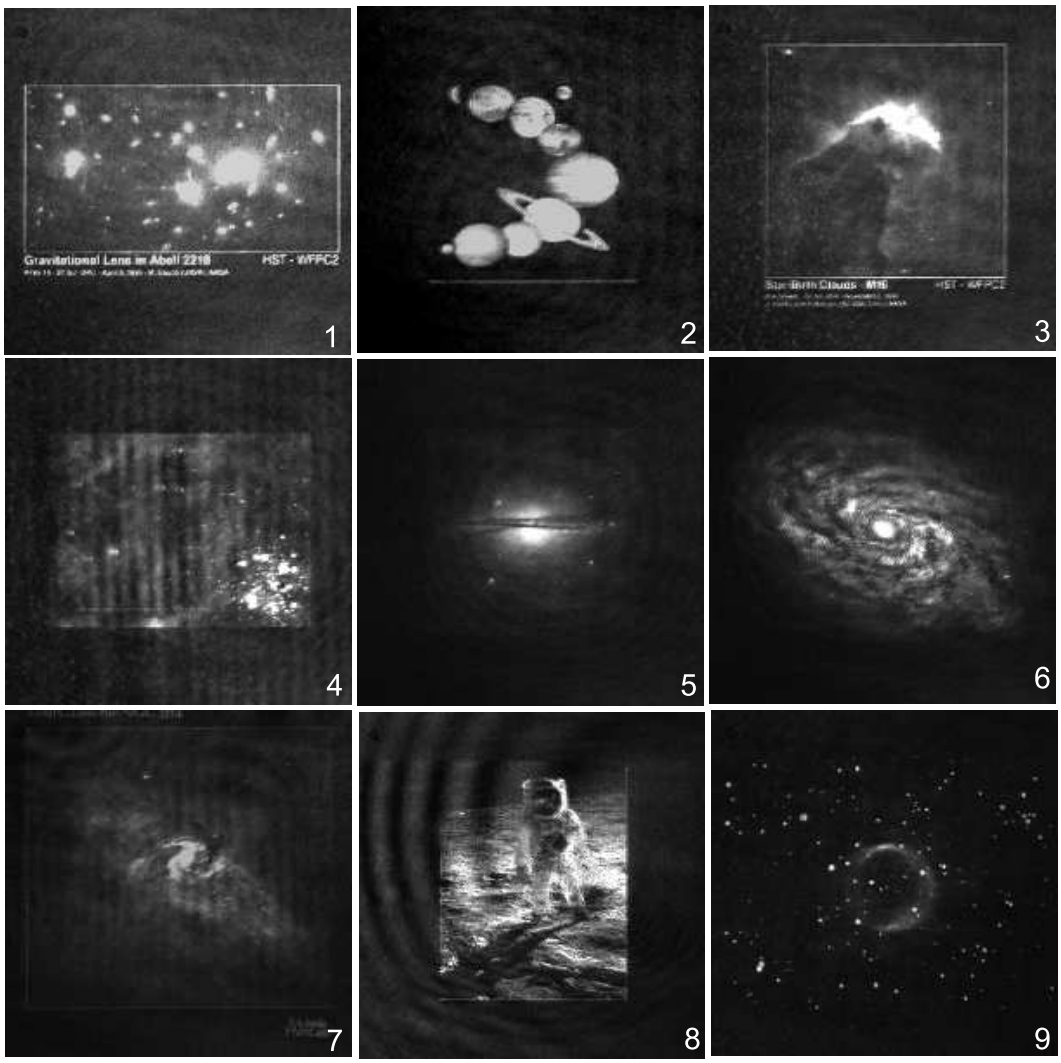

cont.

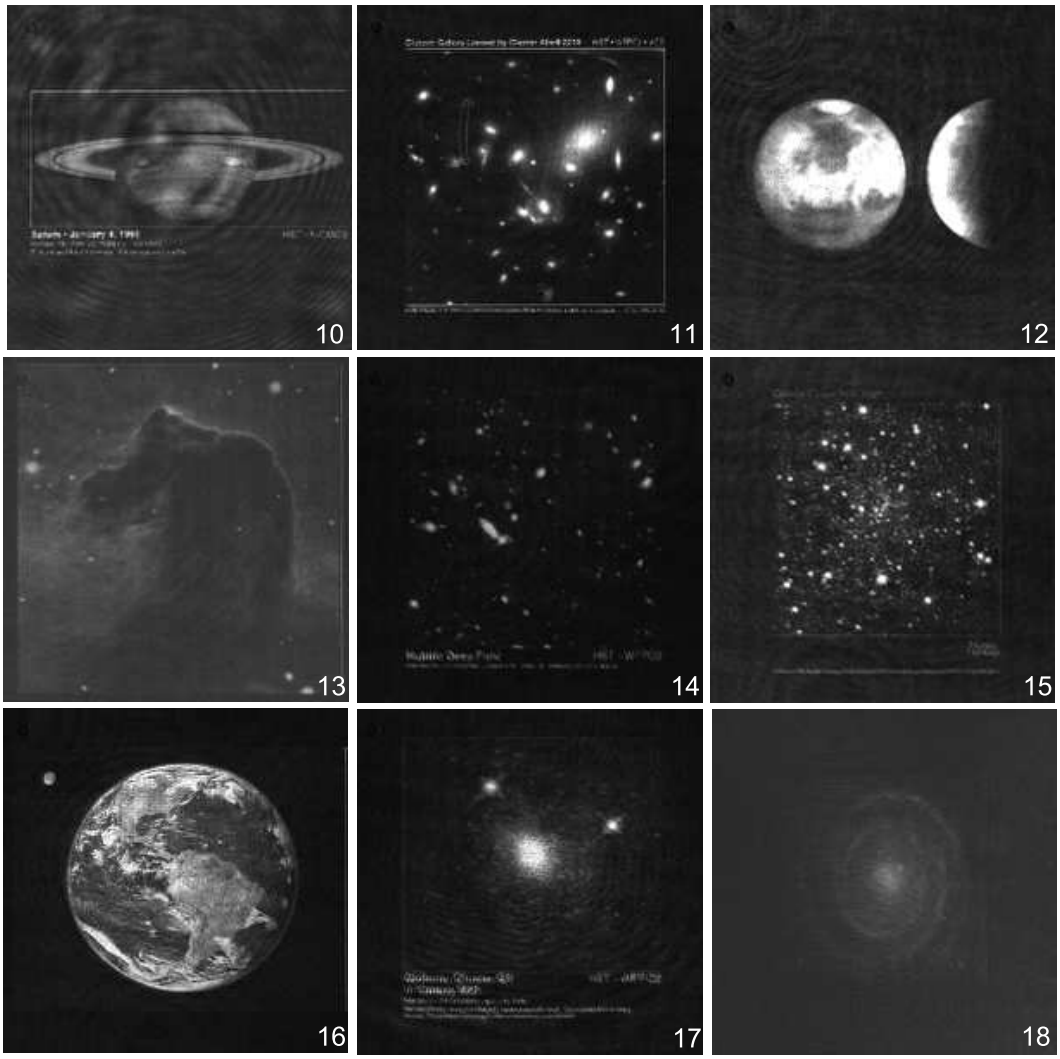

cont.

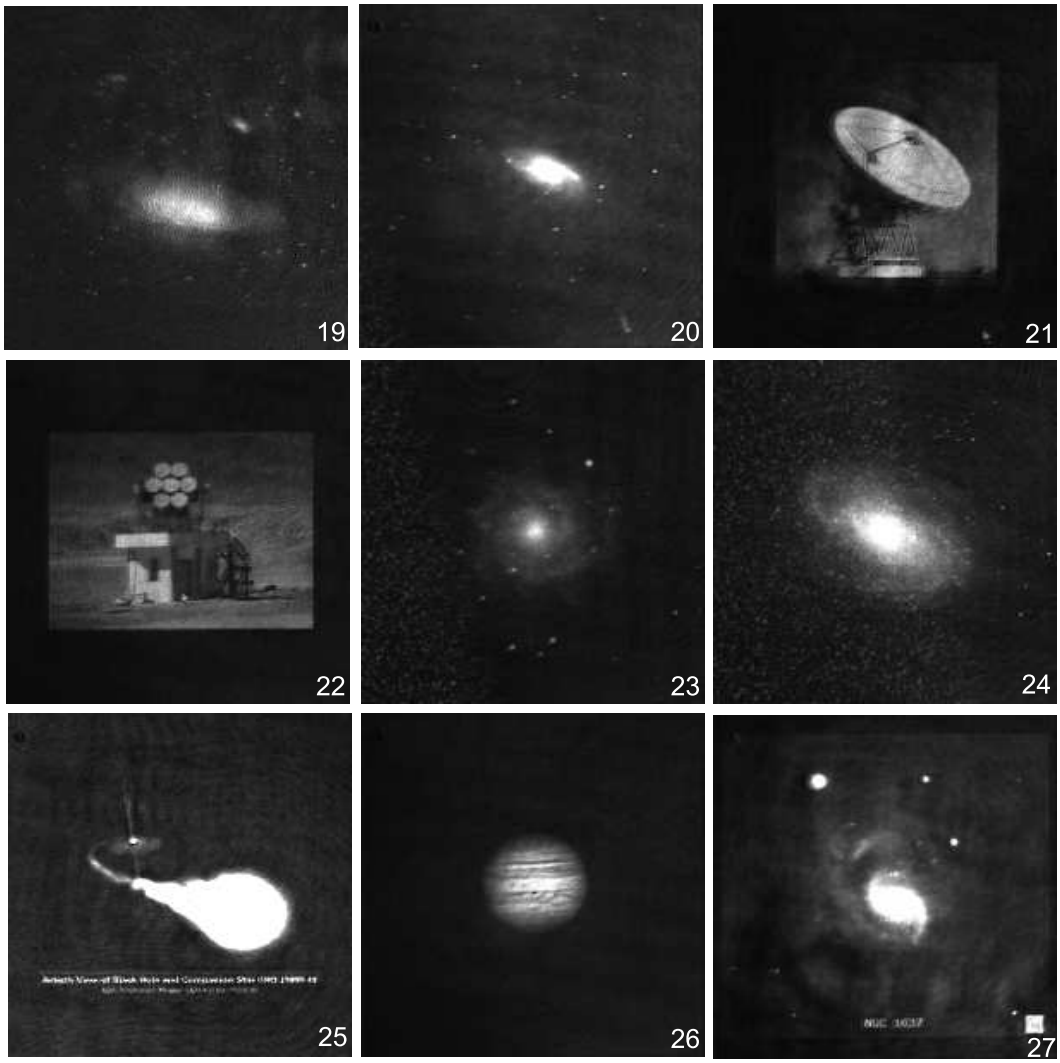

cont.

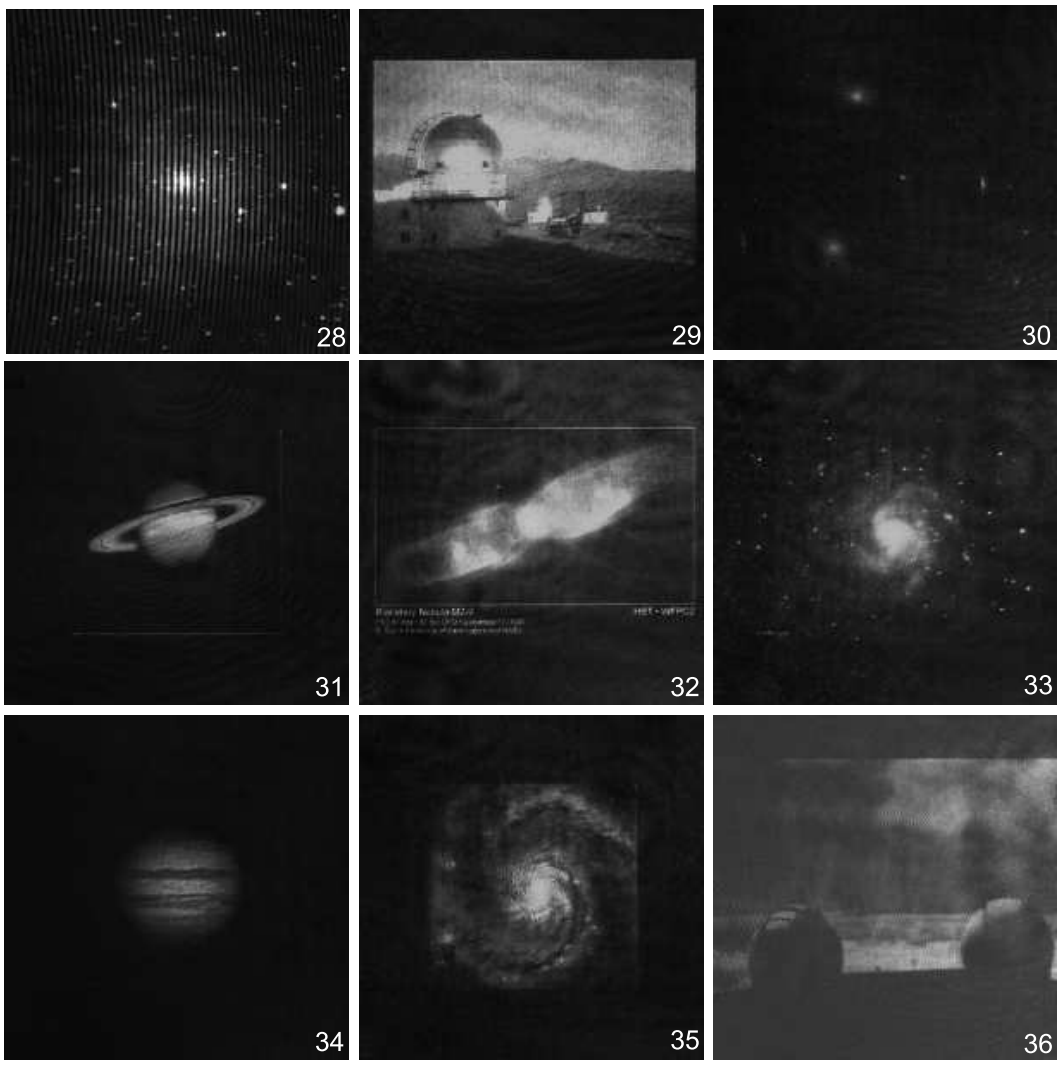

Figure 4.15: Holographically retrieved images from the crystal. The set comprises every third and sixth raw image read-out from all the 18 spatial locations of the crystal.

Table 4.2: Description of images shown in Figure 4.11.

S. No	Image description	Original size & Source
1	Gravitational lensing in galaxy cluster Abell 2218	400×250 $^{(a)}$
2	Artist's impression of planets' motion	350×431 $^{(b)}$
3	Eagle nebula	300×335 $^{(a)}$
4	Star formation regions in Tarantula nebula	500×375 $^{(b)}$
5	The Sombrero galaxy M104 NGC 4594	431×348 $^{(b)}$
6	Spiral galaxy NGC 4414	431×350 $^{(c)}$
7	Spiral galaxy pair NGC 3314	400×500 $^{(a)}$
8	Buzz Aldrin on the Moon	242×298 $^{(b)}$
9	Galaxy NGC 6781	407×528 $^{(c)}$
10	Saturn image	500×267 $^{(a)}$
11	Distance galaxy lensed by Abell 2218	610×655 $^{(a)}$
12	Earth-Mars photograph taken from space	350×250 $^{(b)}$
13	Horse head nebula	400×446 $^{(a)}$
14	Hubble deep field	400×446 $^{(a)}$
15	Globular cluster NGC 3697	300×375 $^{(a)}$
16	Earth from the outer space	431×348 $^{(c)}$
17	Globular cluster in galaxy M31	400×446 $^{(a)}$
18	Backwards spiral Galaxy NCG 4622	431×350 $^{(c)}$
19	Spiral galaxy NGC 7331	734×587 $^{(c)}$
20	Galaxy M106	660×547 $^{(c)}$
21	Kashima radio antenna	540×420 $^{(-)}$
22	High energy gamma ray telescope at IAO*	640×480 $^{(d)}$
23	Galaxy M71	458×366 $^{(b)}$
24	Galaxy M81	998×713 $^{(c)}$
25	Artist's conception of black hole & a companion star	350×280 $^{(a)}$
26	Jupiter comet impact	300×200 $^{(a)}$
27	Galaxy NGC 1637	404×378 $^{(d)}$
28	Galaxy NGC 6946	721×611 $^{(c)}$
29	Himalayan Chandra telescope at IAO	400×300 $^{(d)}$
30	Galaxy M86	760×510 $^{(c)}$
31	Saturn image	256×256 $^{(-)}$
32	Planetary nebula M2-9	400×262 $^{(a)}$
33	Galaxy M101	750×542 $^{(a)}$
34	Jupiter from Cassini orbiter	431×348 $^{(b)}$
35	Whirlpool galaxy M51	431×350 $^{(b)}$
36	Keck telescope located in Mauna Kea in Hawaii	518×318 $^{(b)}$

$^{(a)}$ `http://hubblesite.org/`

$^{(b)}$ `http://www.astroimages.net/`

$^{(c)}$ `http://www.gralak.com/Astro/Astro.html/`

$^{(d)}$ `http://www.iiap.res.in/`

* IAO is Indian Astronomical Observatory located at Hanle (J&K).

4.4 Conclusion

In this chapter, a page oriented architecture of HDSS is outlined. The importance of ECC and modulation codes in data storage application is briefly emphasized. In order to counter the increased overhead rate due to ECC and modulation codes and to improve the effective storage capacity, the need for image or data compression is highlighted. Three types of redundancies used in data compression are discussed. Image compression using the Haar wavelet transform is explained and the its implementation using matrix algebra is proposed. To remove the coding redundancy from the data, the variable length lossless encoding was described. Huffman's encoding technique was outlined with an example. Some of the important parameters such as the degree of compression, the root-mean-square error and the average code length were computed for the four test images.

Experimental aspect of holographic data storage and retrieval system in the lab, were explained in detail. A spatial and rotation multiplexing scheme was developed to store multiple image holograms in the photorefractive crystal. The storage and retrieval of compressed binary data page was successfully implemented. A block-based mean and median processing of CCD image was proposed to distinguish logical 1s and 0s. The compressed binary data pages corresponding to four test images were holographically written in Fe:Ce:Ti $LiNbO_3$. The stored data was retrieve and decoded to reconstruct the original images. At the preliminary stage, holographic recording and retrieval of as many as 108 grey scale astronomical images was successfully demonstrated. Finally, based on the qualitative observations of the retrieved images few suggestions were made to improve the image quality.

Chapter 5

Bacteriorhodopsin: Theoretical Modelling and Experiments

5.1 Introduction

Bacteriorhodopsin (bR) is a photochemically active protein found in the purple membrane of the bacteria Halobacterium salinarium, which is also known as Halobacterium halobium. The photo-response and structure of bR has already been discussed in Chapter 1. The work presented in this chapter comprises theoretical modelling and experimental studies of commercially available bR films. In first section, a time-dependent theoretical model based on rate equations for all the photochemical states of bacteriorhodopsin (bR) is developed. The rate equations for proposed model are formulated and outline of the solution is provided. Subsequently, results obtained from theoretical calculations and computer simulations are discussed. In section 5.2, the experimental work on nonlinear absorption based, high contrast, all-optical switching in photochromic bR films is presented. A simplified three–state model for bR photocycle is formulated and the expression for nonlinear absorption coefficient under two–beam illumination is derived. The switching action is accomplished by controlling the transmission of a weak probe beam through bR sample with the help of a strong pump beam illumination at 532 nm. The results are presented for the wild–type as well as genetically modified D96N variant of the bR.

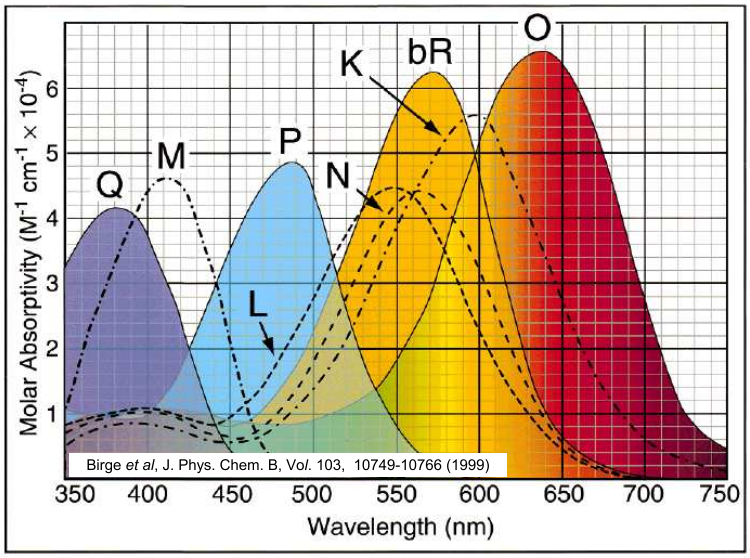

Figure 5.1: Absorption spectra of a typical wild-type bR molecules.

5.2 Theoretical Model and Simulations

Absorption of a photon at $\sim$568 nm by bR molecule initiates a photocycle that leads to transport of a proton out of the cell. The photocycle is characterized by a series of distinct spectral intermediates as explained in Chapter 1. It is customary to represent the photocycle as: $B_{570} \rightarrow J_{625} \rightleftharpoons K_{610} \rightleftharpoons L_{550} \rightleftharpoons M_{410} \rightleftharpoons N_{560} \rightleftharpoons O_{640} \rightarrow B_{570}$. Here, the letters denote the ground and intermediate states and the subscripts correspond to the peak wavelength (nm) of their respective absorption bands. A considerable overlap, as shown in Figure 5.1, exists between the absorption bands of different intermediates [83]. Almost all the applications involving bR require to alter the population density of its molecules in one state or other via photoexcitation. On account of population redistribution of molecules on excitation, bR exhibits strong optical nonlinearities at very low laser powers.

A photocycle for commonly used wild-type bR is shown in Figure 5.2. Typical thermal relaxation times and absorption maxima are also indicated. Also shown in Figure 5.2 are branched states P and Q usually not considered as a part of photocycle, but they are crucial for volume-holographic and page-oriented optical memory applications [82, 83]. Some intermediate state like M has two substates M_I and M_{II}, which are spectroscopically indistinguishable. Substates of O has also been identified in some of the recent studies on bR mutants [191, 192].

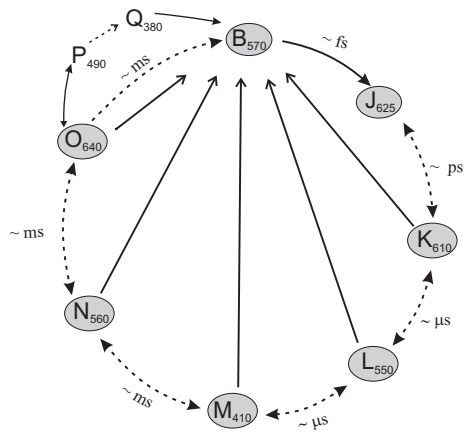

Figure 5.2: Schematic representation of the photocycle of wildtype bR molecule. Arrows with dashes and solid lines indicate thermal and photoinduced transitions, respectively.

5.2.1 A Time-dependent Multi-state Model

Overall dynamics of the each state is usually quite complex and it is governed by incident light intensity and various photophysical properties of other intermediates. The intricate nature of the photocycle makes the mathematical modelling and analysis rather complicated. In the past, researchers have used much simplified scheme of two-level model to describe the kinetics of bR photocycle [115, 193, 194]. The two-level model usually considers B and M states and neglects the time scales and contribution of other intermediates. In general, a significant variation from this model may result at very high or low light irradiance. Another model proposed by Reddy [195] and Roy *et al.* [196] takes into account all the bR states. But, their model is applicable only for steady-state condition, and does not include the time–dependence of the population densities of the intermediate states.

It is not possible to exactly solve the rate equations by simultaneously retaining the temporal and intensity dependence. Therefore, an indirect approach was adapted by conjecturing an effective rate constant that represents average thermal decay and reverse phototransitions rate from various intermediates to B state when illuminated with green–yellow light. A semiquantitative study of temporal and intensity dependence of the population densities can easily be made from the solution obtained under such approximation.

The well known wild-type bR molecular photocycle, shown already in Figure 5.2, can be adopted without any loss in generality. The B state is thermally stable for all form of molecules and requires photoexcitation by suitable wavelength to initiate the photocycle. However, any other intermediate can have bidirectional thermal transitions only with its

adjacent states or it can absorb a photon and revert back to B. The rate of forward reaction is usually dominant at the initial stages before reaching a steady-state, therefore, it is suffice to consider the forward thermal transitions alone to keep the analysis simple. The rate equations for each state can be written as [197]:

$$\frac{\mathrm{d}N_\mathrm{p}}{\mathrm{d}t} = K_\mathrm{o}\,N_\mathrm{o} - \left(K_\mathrm{p} + \frac{1}{\tau_\mathrm{p}}\right) N_\mathrm{p}, \tag{5.1}$$

$$\frac{\mathrm{d}N_\mathrm{o}}{\mathrm{d}t} = \frac{N_\mathrm{N}}{\tau_\mathrm{N}} - \left(K_\mathrm{o} + \frac{1}{\tau_\mathrm{o}}\right) N_\mathrm{o}, \tag{5.2}$$

$$\frac{\mathrm{d}N_\mathrm{N}}{\mathrm{d}t} = \frac{N_\mathrm{M}}{\tau_\mathrm{M}} - \left(K_\mathrm{N} + \frac{1}{\tau_\mathrm{N}}\right) N_\mathrm{N}, \tag{5.3}$$

$$\frac{\mathrm{d}N_\mathrm{M}}{\mathrm{d}t} = \frac{N_\mathrm{L}}{\tau_\mathrm{L}} - \left(K_\mathrm{M} + \frac{1}{\tau_\mathrm{M}}\right) N_\mathrm{M}, \tag{5.4}$$

$$\frac{\mathrm{d}N_\mathrm{L}}{\mathrm{d}t} = \frac{N_\mathrm{K}}{\tau_\mathrm{K}} - \left(K_\mathrm{L} + \frac{1}{\tau_\mathrm{L}}\right) N_\mathrm{L}, \tag{5.5}$$

$$\frac{\mathrm{d}N_\mathrm{K}}{\mathrm{d}t} = K_\mathrm{B}\,N_\mathrm{B} - \left(K_\mathrm{K} + \frac{1}{\tau_\mathrm{K}}\right) N_\mathrm{K}, \tag{5.6}$$

$$\begin{aligned}\frac{\mathrm{d}N_\mathrm{B}}{\mathrm{d}t} &= -K_\mathrm{B}\,N_\mathrm{B} + K_\mathrm{K}\,N_\mathrm{K} + K_\mathrm{L}\,N_\mathrm{L} + K_\mathrm{M}\,N_\mathrm{M} + K_\mathrm{N}\,N_\mathrm{N} \\ &+ \left(\frac{1}{\tau_\mathrm{o}} + K_\mathrm{o}\right) N_\mathrm{o} + \left(\frac{1}{\tau_\mathrm{p}} + K_\mathrm{p}\right) N_\mathrm{p}\end{aligned} \tag{5.7}$$

where, N_i is the population density of the molecules and τ_i^{-1}, is the thermal time constant. The photochemical rate $K_i = \sigma_i F_i$, where σ_i is absorption cross-section and F_i is photon flux. Index i designates B, K, L, M, N, O, and P state. The J state has been neglected since it is extremely short lived ($<$ ps) and remains untrapped even down to 4° K [83]. Further, P and Q states are considered as equivalent and designated as P. Thermal decay rates depend on parameters such as the ambient temperature, hydration, and pH level of the film and otherwise remain constant [198,199]. The closed form solution for the coupled differential Eqs. (5.1)–(5.7) is not possible unless time dependence is neglected. To circumvent this difficulty, we closely examine the two counteracting mechanisms that affect the B state population in Eq. (5.7). (*a*) The photoexcitation of B state diminishes its population when illuminated with green–yellow light beam, and (*b*) the photoinduced transitions from all other intermediates along with thermal relaxation at the end of the photocycle tends to replenish it. In second process (*b*), the thermal decay and photoinduced transition rates of all the intermediates that populate B state can be approximated by an effective rate constant κ. Therefore, Eq. (5.7) can be rewritten as,

$$\frac{\mathrm{d}N_\mathrm{B}}{\mathrm{d}t} = -K_\mathrm{B}\,N_\mathrm{B} + \kappa\,N_\mathrm{I} \tag{5.8}$$

where N_{I} is population of all the intermediate states. If N_{T} is total number density of the bR molecules, then the relation $N_{\mathrm{T}} = N_{\mathrm{B}}(t) + N_{\mathrm{I}}(t)$ is valid at any given time. Considering the initial condition, i.e. $N_{\mathrm{B}} = N_{\mathrm{T}}$ at $t = 0$, Eq. (5.8) can be solved to give:

$$N_{\mathrm{B}}(t) = \frac{\left(\kappa + K_{\mathrm{B}}\, \mathrm{e}^{-t\,(\kappa + K_{\mathrm{B}})}\right)\, N_{\mathrm{T}}}{\kappa + K_{\mathrm{B}}} \tag{5.9}$$

We note that the rate equation for each intermediate is only coupled to its previous state population. Therefore, solution for K state can easily be found by substituting Eq. (5.9) into Eq. (5.6) with initial condition $N_{\mathrm{K}} = 0$ and $t = 0$ as,

$$\begin{aligned} N_{\mathrm{K}}(t) = K_{\mathrm{B}}\, N_{\mathrm{T}}\, \tau_{\mathrm{K}}\, \mathrm{e}^{-t\left(\kappa + K_{\mathrm{B}} + K_{\mathrm{K}} + \tau_{\mathrm{K}}^{-1}\right)} \Big\{ &- \left[\mathrm{e}^{t\,(\kappa + K_{\mathrm{B}})}\, (\kappa + K_{\mathrm{B}})\, (-1 + (\kappa - K_{\mathrm{K}})\, \tau_{\mathrm{K}})\right] \\ &+ \mathrm{e}^{t\left(K_{\mathrm{K}} + \tau_{\mathrm{K}}^{-1}\right)} \left[\mathrm{e}^{t\,(\kappa + K_{\mathrm{B}})}\, \kappa\, (-1 + (\kappa + K_{\mathrm{B}} - K_{\mathrm{K}})\, \tau_{\mathrm{K}}) - K_{\mathrm{B}}\, (1 + K_{\mathrm{K}}\, \tau_{\mathrm{K}})\right] \Big\} \\ &\times \left\{(\kappa + K_{\mathrm{B}})\, [-1 + (\kappa + K_{\mathrm{B}} - K_{\mathrm{K}})\, \tau_{\mathrm{K}}]\, (1 + K_{\mathrm{K}}\, \tau_{\mathrm{K}})\right\}^{-1} \end{aligned} \tag{5.10}$$

Following the recursive substitution into subsequent rate equations, the solution for all other intermediate states can be found. Here, writing the lengthy expressions for other intermediates is avoided for convenience.

The expressions for steady-state population densities for any of the intermediate state in photocycle i can be obtained from the corresponding general solution in the limit $t \to \infty$. After the substitution and algebraic simplification, we get,

$$N_i^{\mathrm{s}} = \frac{\kappa\, K_{\mathrm{B}} N_{\mathrm{T}}\, \tau_j}{(\kappa + K_{\mathrm{B}}) \prod_{j=1}^{i} (1 + K_j \tau_j)} \tag{5.11}$$

where $j = 1, 2, 3, ...$, represent K, L, M, ..., respectively, and superscript 's' stands for the steady-state. Other symbols have their usual meaning as already defined. It is customary to express the photoinduced transition rates in terms of the molar extinction coefficients $\epsilon_i(\lambda)$ as [200]:

$$K_i = \frac{2303\, \phi_i(\lambda)\, \epsilon_i(\lambda)}{N_{\mathrm{A}}\, h\, \nu}\, I \tag{5.12}$$

where ϕ_i, I, N_{A}, h, and ν are, quantum efficiency, light intensity in mW, Avogadro's number, Planck's constant, and central frequency of illuminating light, respectively. Due to the presence of thermal decay term in Eq. (5.7), the effective rate constant κ defined earlier should exhibit a sublinear intensity dependence of the form $\kappa\, \alpha\, I^{\gamma}$. The value of $\gamma \sim 0.7$ is consistent with our simulations for the material parameters listed in Table 5.1 [82, 196].

Table 5.1: Typical material parameter values for wild–type bR.

	$\epsilon_i\,(\mathrm{l\,mol^{-1}cm^{-1}})$			
States	410 nm	570 nm	640 nm	τ_i
B	10000	63000	7842	–
K	8000	47000	36600	$10\,\mu$s
L	11000	39000	7000	$50\,\mu$s
M	46000	0	0	1 ms
N	10000	42000	9000	3 ms
O	11000	28000	66000	5 ms
P	12000	1000	0	$\sim$ mins
Q	31000	0	0	$>$ 5 yrs

5.2.2 Simulations and Discussion

The dynamics of various states based on the solution of the proposed model is shown in Figure 5.3. Ground state excitation of a thin bR film at 570 nm is assumed for simulation purpose. For clarity, the P state population is not shown since it is very small ($\sim 0.003\,\%$) due to extremely low quantum yield ($\phi_{\mathrm{o}\rightarrow\mathrm{p}} \sim 2 \times 10^{-4}$) for branched cycle in comparison to primary photoreaction of bR ($\phi_{\mathrm{B}\rightarrow\mathrm{K}} \geq 0.64$) [82]. Table 1 lists the values of other material parameters used in our simulations [83]. Theoretical calculations indicate that at low intensity ($I \leq 1\,\mathrm{Wcm^{-2}}$) the population of each state depends critically on its thermal relaxation time, whereas at higher intensity it is determined by the photoinduced transitions of the intermediate in question. This can be seen in Figure 5.3(a)–(d), where, for example, the relative population of O state is higher at low intensity (due to relatively longer thermal decay time) compared to other states but does not increase in same proportion at higher intensity. In fact there is a decline at higher intensity due to increase in absorption that causes significant photoinduced transitions from O to B. On the contrary, M state has no absorption at 570 nm, and therefore its population continues to rise with intensity. As expected, the maxima of each intermediate state, in order of their occurrence in photocycle is also shown suitably shifted to right on the time axes, widely spaced from each other at low intensity, and considerably shifted to left at higher intensity.

The knowledge of optimum light exposure is of paramount importance in any application. This can be elucidated by considering page oriented volumetric memories that rely on branched photocycle of bR involving P and Q states. The process is based on the following consecutive sequence:

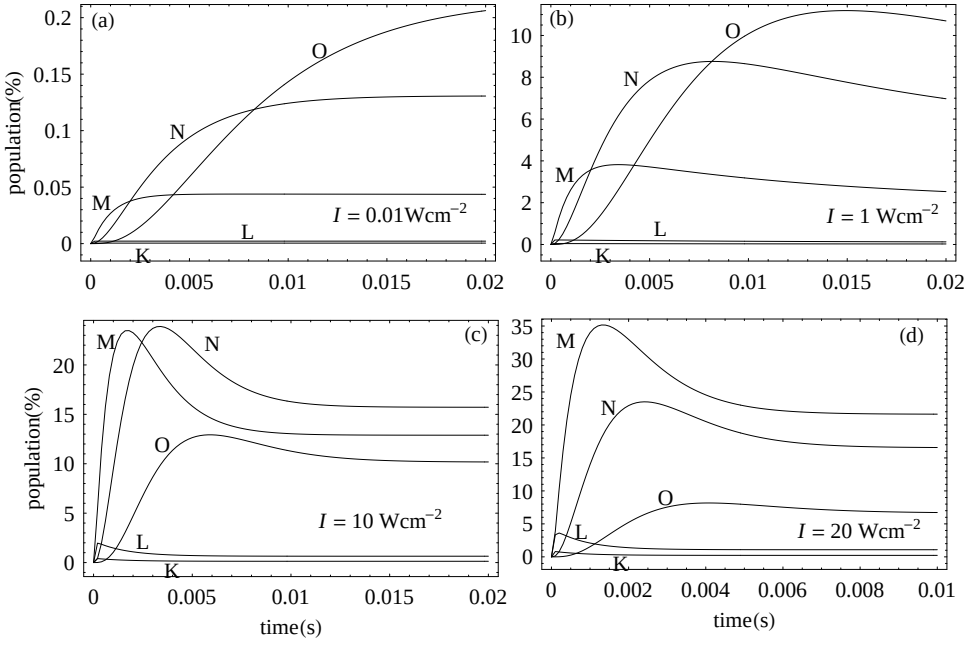

Figure 5.3: Temporal evolution of population densities of various intermediates at different intensities of illumination at wavelength 570 nm.

$$\mathrm{B}(\texttt{state 0}) \overset{\text{photon 1}}{\Longrightarrow} \mathrm{K} \rightarrow \mathrm{L} \rightarrow \mathrm{M} \rightarrow \mathrm{N} \rightarrow \mathrm{O} \rightarrow \mathrm{B} \qquad (\textit{paging})$$

$$\mathrm{O} \overset{\text{photon 2}}{\Longrightarrow} \mathrm{P/Q}(\texttt{state 1}) \qquad (\textit{writing})$$

where P and Q are intermediates in the branching cycle and K, L, M, N and O are all intermediates within the main photocycle. In the *paging* process, a green–yellow laser beam ($\lambda \approx 570\,\mathrm{nm}$) activates a thin region inside the bR cuvette by initiating the photocycle. After few milliseconds the population of O intermediate reaches near maximum. In the present case it takes $\sim$ 15 ms at 1 Wcm^{-2} paging beam intensity. At this point, spatially modulated data beam ($\lambda \approx 640\,\mathrm{nm}$) irradiates the volume to complete the *writing* process by photo-activating O state to P state that eventually decays to form a long lived Q state. Usually, a binary state 0 is assigned to B and 1 is assigned to P/Q state. A similar procedure is followed to read the stored data page using the technique of differential absorption measurements. To keep the bit error rate within acceptable limit ($\sim 10^{-12}$), a high signal to noise ratio (SNR) is most desirable while reading the data. Therefore, the first important thing is to develop an accurate *paging* scheme in terms of optimum exposure time and intensity to maximize the photo conversion from B to P/Q state. As

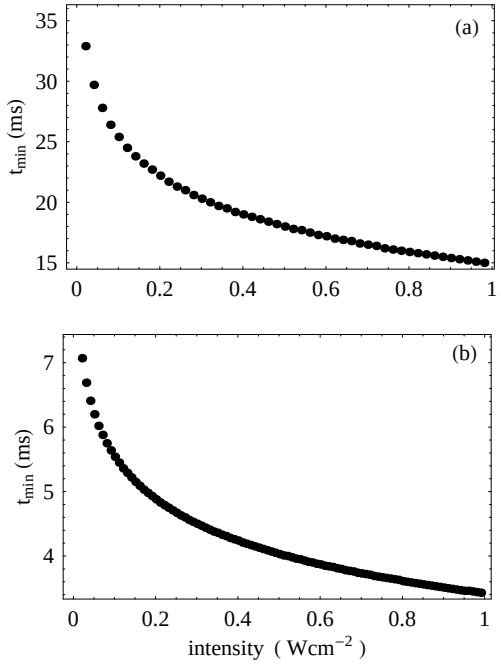

Figure 5.4: Plot of minimum time required vs illumination intensity to achieve maximum population densities (a) for O state (b) for M state.

noted already in Figure 5.3, the time taken to reach the maximum population for any intermediate decreases with intensity. The minimum exposure time $t_{\min}$ required to maximize O state population was found to vary from $\sim$ 35 ms at 0.001 Wcm^{-2} to 15 ms at 1 Wcm^{-2} intensity. Numerically computed $t_{\min}$ for O state is shown in Figure 5.4(a). A similar variation in $t_{\min}$ from 7 ms to 3.5 ms over the same intensity range can be noticed in Figure 5.4(b) for the M state. Plots for the steady-state population densities based on equation Eq. 5.11 are presented in Figure 5.5. Even in the steady-state, the overall behaviour is governed by the photoinduced transitions and the thermal decay rates. The steady-state photoconversion efficiency of bR to various intermediate states is different in different intensity regions. The O, N and M state populations in Figure 5.5 dominate region I, II and III, respectively. This fact can be used as an effective guideline for estimating *photon budget* while devising specific application based on any of the intermediates of the bR. For example, increasing the illumination intensity beyond 4.8 Wcm^{-2} will only reduce the O state yield. Therefore, it is advantageous to confine the illumination intensity within optimum limit of 4.8 Wcm^{-2} to maximally exploit O state in the intended application. On the other hand, high intensity that can be obtained from pulsed lasers or

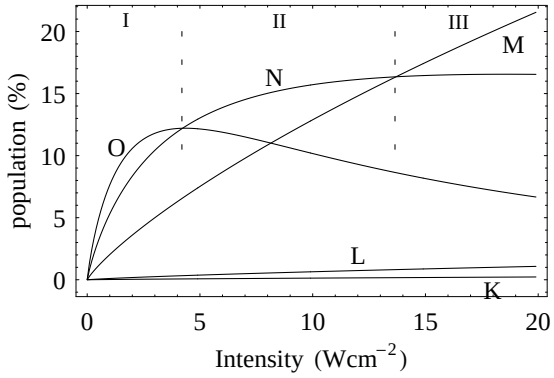

Figure 5.5: Steady-state population density versus intensity of illumination at wavelength 570 nm.

tightly focused cw beam is favourable for applications involving M state population. The noted aspect was not obvious in the earlier models [195, 196] as they were confined only to low intensity regime. Finally, it must be emphasized that most of the photophysical properties (such as absorption, life time and quantum efficiency etc.) of the bR can be tailor made by chemical or genetic modifications to suit a particular application [201].

5.3 All-Optical Switching in bR Films

On account of population redistribution of molecules on excitation, bR sample exhibits strong optical nonlinearities at very low laser powers. The phenomenon of photoinduced absorption changes and Kerr type refractive index changes are the most relevant nonlinear processes that form the basis for almost all the envisaged applications of bR.

The photoinduced anisotropy and birefringence in bR has been explored for its applications in all–optical switching [202,203]. The bR film that is normally opaque to the weak probe beam (in green-yellow region) becomes transparent due to significant reduction in absorption when illuminated with an intense pump beam. The pump assisted fine controllability of the probe beam transmission makes it ideal for operating as an all–optical switch.

Nonlinear absorption based all-optical switching and logic gates in bR have been experimentally demonstrated by researchers recently [106, 204–206]. All these studies were carried out using probe beam wavelength that corresponds to peak absorption of the O and M intermediates in the bR photocycle. As compared to the ground state, the fraction of molecules present in these states under steady-state pump illumination remains consid-

erably smaller. Therefore, even though the O-state has maximum absorption at 640 nm, the achievable contrast at this wavelength is rather low. To evaluate and optimize the performance of bR for switching purpose, nonlinear absorption dynamics and its spectral and intensity dependence merit a detailed investigation, as a considerable departure may exist between theoretically predicted model and experimentally measured values.

5.3.1 Photoinduced Nonlinear Absorption

Nonlinear absorption refers to the change in transmittance of the material as a function of incident light intensity. When a bR sample is illuminated with green–yellow laser (570 nm), increasing number of molecules are transferred into other intermediate states. The net result is that the sample cannot absorb as many photons of incident light as it does at low intensity levels. The reduced difference in population of molecules in ground state and other intermediates causes the reduction in ground–state absorption.

When the absorption cross-section of the excited or intermediate state is less than that of the ground state, the transmittance of the system will increased at high intensity. This process leads to saturable absorption. On the other hand, a reverse saturable absorption results when the absorption cross-section of the intermediate state is more than the ground state and as a consequence the material becomes less transmissive at high intensities. Interestingly, by selecting appropriate probe wavelength, the bR offer the possibility to realize both the phenomenon when photoexcited from the ground state by green-yellow light beam. As compared to other intermediates, the M and O states have relatively longer thermal relaxation times and also larger absorption cross-section. More importantly the non-overlapping absorption bands of M and O states are blue and red shifted with respect to ground state absorption. Therefore, it is suffice for all practical purposes to replace the complex photocycle by a simplified three-level scheme shown in Figure 5.6. The level 1, 2 and 3 can be identified, respectively, with B, M and O states in bR photocycle.

Here, we derive an expression for the intensity dependent nonlinear absorption closely based on the a simplified photoexcitation process. Therefore, from Figure 5.6, the admissible routes in photocycle are [207]:

$$1 \rightarrow 1' \Rightarrow 2 \Rightarrow 3 \Rightarrow 1,$$
$$1 \rightarrow 1' \Rightarrow 2 \rightarrow 1, \text{ and}$$
$$1 \rightarrow 1' \Rightarrow 2 \Rightarrow 3 \rightarrow 1$$

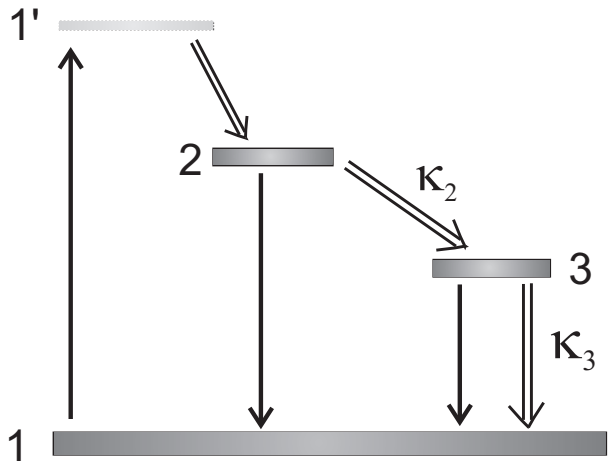

Figure 5.6: A modified three-level scheme for bR photocycle. The photoexcitation is designated by solid arrows (→), whereas, double arrows (⇒) indicate the process of thermal relaxation of intermediate states.

We consider the simultaneous illumination of the bR sample with a pump and a probe light beams which are not necessarily at same wavelength. The rate equations for the three states can be written as,

$$\frac{\mathrm{d}N_1}{\mathrm{d}t} = -(\sigma_{1s}\,F_s + \sigma_{1p}\,F_p)N_1 + (\sigma_{2s}\,F_s + \sigma_{2p}\,F_p)N_2 + (\sigma_{3s}\,F_s + \sigma_{3p}\,F_p + \kappa_3)N_3, \quad (5.13)$$

$$\frac{\mathrm{d}N_2}{\mathrm{d}t} = -\left(\sigma_{2s}\,F_s + \sigma_{2p}\,F_p + \kappa_2\right)N_2 + \left(\sigma_{1s}\,F_s + \sigma_{1p}\,F_p\right)N_1, \quad (5.14)$$

$$\frac{\mathrm{d}N_3}{\mathrm{d}t} = -\left(\sigma_{3s}\,F_s + \sigma_{3p}\,F_p + \kappa_3\right)N_3 + \kappa_2^{-1}N_2, \quad (5.15)$$

where N_i is molecule density, F_j is incident photon flux, σ_{ij} absorption cross-section for the state i ($i = 1, 2, 3$) and beam j ($j = s, p$ signifies probe and pump, respectively). κ_2 and κ_3 are thermal decay rates for $2 \Rightarrow 3$ and $3 \Rightarrow 1$ transition, respectively. The existence of $1'$ state is considered to be extremely short with insignificant population as compared to other states.

In the steady–state, $\mathrm{d}N_i/\mathrm{d}t = 0$ and Eqs. (5.13)–(5.15) can be solved to obtain the population density of the molecules in different levels. The change in probe beam intensity with propagation distance inside a bR film can be written as,

$$\frac{\mathrm{d}I_s}{\mathrm{d}z} = -\sum_i \sigma_{is} N_i \cdot I_s = -\alpha(I, \lambda) \cdot I_s \quad (5.16)$$

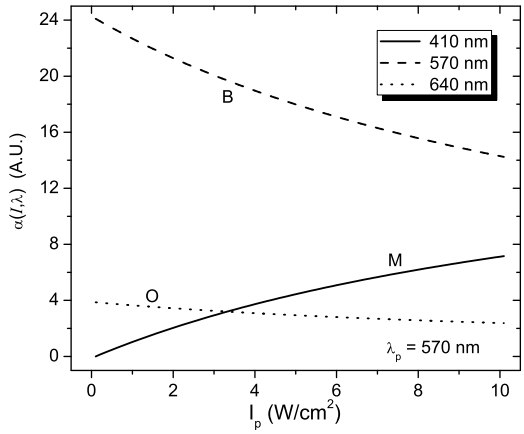

Figure 5.7: Calculated nonlinear absorption curves for 570 nm, 410 nm and 640 nm signal beams corresponding to absorption maxima of B, M and P states for a wild-type bR film.

where $\alpha(I,\lambda)$ is intensity–dependent absorption coefficient and it is given by,

$$\alpha(I,\lambda) = N_T \frac{a\sigma_{1p}\sigma_{2s}\kappa_2^{-1}F_p+(\sigma_{1p}F_p+\sigma_{1s}F_s)\sigma_{3s}\kappa_3^{-1}+a[1+(\sigma_{2p}F_p+2\sigma_{2s}\kappa_2^{-1}F_s)]\sigma_{1s}}{1+a[(\sigma_{1p}+\sigma_{2p})F_p+(\sigma_{1s}+\sigma_{2s})F_s]\kappa_2^{-1}+[(\sigma_{1p}+\sigma_{3p})F_p+(\sigma_{1s}+\sigma_{3s})F_s]\kappa_3^{-1}} \tag{5.17}$$

where $N_T = N_1 + N_2 + N_3$ is total density of the bR molecules, and $a = 1+(F_p\sigma_{3p}+F_s\sigma_{3s})\kappa_3^{-1}$. For a single beam illumination, i.e., $F_p = 0$, Eq. (1.17) reduces to the expression derived by Rao *et al* [208]. Considering the ground state excitation of bR at 570 nm, we can calculate the variations in nonlinear absorption coefficient using Eq. (1.17). The characteristic absorption saturation for B and O state and reverse absorption saturation for M state can be ascertained clearly from Figure 5.7. Simulated curves in Figure 5.7 are obtained using material parameters of a typical bR sample given in Table 5.1. It is to be noted that the intensity–dependent absorption change is maximum for a probe wavelength that is closer to ground state absorption. The experimental results presented in the next subsection indeed validate this assertion.

Switching time and contrast ratio

Two important parameters used for evaluating the performance of a simple on–off optical switch are: switching contrast also known as contrast ratio (C.R.) and switching time (S.T.) Switching contrast is the ratio of the maximum transmitted intensity $I_{\max}$ to the

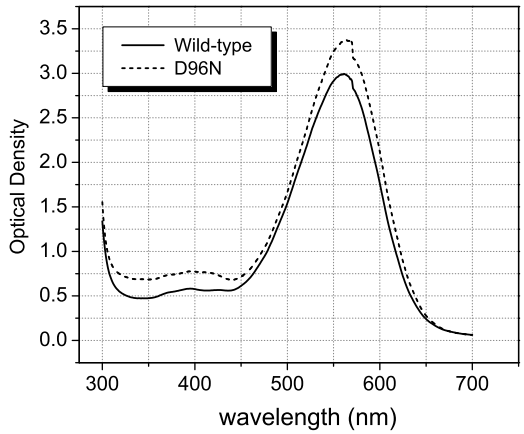

Figure 5.8: Spectral curves for ground state absorption in wild-type and D96N film.

minimum transmitted intensity $I_{\min}$, and often expressed in decibels as [209]:

$$\text{C. R.} = 10 \log(I_{\max}/I_{\min}) \tag{5.18}$$

A high contrast is necessary to distinguish two logic states unambiguously.

Switching time is the measure of finite elapse that occurs during the transition from one state of the switch to other. It is customary to define switching time as the time required to change the signal beam intensity from 10% to 90% of $I_{\max}$, i.e., S. T. $= t_{(0.9\, I_{\max})} - t_{(0.1\ I_{\max})}$.

5.4 Experimental Results and Discussion

The conventional pump–probe method is used to investigate the optical switching properties of commercially available wild–type (WTN3) and genetically modified D96N variant of the bR. Bacteriorhodopsin films were purchased from Munich Innovative Biomaterials GmbH (MIB) Germany. These films were sealed between two windows of high-quality optical glass which was held permanently in a rugged metal holder. The films had clear circular aperture of 19 mm. The spectral curves for ground state absorption of these films are shown in Figure 5.8.

A vertically polarized light from diode-pumped Nd: YAG laser at 532 nm was used as pump beam. The output of green, orange and red He-Ne lasers, respectively, at 543 nm, 594 nm and 633 nm were used as probe wavelengths. Both the films had optical density 2.5 (Figure 5.8) at 532 nm. The basic experimental set-up is outlined in Figure 5.9. The beam-crossing angle was made small to ensure a complete and uniform overlap of the beams in

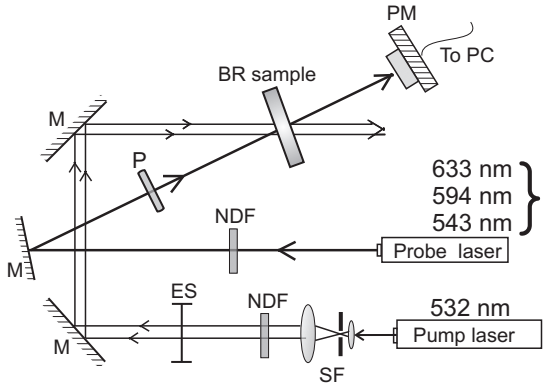

Figure 5.9: Experimental layout for optical switching using pump–probe method. SF, spatial filter with beam expander; P, polarizer; PM, power meter; M, mirror; ES, electronic shutter; NDF, neutral density filter.

the bR sample. Transmitted power of the probe was monitored using computer controlled optical power meter (Model: 4832-c Multichannel Optical Power Meter; Newport). In the region of interaction, the diameters of pump and probe beam was ~ 3.2 mm and ~ 2 mm, respectively.

5.4.1 Transmittance Measurements

The bR film that is considerably opaque at a weak probe beam becomes transparent when illuminated with brighter pump beam. The probe beam transmission in the presence of 5 mW pump beam is illustrated in Figure 5.10 for different probe wavelengths. There is no change in probe beam power for $t < 0$. Once the pump beam is turned on at $t = 0$, immediately the probe power starts rising and eventually reaches a steady–state value. The transmission again falls due to increased absorption after switching the pump beam off. The dynamics of transmission rise and decay processes can be described by a double exponential function of the form:

$$y = y_0 + A_1 \exp(-t/\tau_1) + A_2 \exp(-t/\tau_2), \tag{5.19}$$

where, y_0 is a positive constant, and $A_1, A_2 < 0$ for the transmission rise and $A_1, A_2 > 0$ for the transmission decay. τ_1 and τ_2 are two distinct time constants representing slower and faster components of rise and decay curves. These time constants are independent of pump intensity but found to vary with probe wavelengths. Both the films, WTN3 and D96N, had almost identical values of τ_1 and τ_2. For the rise and decay processes, the

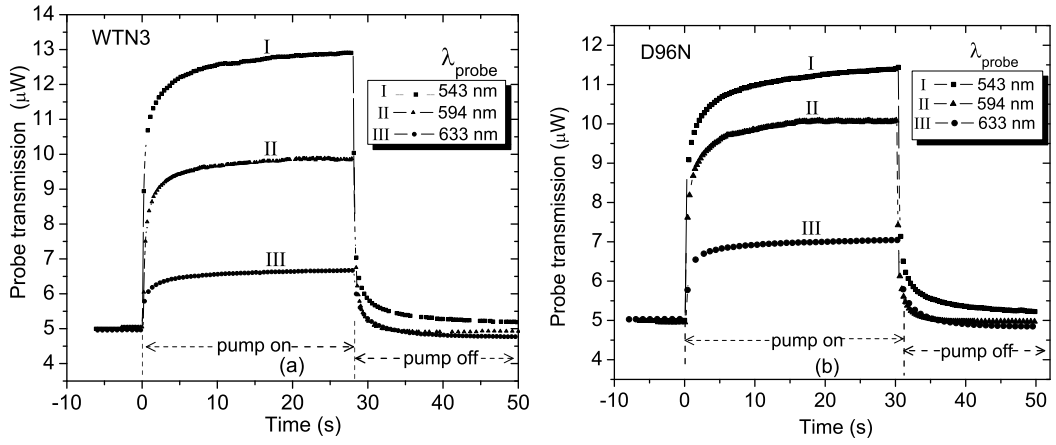

Figure 5.10: Pump–induced transparency of probe beam in (a) WTN3 and (b) in D96N film. The pump and probe powers are 5 mW and 5 μW, respectively.

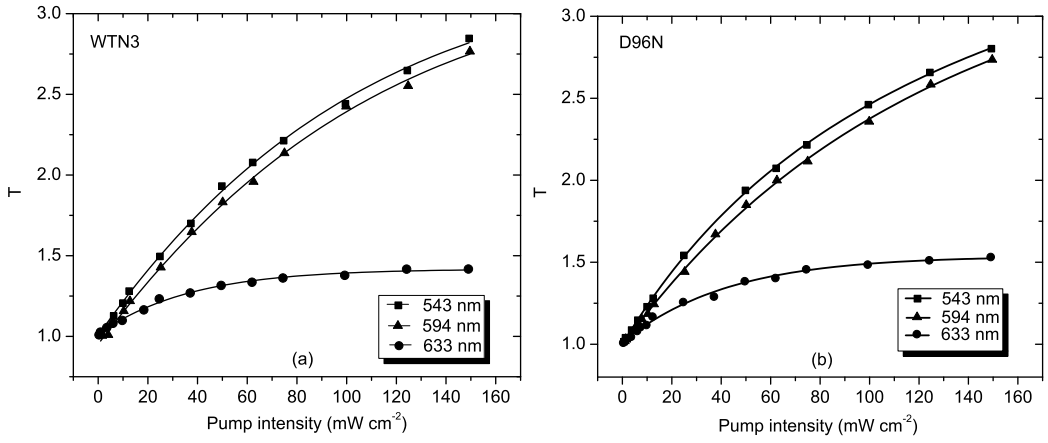

Figure 5.11: Measurement of probe beam transmittance through (a) wild-type and (b) D96N film at different pump powers. Different symbols represent the experimental data points, whereas solid lines are theoretically calculated values using three–state model.

approximate values of τ_1 and τ_2 obtained using Eq. (5.18), are listed in Table 5.2.

Table 5.2: The rise and decay time constants at different probe wavelengths for WTN3 and D96N bR samples.

λ_{probe}	rise		decay	
(nm)	$\tau_1(s)$	$\tau_2(s)$	$\tau_1(s)$	$\tau_2(s)$
633	9	0.6	4	0.5
594	3	0.3	1.5	0.2
543	7	0.3	4.5	0.2

The photo-induced change in optical transmittance of the probe beam was measured at different illumination levels of the pump beam by varying the power from 0.01 mW to 12 mW. The sample transmittance T is define as,

$$T = \frac{I_s(\text{pump on})}{I_s(\text{pump off})} \tag{5.20}$$

Where, I_s(pump on) and I_s(pump off) is the steady–state transmitted probe intensity in the presence and absence of the pump beam, respectively. The results for transmittance measurements for WTN3 and D96N film are shown in Figure 5.11.

The observed behaviour of sublinear dependence and subsequent saturation of probe beam transmittance at high pump intensities follows from the nonlinear absorption model presented in previous section. Unlike 633 nm, the probe wavelength 543 nm and 594 nm have relatively higher absorption primarily because they lie close to the ground state absorption peak (570 nm) of bR. Additionally, the molecules in other intermediates like K, L, N and O, due to their finite overlap of absorption bands, may contribute to increased probe absorption at these wavelengths [83]. The photo-conversion rate from other intermediate states to the B state increases with increase in pump irradiance. As a result the saturation of the 543 nm and 594 nm probe occurs relatively at higher pump intensity as compared to the early saturation of probe at 633 nm.

5.4.2 All-Optical Switching

The photonic switching operation was realized by controlling the transmission of probe beam through bR sample by periodically illuminating it by a pump beam at 532 nm [207]. The illumination period of the pump was controlled by an electronic shutter set to 50% duty cycle. The pump illumination period was varied over a range from 10 s to 100 ms.

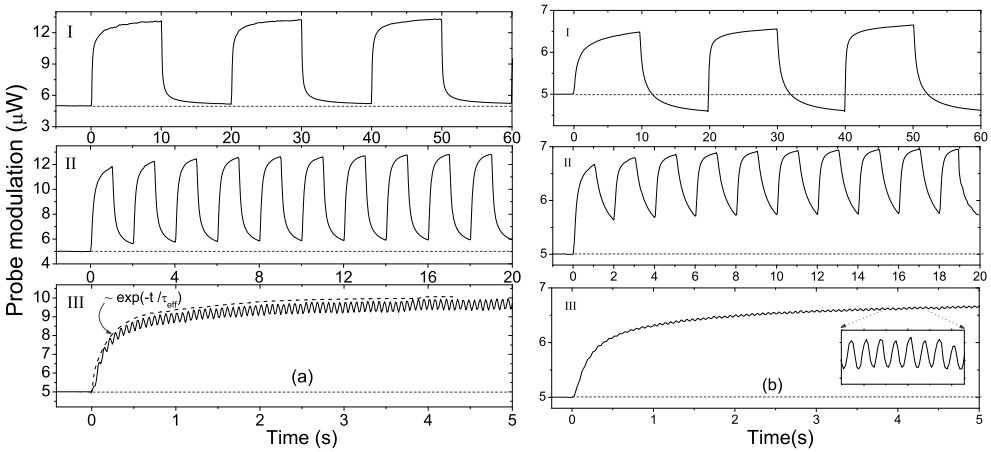

Figure 5.12: Probe beam switching at (a) 543 nm and (b) 633 nm in WTN3 film in response to periodic, square-wave illumination with 10 mW pump. Pump excitation rate for the curve I, II and III are 0.05 Hz, 0.5 Hz and 15 Hz, respectively.

The probe beam power through bR sample was fixed at 5 μW prior to pump excitation that begins at $t = 0$. In response to periodic square–wave pump excitation, the switching characteristics of the probe transmission resembles more like a charging and discharging of a capacitor.

Shown in Figure 5.12 are some of the experimental results of the optical switching observed at 543 nm and 633 nm probe wavelengths. At higher illumination rate the switching process approaches a steady response with a time constant τ_{eff}. This is indicated by a segmented line that overrides the probe modulated curve in Figure 5.12(a)-III. The overall slow thermal relaxation of bR molecules is responsible for this behaviour. The direct consequence of slow thermal relaxation of bR is the fall in contrast ratio with increase in pump illumination rate.

The variation of contrast ratio, and switching time with pump illumination rate measured at three different pump power levels are shown in Figure 5.13(a) and 5.13(b), respectively. Again, the contrast ratio has nonlinear dependence on the pump intensity in the sense that incremental change in pump does not result in same incremental change in contrast at hight pump intensities as it does at low intensities. If the width of the pump pulse is D, then for $D >> \tau_{\text{eff}}$, the population distribution of bR molecules reaches a steady–state before the pulse ends. As D is shorten, i.e., $D << \tau_{\text{eff}}$, the pump pulse ends much before the time required to reach the steady–state. Likewise, when the pump is off, due to slow thermal decay rate not all the molecules in the photocycle are able

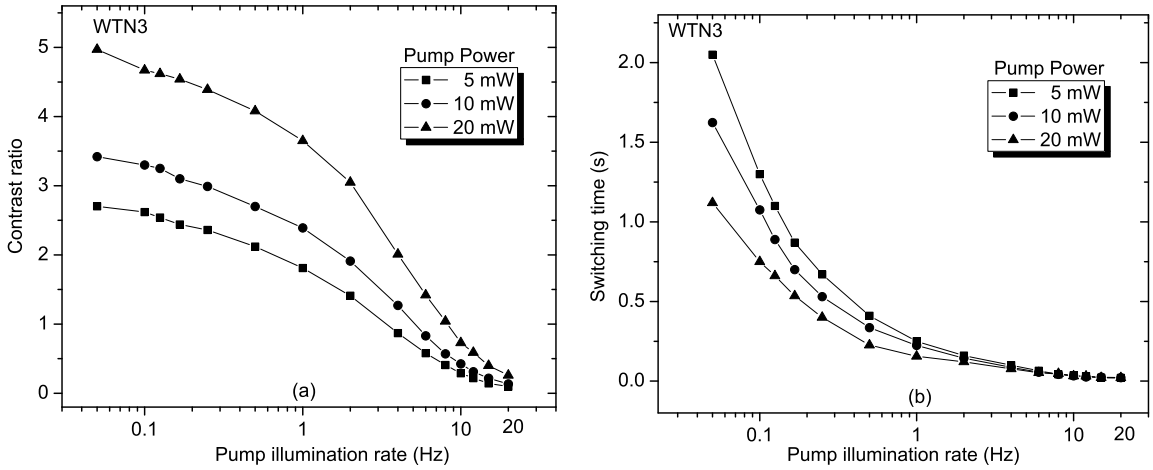

Figure 5.13: Variation of (a) contrast ratio and (b) switching time with pump illumination rate in wild–type BR sample measured at 5 mW, 10 mW and 20 mW pump powers and 543 nm probe. The probe beam power was $\approx 5\ \mu W$.

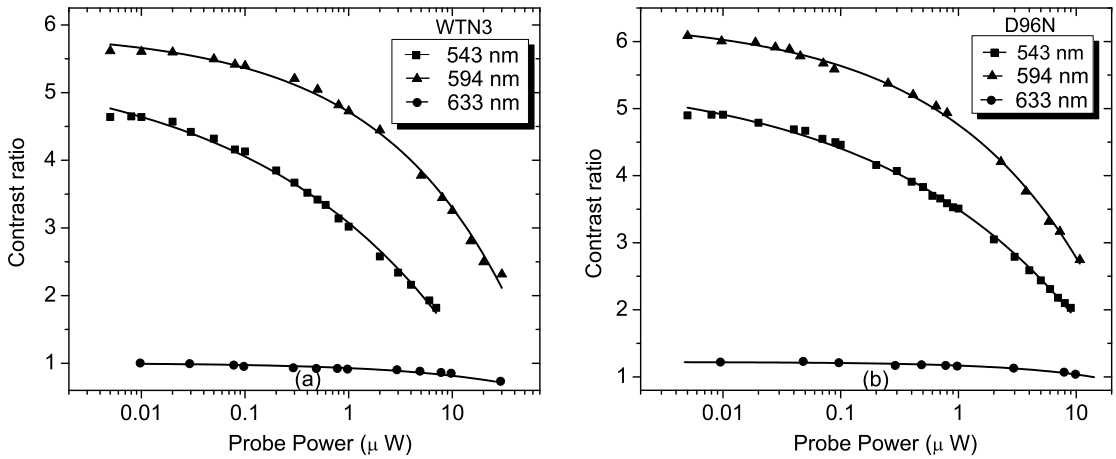

Figure 5.14: Contrast ratio as a function of probe beam intensity at 10 mW pump and 1 s illumination rate. (a) for wild-type and (b) for D96N. The solid curve is power law fit to the experimental data points represented by different symbols.

to relax to the ground state B before the arrival of the next pump pulse. Consequently, the power level designating 'on-state' is lowered while the 'off-state' is raised. Therefore, large thermal relaxation time leads to low contrast and slow switching rates. The detailed experimental results concerning switching time and contrast ratio are summarized in Table 5.3. For comparison, some of the recent studies in all-optical switching in bR, are recorded in Table 5.4.

The high switching contrast reported in Ref. [202, 203] is obtain using photoinduced anisotropy. That is, when a film is illuminated by a linearly polarized light, only those bR molecules whose transition dipole-moment vector is oriented along the polarization vector of the incident light, are saturated, while those with perpendicular direction are spared. This anisotropic distribution of bR molecules results in photoinduced dichroism and photoinduced birefringence. The photoinduced birefringence can appreciably rotate the polarization vector of incident probe beam, which can be completely blocked by an analyzer oriented appropriately and placed the in beam's path to yield high contrast. The photoinduced anisotropy based studies in our bR films will be taken up in near future.

The measurements of contrast ratio were also made by varying the probe beam power

Table 5.3: The measured range of contrast ratio and switching time when the pump illumination rate was varied from 0.1 Hz to 10 Hz. The probe beam power was fixed at 5 μW.

λ_{probe}	pump power	contrast ratio		switching time (s)	
(nm)	(mW)	WTN3	D96N	WTN3	D96N
633	5	1.35–0.01	1.60–0.01	1.90–0.02	1.82–0.02
	10	1.54–0.01	1.89–0.02	1.80–0.02	1.76–0.01
	20	1.72–0.02	2.08–0.02	1.46–0.02	1.68–0.01
594	5	3.59–0.08	6.15–0.10	2.2–0.02	2.75–0.02
	10	4.77–0.15	7.71–0.18	1.92–0.02	2.31–0.02
	20	5.69–0.21	8.66–0.25	1.22–0.02	1.95–0.02
543	5	2.70–0.10	2.74–0.08	2.05–0.02	2.84–0.02
	10	3.42–0.14	4.13–0.15	1.62–0.02	2.06–0.02
	20	4.97–0.03	4.96–0.23	1.12–0.02	1.71–0.02

from 5 nW to 15 μW while keeping the pump power fixed at 10 mW with 1s illumination. Contrast ratio is high at weak probe and appears to drop as the probe intensity is increased. Figure 5.14 depicts the results of contrast change for wild-type and D96N films at different probe intensities. The contrast ratio shows a power law dependence on the probe intensity that has the form $R = a_0 + a_1 I_s^{\gamma}$, where a_0 and a_1 are constants and γ is intensity power

Table 5.4: All-optical switching studies in bR from literature.

bR sample & method	Wavelength/Intensity		Rise/Decay	Contrast	References
	λ_{pump}	λ_{probe}	(s)		
WT film ; PIA†;	532 nm	660 nm	0.6/1.5	1000:1	[203]
OD=3 @ 570 nm;	500 mWcm^{-2}	5 mWcm^{-2}			
WT film; PIA;	568 nm	633 & 442 nm	–	80:1	[202]
OD=5 @ 570 nm;	300 mWcm^{-2}	250 mWcm^{-2}			
WT film; LIA‡;	532 nm	635 nm	0.016/–	0.2–0.85	[206]
OD=3 @ 570 nm;	470 mWcm^{-2}	10.8 mW			

† PIA: Photoinduced anisotropy; ‡LIA: Light-induced absorption

Table 5.5: The best fit parameter values for the power law dependence of contrast ratio on probe beam intensities in WTN3 (D96N) bR films.

λ_{probe}	a_0	a_1	γ
633 nm	1.00 ± 0.01	-0.07 ± 0.01	0.40 ± 0.02
	(1.28 ± 0.02)	(-0.11 ± 0.02)	(0.38 ± 0.02)
594 nm	5.93 ± 0.08	-1.19 ± 0.1	0.34 ±0.02
	(6.31 ± 0.04)	(-1.46 ± 0.06)	(0.34 ± 0.01)
543 nm	5.51 ± 0.13	-2.13 ± 0.14	0.22 ± 0.01
	(5.54 ± 0.07)	(-2.05 ± 0.08)	(0.25 ± 0.01)

index. The best fit values of these parameters for both the films are listed in Table 5.5. However no significant variation of switching time was observed with probe intensity. A brief comparison between two bR samples shows that D96N film has slightly better contrast than wild–type film. In addition, D96N has somewhat slow response time as compared to the wild-type film. Otherwise, there no marked difference between their absorption and switching properties.

5.5 Conclusion

A time-dependent multistate model for bR photocycle is presented. The model incorporates both temporal and intensity dependence of population densities for different bR states. Simulation results obtained for a typical wild type sample provide a better understanding of bR dynamics and its steady-state behaviour that can be used to optimize its performance in device applications.

A nonlinear-absorption based experimental studies of all-optical switching in bR films is presented. The switching response of the films was characterized using several exper-

imentally controllable parameters like, pump and probe beam intensities, probe wavelengths, and pump illumination rate. Experimental results were interpreted using a model based on simplified three–level scheme. Though, far from being exact, the model is useful for semi-quantitative analysis of nonlinear absorption in bR sample.

For an error-free transmission and processing, a high contrast is necessary to ensure a better discrimination of signal in a noisy environment. The contrast in absorption based switching can be maximized by suitable selection of probe wavelength that has a absorption overlap with most of the intermediate states as well as ground state. To that effect, we find 594 nm and 543 nm wavelengths are better suited both in terms of improved contrast and faster switching response times as compared to 633 nm.

Chapter 6

Future Goals

The broad fields of holographic data storage and optical switching have manifold possibilities for research and technological development for future applications. The discussion in this chapter will be confined to the specific areas of research that can be taken-up as a natural extension of the work presented in this thesis. Some of the research problems, projected as future goals, are described in the following:

Two-center Hologram Recording in Fe:Ce:Ti:$LiNbO_3$

One of the main issues of concern in holographic memories is volatility of the stored data. That is, the repeated read-out cycles, gradually erase the recorded information and increases the scattering noise. It is the same mechanism that is responsible for hologram formation, (i.e., charge excitation, transport and trapping at impurity centers) which eventually weaken the index grating upon continuous readout. Therefore, hologram fixing is absolutely necessary for nondestructive readout of the data.

To overcome this problem, Buse *et al.*, proposed a two-center holographic recording in doubly doped Fe:Mn:$LiNbO_3$ crystal [210]. This crystal has iron (shallower trap) and manganese (deeper traps) as two different deep traps. Initially, the deep centers are filled with electrons and crystal remains transparent in the visible region. Though, illuminating the crystal with ultraviolet radiations can effectively ionize the Mn traps. The liberated electrons in turn populate the iron traps. Now the visible radiations can be used to photoexcite the electrons from iron centers and send them back to Mn traps. Therefore, ultraviolet pre-exposure sensitizes the material before a hologram is written with visible light. The subsequent hologram read-outs with light of visible wavelength does not alter

the space-charge pattern that is embedded in deeper traps. The hologram can only be erased with shorter wavelength UV light.

In triply doped Fe:Ce:Ti:$LiNbO_3$ crystal that we used, Ti impurities are deeper trap, whereas Ce and Fe are shallower traps. Cerium is known to be an effective trap center just as iron. Additionally, the presence of cerium (Ce) in $LiNbO_3$ crystal, leads to substantial increases in sensitivity towards red spectral region [76]. In the present work on Fe:Ce:Ti:$LiNbO_3$ (Chapter 2), we have observed diffraction efficiency as high as 80% in visible wavelengths. The holographic data storage demonstrated in Chapter 4, was also based on one-colour or single wavelength recording. Therefore, two-center recording in Fe:Ce:Ti:$LiNbO_3$ merits a detailed investigation so as to explore and understand the role of Ti in realizing non-volatile holographic memories.

Phase & Polarization Encoded Data Page for HDSS

Two-dimensional optical information processing systems, in general, require some means to spatially modulate the wavefront of the light beam. A light beam can be represented by a 2-dimensions complex-valued function in phaser notation as [127]:

$$\boldsymbol{f}(x,y) = A(x,y)\,\widehat{\mathbf{p}}\,\exp[i\,\phi(x,y)] \tag{6.1}$$

where, $A(x,y)$ is a real and nonnegative amplitude, $\widehat{\mathbf{p}}$ is polarization vector and $\phi(x,y)$ is a real phase distribution. The phase front of a laser beam has certain values of amplitude, phase and polarization at every point. If $g(x,y)$ is the input image, then the optical replica $f(x,y)$, of the input image is obtained by wavefront modulation of the light beam at every point (x,y). The image pixel value at (x,y) can be mapped to corresponding (x,y) spatial location on the light wavefront by spatially encoding the intensity or the phase or the polarization state at that point. This is how the information is imprinted onto the object beam. Using Eq. (6.1), the intensity modulated image can be obtained using,

$$\begin{aligned} |A(x,y)|^2 &= k_1 \cdot g(x,y) \\ \phi(x,y) &= \text{constant} \end{aligned} \tag{6.2}$$

where k_1 is a scaling function. The polarization rotation property of the SLM was used for composing a *intensity-modulated* data page for hologram recording. The theory of SLM that describes the intensity modulation properties of the twisted liquid crystal cell is presented in Chapter 3. As pointed out elsewhere (Chapter 4, section 4.3), the

holographic data storage based on intensity modulated input page used in Fourier geometry has two disadvantages. First, the intensity modulated data page has a highly nonuniform distribution of light at the Fourier plane where the data is recorded. This is illustrated in Figure 6.1, where, a picture of Lena and its computed Fourier transform image is shown. It

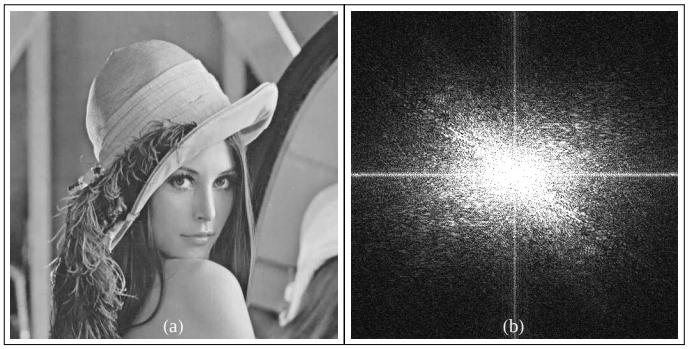

Figure 6.1: (a) Lena image, (b) computed Fourier image of Lena image.

can be noticed from the Fourier image in Figure 6.1(b) that most of the energy is confined only within the small central region. The strong low frequency components near center, saturate the recording material locally. Therefore, the finer details of the image that are present in high frequency components, are poorly registered. Eventually, the quality of reconstructed image suffers from low-pass blur and unwanted nonlinear distortions. The drawbacks of intensity modulated image, can be effectively overcome using phase modulation of the image data. In a phase-modulated data page, each LC cell imparts a certain phase to the light that passes through it. Imparted phase is proportional to the grey level of the image pixel in the input image. The intensity distribution across the Fourier image of a phase-modulated data page is more uniform. From Eq. (6.1), the phase modulation is achieved by allowing

$$\begin{aligned} |A(x,y)| &= \text{constant} \\ \phi(x,y) &= k_2 \cdot g(x,y) \end{aligned} \tag{6.3}$$

where, k_2 is a scaling parameter. A phase encoded version of Lena image generated using Eqs. (6.1) and (6.3) is shown in Figure 6.2(a). In this image, the input pixel range (0-255) was linearly re-scaled to $(0-10\,\pi)$ rad using $k_2 = 10\,\pi/255$. The corresponding Fourier transformed images for different values of scaling parameter k_2 are shown in Fig. 6.2(b)-6.2(d). Clearly, the low frequency Fourier components of the phase image are not as strong as in Figure 6.1(b). Further, the degree of energy spread from low frequency to higher

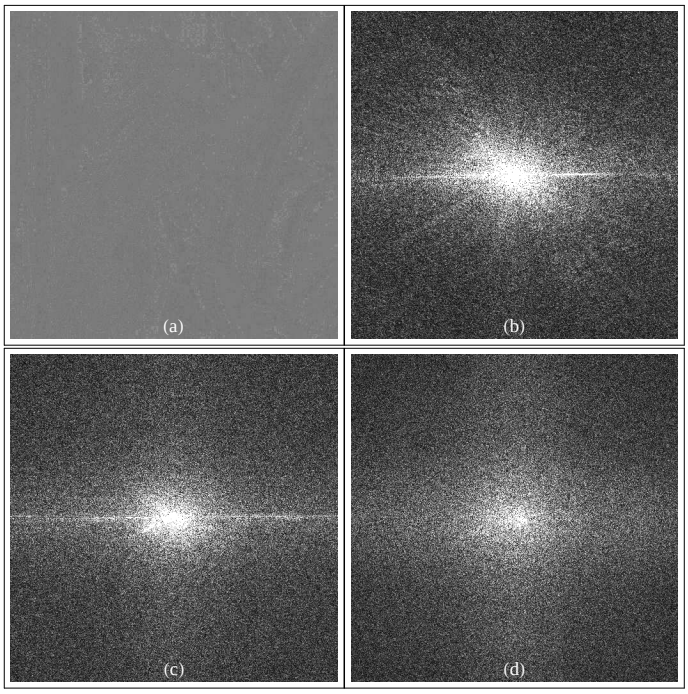

Figure 6.2: (a) Phase encoded Lena image, (b) computed Fourier transform of the phase image for $k_2 = 10\,\pi/255$, (c) for $k_2 = 20\,\pi/255$ and, (d) for $k_2 = 50\,\pi/255$.

frequency components is proportional to the scaling parameter k_2. In other words, larger the phase encoding range, more uniform is the energy distribution in the Fourier image. Recently, Renu *et al.* have shown that the parallel search capabilities based on associative retrieval of phase-modulated data pages yield better discrimination thresholds [211].

Despite all the advantages and attractive features, a practical demonstration of actual image storage and retrieval using phase-modulated data page is yet to be seen. Two main reasons for this inadequacy are:

(1) The design of most of the commercially available SLMs are optimized for applications that require amplitude modulation. In terms of phase modulation, their dynamic range is rather limited.

(2) For information retrieval, the phase encoded data needs to be converted into intensity coded data page. The conversion is not straightforward and requires interferometric techniques which are often complex and impose extra constrains on other system components.

A proposed but untested scheme based on a combination of phase & polarization encoding is shown in Figure 6.3. In this scheme, an information bit is represented together by a

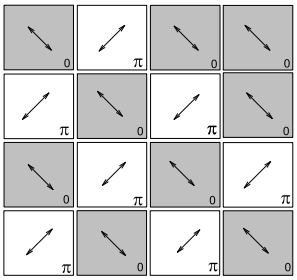

Figure 6.3: Schematic for phase and polarization encoding of 2-dimensional binary data. The grey squares (0 bit) have a phase of 0 rad, whereas the white squares (1 bit) has a phase of π rad. The corresponding direction of polarization is indicated by the arrows.

fixed polarization and a fixed phase. Such a scheme may have all the advantages that phase-modulation seems to offer. Without having the need for separate interferometry based detections, a simple linear polarizer may be used for converting phase information into intensity. The only requirement is that a storage media should be able to record and discriminate both the orthogonal polarizations states. Future studies in these direction would constitute an important contribution towards phase-based holographic data storage.

Improving the Switching Response of bR Films

In Chapter 5, the diminishing contrast ratio at high pump excitation rates can be attributed to slow response time due to the accumulation of bR molecules in M state. The thermal relaxation time of M state is of order of few seconds and nearly zero absorption cross-section at pump wavelength 532 nm. To a certain extent we can overcome this difficulty by continuous irradiation of the bR sample with a violet light source around 410 nm. The presence of violet light acting as a catalyst can greatly enhance the M $\Rightarrow$ B photoconversion, thereby resulting in a faster response time. In our preliminary experiments we could reduce switching response time by almost one order of magnitude with simultaneous illumination of the films with light a 488 nm from Argon ion laser. Though a small loss in contrast ratio was inevitable. The current performance of these films can be further optimized using a catalytic light source with a wavelength closer to M state absorption. In addition, as mentioned in section 5.3.2, the switching contrast itself can be substantially enhanced using photoinduced anisotropy. It would be worthwhile to undertake these complimentary studies in order to evaluate the performance and suitability of bR in all-optical switching.

Appendix A

Equipments and Accessories

The appendix covers the details of main instruments and accessories used in the experimental work presented in this thesis. Important specifications and operational characteristics of laser sources, detectors, data acquisition and interfacing systems are highlighted as a guiding tools.

A.1 Laser Sources

A.1.1 BeamLok^{TM} 2085: Argon-ion Laser (Spectra Physics)

The complete BeamLok^{TM} 2085 Argon-ion laser system consists of a BeamLok laser head, a high–current power supply (Model 2580), a remote control module (Model 2474), a water cooler, a Z-Lock and a J-Lok accessories.

BeamLok laser head comprises a temperature compensated mechanical resonator, a plasma tube with increased mode volume, high–field magnet and an active BeamLok beam–positioning system. The three bar resonator and an advanced plasma tube design is combined to provide a stable and excellent beam quality. The automatic gas fill keeps the plasma tube filled to an optimum gas pressure. An intracavity passive catalyst minimizes the build-up of contaminating O_3 gas by converting it to less harmful O_2 thereby eliminating the need of interacavity N_2 purging.

BeamLok is an advanced positioning system that dynamically locks the laser beam to a fixed reference point beyond cavity. The beam movement is continuously monitored with the help of position detectors and electronics system. The laser beam pointing stability is ensured by a feedback signal that drives the mirror actuators to compensate for any drift.

In *power mode* operation, the BeamLoK mechanism actively controls both the output power and the beam position.

A convenient remote control BeamLok module allows: current or power mode operation, sensitivity range selection, digital display of laser power output, tube voltage and current readings, interlock water flow and temperature status. There is also an analog meter that comes handy while tuning the laser for maximum output.

A resonant optical cavity is defined by two mirrors –the output coupler and the high reflector. The laser output is only a fraction of cavity energy transmitted by the output coupler. Both these mirrors are coated to reflect a specific wavelength. The selection of an appropriate cavity mirrors allows the laser output at desired wavelength. At maximum current, a single frequency output up to 8 W and multiline output up to 25 W are achievable. A prism inserted in the cavity limits the oscillation of the laser to a single line. The dispersion of the prim allows only one line to be perfectly aligned with high reflector. The range of available wavelength and some of the operational characteristics[†] of BeamLok^{TM} 2085 laser model are listed below [212]:

Prominent wavelengths:

- Visible range (λ): 476 nm, 488 nm, 496 nm, 514.5 nm, and 528.7 nm
- Mid-UV range (λ): 351.1 nm, 351.4 nm, and 363.8 nm

Beam diameter at $1/e^2$ point: 1.9 mm

Beam divergence, full angle: 0.45 mrad

Polarization state: vertical, $> 100 : 1$

Cavity length with (without) prism: 1.78 m (1.71 m)

Mode spacing with (without) prism: 84 MHz (87 MHz)

Power mode stability: $\pm 0.5\,\%$

Current mode stability: $\pm 1.0\,\%$

Frequency jitter: ≤ 3 MHz

Power consumption: 57 kW

[†]These specification are valid only when both Z-Lok and J-Lok are enabled.

Water flow rate: 18.9 l/min

Inlet temperature: 10–35°

Z-Lok and J-Lok Accessories

A free–running laser cavity of length 2 to 3 m can support typically up to 30 to 60 longitudinal modes. A single mode operation is realized by adding a thin etalon to the cavity. The large free-spectral range (greater than the width of laser gain profile) of the etalon allows only one of the cavity modes to oscillate. The cavity length as well as the etalon thickness might vary due to change in ambient temperature. Even a very small detuning between the cavity length and the etalon thickness leads to mode hopping which in turn results in a substantial power loss.

Z-Lok system (Model 587) is an interacavity based etalon and electronic controller accessory meant to provide automated single-mode frequency operation with constant output power. When combined with BeamLok, it controls the laser cavity length to stabilize both frequency and beam motion. The intracavity etalon is thermally isolated and stabilized at optimum laser output at the selected frequency. The electronic module also controls and monitors the laser cavity length by monitoring output power or current. It modifies the BeamLok signal to three-element piezoelectric (PZT) transducer system to provide a single frequency mode-hops free operation.

While laser is on, the excessive amount of heat generated in the plasma tube is removed by water convection. High pressure water flow around plasma tube creates acoustic vibrations which produce jitter in the laser output. Here, jitter refers to the rapid fluctuations in laser frequency ($\sim$ 15 MHz) due to mechanical vibrations.

J-Lok modules (model 588) consists of a scanning Fabry-Perot interferometer and interferometer driver. It scans a part of the incoming laser beam to detect different frequencies and their respective intensities. The different frequency components can be displayed on the oscilloscope. When used in conjunction with Z-Lok, J-Lok selects the single frequency component. Once locked to single frequency, J-Lok controller sends a correction signal to Z-Lok electronic module to stabilize the system at the desired frequency. Two error signals modify the cavity length via PZT driven output coupler. The Z-Lok uses laser output power as a reference source for long term stability, whereas J-Lok monitors and corrects the short term frequency shifts in a single mode laser operation. In the present case,the J-Lok can mitigate the jitter effects almost by a factor of ten.

A.1.2 Millennia^{TM} V: (Spectra Physics)

Millennia^{TM} V is a diode–pumped, hight power (5 W), solid-state, cw laser that produces 532 nm output. The complete system includes Millennia V laser head, a power supply, a chiller and a control module.

The Millennia V laser head encloses the optical resonator, the neodymium yttrium vanadate (Nd:YVO_4) gain medium, focusing optics, lithium triborate (LBO) as a doubling crystal and diode laser fiber delivery bundle. The output from two high-power, fiber coupled laser diode bars is used to end-pump the laser gain medium Nd:YVO_4. The diode-pumped light is absorbed by the crystal and emitted as diffraction limited, 10 W output at 1064 nm. The Millennia V uses a 90°, noncritically phase-matched, temperature-tuned LBO nonlinear crystal as doubling medium which converts the 1064 nm light to the 532 nm green output. The LBO assembly is housed in an oven that maintains the optimum temperature for stable output. The main specifications of Millennia^{TM} V are as follows [213]:

Output power: 5 W

Operating wavelength: 532 nm

Spatial Mode: TEM_{00}

Beam diameter at $1/e^2$ points: < 2.5 mm

Beam divergence, full angle: < 0.5 mrad

Polarization state: vertical, $> 100 : 1$

Power stability: $\pm 1.0\%$

Power requirement: 220 Vac, 6 A, 50 Hz

All operations of the laser can be easily handled by Millennia V control module handset.

A.1.3 3900S: CW Ti:Sapphire Laser (Spectra Physics)

3900S, Ti:Sapphire is tunable solid-state laser that has only optical components without any electronic or electrical control. The Ti^{3+} ion is responsible for the laser action of Ti:sapphire. The model 3900S can be pumped either by 2085 argon-ion laser or Millennia V solid state laser. The wavelength tuning is achieved by a birefringent filter made of three

crystalline quartz plates, placed inside the cavity. The filter has a free spectral range of 150 nm. The desired wavelength is selected by rotating the filter about an axis normal to the plate. In order to achieve a narrow linewidth (< 15 GHz) operation, a thin etalon may be added to the cavity. Tuning is accomplished by either angular adjustment of the etalon or by temperature control of the etalon housing. The main specifications of 3900S model are [214]:

Tunable wavelength range: 750-950 nm

Average power: up to 1 W using 5 W pump.

Beam diameter at $1/e^2$ points: 0.95 mm

Linewidth: < 40 GHz

Beam divergence, full angle: $<$ 1 mrad

Spatial mode: TEM_{00}

Polarization state: horizontal, $> 100 : 1$

Power stability: $< 3\,\%$

A.1.4 He-Ne Lasers

The main features[1] of He–Ne laser sources are listed in Table A.1:

Table A.1: Specifications of He-Ne laser sources.

Specifications	Laser 1	Laser 2	Laser 2
Model	25-LHR-151-230	1673P	25 LYR-173-230
Supplier	Melles Griot	JDS Uniphase	Melles Griot
Power	15 mW	4 mW	2 mW
Wavelength	632.8 nm	543.5 nm	594.1 nm
Polarization	random	random	random
Beam diameter ($1/e^2$)	0.8 mm	0.8 mm	0.75 mm
Far-field divergence	1.0 mrad	0.86 mrad	0.91 mrad

[1] Taken from manufacturer's data sheet

A.2 TM-1320-15CL: CCD Camera (PULNiX)

TM-1320-15CL is a high resolution, compact size, monochrome progressive scan CCD camera. It has both video as well as digital camera link output. Camera Link^{TM} is a new industrial standard which includes data transmission as well as camera control and asynchronous serial communication –all in one cable. The standard defines a single connector for both digital cameras and image acquisition boards to ensures a smooth interchangibility among all the camera link products. Detailed product specifications[2] are listed in the Table A.2.

Table A.2: TM-1320-15CL CCD camera specifications.

Number of pixel: 1300 (H)× 1030 (V)	Pixel size: 6.7 μm × 6.7 μm
Active area: 8.7 mm (H) × 6.9 mm (V)	Shutter speed: 1/25 to 1/16,000 s
Frame rate: 15 frames/s	Image resolution: 8-bit
Typical noise level: 30 electrons	Well capacity: 16,000 electrons
Data clock output: 25.00 MHz	S/N ratio: 50 dB min
Analog video output: 1.0 V_{p-p}, 75Ω	Lens mount: $2/3''$ C-mount
Digital video output: 8-bit RS-644	Power req: 12V DC±10%, 37–390 mA

TM-1320-15CL CCD camera was controlled using National Instruments' PCI-1428 image acquisition board which supports the camera link technology.

A.3 IMAQ Vision Builder: (National Instruments)

NI–IMAQ Vision Builder is a tool for prototyping and testing image processing applications. The driver software that comes with NI image acquisition hardware includes, National Instruments' Measurement and Automation Explorer for camera configuration, and acquisition functions for NI LabVIEW, C, and Visual Basic. IMAQ Vision Builder offers an easy interface between image acquisition board PCI-1428 and the CCD camera. This interface makes camera setting, control and image acquisition processes extremely easy and straightforward.

In addition, IMAQ Vision Builder offers several powerful and advanced image processing and analysis functions. Some of these functions are: histogram processing, pattern matching, image calibration and correction, blob analysis, centroid detection, spatial and

[2]Taken from manufacturer's data sheet

Fourier domain filtering, logical and arithmetic operations, particle analysis, gray scale and binary morphological operations.

A.4 4832-C: Multi-Channel Optical Power Meter (Newport)

The 4832-C Multi-Channel Optical Power Meter is NIST calibrated, plug-in card based instrument used for making highly accurate and fast optical measurements. The model 4832-C comprises, four channel amplifier box, semiconductor large area detectors and a PC plug-in card.

The amplifier box contains analog to digital convertor and amplifier unit for each channel. It has a provision for simultaneous measurement from four detectors. The 4832-C is compatible with Newport's low power, 818 series detectors. Each channel is optimized for a specific detector, for maximizing bandwidth and minimizing the noise level. The detector connected to respective channel on the amplifier box, comes with its *factory-programmed* calibration modules that contain responsibity data and other information required for making accurate and calibrated measurements.

The 4832-C interfaces directly with the host computer through the PC ISA bus. A serial interface (15 feet long) cable connects the back plane of the amplifier box to a PC plug-in controller card inserted in the ISA slot of the host computer. A high performance processor on PC plug-in card handles all the instrument ranging and data acquisition commands. Some of the important specifications of 4832-C device are listed below: [215]

Typical current consumption from PC:
+5V at 1A
+12V at 125 mA
-12V at 125 mA

Analog Output:
Full scale voltage: 0–2.5 V at 1 MΩ
Accuracy: ±2.5%

Full scale current: 2.52 nA – 2.52 mA for signal range 0–6

A/D resolution (12 bit): 615 fA – 615 nA for signal range 0–6

A/D resolution (15 bit): 77 fA – 77 nA for signal range 0–6

Typical accuracy: $\pm 0.1\,\%$

Ranging time: 2 ms – 200 μs for signal range 0–6

Available measurements units: Watts, dBm, Amps, and Volts

A.4.1 LabVIEW Driver Software

The 4832-C power meter has following software options:
Software driver and utilities for DOS based C language development environment, 4832-C terminal emulator for Windows for easy communication & measurements and LabVIEW software drivers. LabVIEW is a 4th generation graphical programming language from Na-

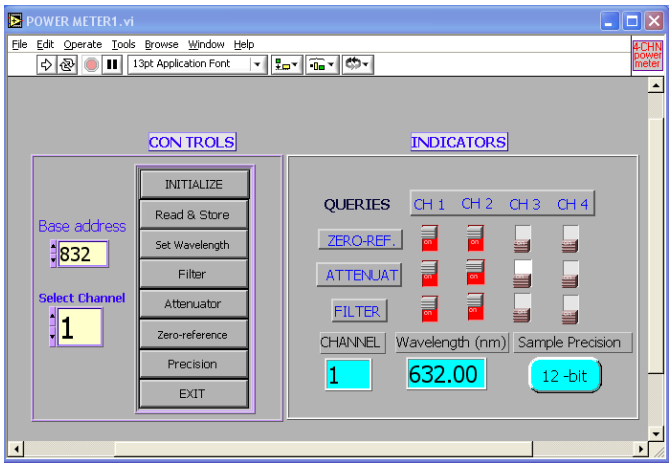

Figure A.1: One of the front panels of a LabVIEW program that controls 4832-C power meter in lab.

tional Instruments, used primarily in data acquisition and instrumentation controls. The graphical paradigm significantly simplifies programming tools and cuts down on development and debugging time. LabVIEW programs/subroutines are called virtual instruments (VIs). Each VI has two components, a block diagram and a front panel. Controls and indicators on the front panel allow an operator to input data into or extract data from a running virtual instrument. The main benefit of LabVIEW over other development environments is the extensive support for accessing several types of instrumentation hardware without worrying about the machine level details.

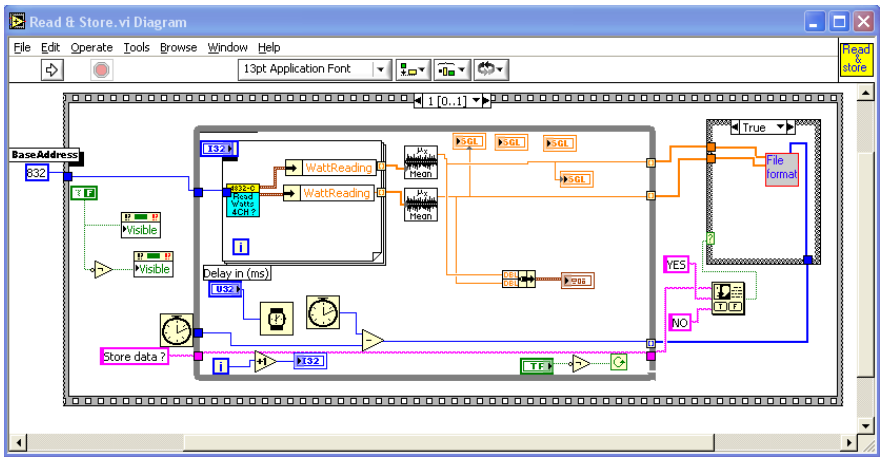

Figure A.2: One of the block diagrams of a LabVIEW program that reads and stores the data.

The 4832-C LabVIEW driver library contains as many as 40 VIs and sub–VIs. Each VI performs a specific task while communicating with the 4832-C instrument. These VIs and sub-VIs can be combined in an advanced LabVIEW program to perform several independent tasks. For example, the LabVIEW application program that we developed in the lab, initializes the 4832-C power meter, displays the measured data from all four channels on the computer screen, allows the user to specify the wavelength, number of measurements to be made, etc. The graphical user interface (GUI) interface also allows to toggle the attenuator, zero–reference, precision and filter settings. In addition, the acquired data from all the channels can be stored in a text file for further processing. Main controls and indicators in the front panel of the power meter LabVIEW program are shown in Figure A.1. The block diagram of a sub–VI that reads and stores the data is shown in Figure A.2.

A.4.2 818 Series Photo Detectors

The specifications[‡] for the large area semiconductor (818 series) optical detectors used with 4832-C model are provided in Table A.3.

Table A.3: 818 series detector specifications.

Detector model	818-UV/CM	818-SL/CM	818-IR/CM
Material	Silicon	Silicon	Germanium
Active area (cm^2)	1.0	1.0	0.71
Spectral range (nm)	190–1100	400–1100	780–1800
Maximum average power (W/cm^2)	0.2	2.0	2.0
Accuracy (%)	± 2	± 2	± 3
Linearity (%)	± 0.5	± 0.5	± 0.5
Saturation current (mA/cm^2)	0.1	4.6	400
Peak responsibity (A/W)	> 0.4 at 850 nm	> 0.5 at 920 nm	> 0.8 at 1550 nm
Rise time (μs)	≤ 2	≤ 2	≤ 2

[‡]Applicable with the calibration module and OD3 attenuator.

Bibliography

[1] T. H. Maiman, "Optical and microwave-optical experiments in Ruby," *Physical Review Letters* **4**, pp. 564–566, 1960.

[2] P. A. Franken, A. E. Hill, C. W. Peters, and G. Weinreich, "Generation of optical harmonics," *Physical Review Letters* **7**, pp. 118–119, 1961.

[3] W. Kaiser and G. C. B. Garrett, "Two-photon excitation in CaF2; Eu^{2+},," *Physical Review Letters* **7**, pp. 229–231, 1961.

[4] E. J. Woodbury and W. K. Ng, "Ruby laser operation in the near IR," in *Proc. IRE 50*, pp. 2367–2371, 1962.

[5] P. D. Maker, R. W. Terhune, and C. M. Savage, *Optical Third Harmonic Generation*, Columbia University, New York, 1964.

[6] P. D. Maker and R. W. Terhune, "Study of optical effects due to an induced polarization third order in the electric field strength," *Physical Review Letters* , pp. 801–818, 1965.

[7] J. A. Armstrong, N. Bloembergen, J. Ducuing, and P. S. Pershan, "Interactions between light waves in a nonlinear dielectric," *Physical Review* **127**, pp. 1918–1939, 1962.

[8] L. Millar, "Novel organic materials with exceptional nonlinear optical properties," Available at: `http://www.otm.uiuc.edu/techs/listingsearch.asp`.

[9] A. Ashkin, G. D. Boyd, J. M. Dziedzic, R. G. Smith, A. A. Ballman, J. J. Levinstein, and K. Nassau, "Optically-induced refractive index inhomogeneities in $LiNbO_3$ and $LiTaO_3$," *Applied Physics Letters* **9**, pp. 72–74, 1966.

[10] F. S. Chen, "Optically induced change of refractive indices in $LiNbO_3$ and $LiTaO_3$," *Journal of Applied Physics* **40**, pp. 3389–3396, 1969.

[11] J. J. Amodei, D. L. Staebler, and A. W. Stephens, "Holographic storage in doped barium sodium niobate ($Ba_2NaNb_5O_{15}$)," *Applied Physics Letters* **18**, pp. 507–509, 1971.

[12] N. V. Kukhtarev, V. B. Markov, S. G. Odulov, M. S. Soskin, and Vinetskii, "Holographic stoarge in electrooptic crystals. I. –Steady state," *Ferroelectric* **22**, pp. 949–960, 1979.

[13] N. V. Kukhtarev, V. B. Markov, S. G. Odulov, M. S. Soskin, and Vinetskii, "Holographic stoarge in electrooptic crystals. II. Beam coupling & light amplification," *Ferroelectric* **22**, pp. 961–964, 1979.

[14] J. Feinberg, D. Heiman, A. R. Tanguay, and R. W. Hellwarth, "Photorefractive effects and light-induced charge migration in barium titanate," *Journal of Applied Physics* **51**, pp. 1297–1305, 1980.

[15] D. Psaltis and F. Mok, "Holographic Memories," *Scientific American* **273**, pp. 52–58, 1995.

[16] J. Feinberg, "Photorefractive nonlinear optics," *Physics Today* , pp. 46–52, 1988.

[17] D. M. Pepper, J. Feinberg, and N. V. Kukhtarev, "The photorefractive effect," *Scientific American* **263**, pp. 34–40, 1990.

[18] D. M. Pepper, "Applications of optical phase conjugation," *Scientific American* **254**, pp. 56–65, 1986.

[19] G. Cedilnik, M. Esselbach, A. Kiessling, and R. Kowarschik, "Real-time holographic inteferometry with double two-wave mixing in photorefractive crystals," *Applied Optics* **39**, pp. 2091–2099, 2000.

[20] P. Kerkoc, M. Zgonik, K. Sutter, C. Bosshard, and P. N. Gunter, "4-(N,N-Dimethylamino)-3-acetamidonitrobenzene single crystals for nonlinear-optical applications," *Journal of Optical Society of America B* **7**, pp. 313–319, 1990.

[21] K. Sutter and P. N. Gunter, "Photorefractive gratings in the organic crystal 2-cycloocytylamino-5-nitropyridine doped with 7,7,8,8-tetracyanoquinodimethane," *Journal of Optical Society of America B* **7**, pp. 2274–2278, 1990.

[22] S. Ducharme, J. C. Scott, R. J. Twieg, and W. E. Moerner, "Observation of the photorefractive effect in a polymer," *Physical Review Letters* **66**, pp. 1846–1849, 1991.

[23] A. Motes and J. J. Kim, "Intensity-dependent absorption coefficient in photorefractive $BaTiO_3$ crystals," *Optical Society of America Journal B* **4**, pp. 1379–1381, 1987.

[24] G. A. Brost, R. A. Motes, and J. R. Rotge, "Intensity-dependent absorption and photorefractive effects in barium titanate," *Optical Society of America Journal B* **5**, pp. 1879–1885, 1988.

[25] D. Mahgerefteh and J. Feinberg, "Explanation of the apparent sublinear photoconductivity of photorefractive barium titanate," *Physical Review Letters* **64**, pp. 2195–2198, 1990.

[26] H. Kogelnik, "Coupled wave theory for thick hologram gratings," *Bell System Technology Journal* **2**, pp. 2909–2945, 1969.

[27] D. L. Staebler and J. J. Amodei, "Coupled-wave analysis of holographic storage in linbo[sub 3]," *Journal of Applied Physics* **43**, pp. 1042–1049, 1972.

[28] J. Joseph, P. K. C. Pillai, and K. Singh, "High-gain, low-noise signal beam amplification in photorefractive $BaTiO_3$," *Applied Optics* **30**, pp. 3315–3318, 1991.

[29] A. Marrakchi, J. P. Huignard, and P. Guenter, "Diffraction efficiency and energy transfer in two-wave mixing experiments with $Bi_{12}SiO_{20}$ crystals," *Applied Physics* **24**, pp. 131–138, 1981.

[30] J. Xu, G. Zhang, J. Liu, and S. Liu, "Noise-free, high-gain signal beam amplification using beam fanning in a photorefractive $KNbO_3$:Fe crystal," *Optics Communications* **107**, pp. 99–103, 1994.

[31] M. Kaczmarek and R. W. Eason, "Very-high-gain single-pass two-beam coupling in blue Rh:$BaTiO_3$," *Optics Letters* **20**, pp. 1850–1853, 1995.

[32] X. Mu, X. Xu, Z. Shao, M. Jiang, and H. Luo, "Low-noise and high-gain image amplification by contradirectional two-wave mixing," *Applied Physics Letters* **77**, pp. 337–339, 2000.

[33] G. W. Burr, H. Coufal, R. K. Grygier, J. A. Hoffnagle, and C. M. Jefferson, "Noise reduction of page-oriented data storage by inverse filtering during recording," *Optics Letters* **23**, pp. 289–291, 1998.

[34] Y. Fainman, C. C. Guest, and S. H. Lee, "Optical digital logic operations by two-beam coupling in photorefractive material," *Applied Optics* **25**, pp. 1598–1603, 1986.

[35] J. H. Hong, A. E. T. Chiou, and P. A. Yeh, "Image amplification by two-wave mixing in photorefractive crystals," *Applied Optics* **29**, pp. 3036–3040, 1990.

[36] P. Günter and J.-P. Huignard, eds., *Photrefractive Materials and their Applications I –Topics in Applied Physics*, vol. 61, Springer Verlag, 1988.

[37] P. Günter and J.-P. Huignard, eds., *Photrefractive Materials and Their Applications II –Topics in Applied Physics*, vol. 62, Springer Verlag, 1988.

[38] P. Yeh, *Introduction to Photorefractive Nonlinear Optics*, Wiley, 1993.

[39] M. Cronin-Golomb, B. Fisher, J. White, and A. Yariv, "Theory and applications of Four-Wave mixing in photorefractive media," *IEEE Journal of Quantum Electronics* **20**, pp. 12–30, 1984.

[40] D. Gabor, "A new microscope principle," *Nature* **161**, pp. 777–778, 1948.

[41] D. Gabor, "Microscopy by reconstructed wavefronts," in *Proceeding of the Royal Society*, 1949.

[42] E. N. Leith and J. Upatnieks, "Reconstructed wavefronts and communication theory," *Journal of Optical Society of America* **52**, pp. 1123–1130, 1962.

[43] E. N. Leith and J. Upatnieks, "Wavefront reconstruction with continuous-toneobjects," *Journal of Optical Society of America* **53**, pp. 1377–1381, 1963.

[44] R. F. van Ligten, "Influence of photographic film on wavefront reconstruction. I: plane wavefronts," *Journal of Optical Society of America* **56**, pp. 1–7, 1966.

[45] J. W. Goodman, "Effects of film nonlinearities in holography,," *Journal of Optical Society of America* **57**, pp. 560–564, 1966.

[46] J. P. van Heerden, "Theory of optical information storage in solids," *Applied Optics* **2**, pp. 393–400, 1963.

[47] F. S. Chen, J. T. LaMacchia, and D. B. Fraser, " Holographic storage in Lithium Niobate," *Applied Physics Letters* **13**, pp. 223–225.

[48] J. B. Thaxter, "Electrical control of holographic storage in Strontium-Barium Niobate," *Applied Physics Letters* **15**, pp. 210–212, 1969.

[49] J. F. Heanue, M. C. Bashaw, and L. Hesselink, "Volume holographic storage and retrieval of digital data," *Science* **265**, pp. 749–752, 1994.

[50] D. W. Vahey, "A nonlinear coupled-wave theory of holographic storage in ferroelectric materials," *Journal of Applied Physics* **46**, pp. 3510–3515, 1975.

[51] J. R. Wullert and Y. Lu, "Limits of the capacity and density of holographic storage," *Applied Optics* **33**, pp. 2191–2196, 1994.

[52] E. S. Maniloff and K. M. Johnson, "Maximized photorefractive holographic storage," *Journal of Applied Physics* **70**, pp. 4702–4707, 1991.

[53] S. Campbell, Z. Yuheng, and Y. Pochi, "Writing and copying in volume holographic memories: approaches and analysis," *Optics Communications* **123**, pp. 27–33, 1996.

[54] F. Grawert, S. Kobras, G. W. Burr, H. J. Coufal, H. Hanssen, M. Riedel, C. M. Jefferson, and M. C. Jurich, "Content-addressable holographic databases," in *Proc. SPIE Vol. 4109, p. 177-188, Critical Technologies for the Future of Computing, Sunny Bains; Leo J. Irakliotis; Eds.*, pp. 177–188, 2000.

[55] G. W. Burr, S. Kobras, H. Hanssen, and H. Coufal, "Content-addressable data storage by use of volume holograms," *Applied Optics* **38**, pp. 6779–6784, 1999.

[56] Y. S. Bai and R. Kachru, "Nonvolatile holographic storage with two-step recording in lithium niobate using cw lasers," *Physical Review Letters* **78**, pp. 2944–2947, 1997.

[57] G. A. Betzos, M. S. Porter, J. F. Hutton, and P. A. Mitkas, "Optical storage interactive simulator: An interactive tool for the analysis of page-oriented optical memories," *Applied Optics* **37**, pp. 6115–6126, 1998.

[58] K. Buse, A. Adibi, and D. Psaltis, "Novel method for persistent holographic recording in doubly doped lithium niobate," in *Proc. SPIE Vol. 3638*, pp. 15–21, 1999.

[59] F. H. Mok, G. W. Burr, and D. Psaltis, "System metric for holographic memory systems," *Optics Letters* **21**, pp. 896–898, 1996.

[60] Y.-H. Kim, S.-D. Sohn, and Y. H. Lee, "Storage of multiple holograms of equal diffraction efficiency in a phase-code multiplexing system," *Applied Optics* **43**, pp. 2118–2124, 2004.

[61] G. Berger, C. Denz, S. S. Orlov, B. Phillips, and L. Hesselink, "Associative recall in a volume holographic storage system based on phase-code multiplexing," *Applied Physics B – Lasers and Optics* **73**, pp. 839–845, 2001.

[62] H. Lee, X. Gu, and D. Psaltis, "Volume holographic interconnections with maximal capacity and minimal cross talk," *Journal of Applied Physics* **65**, pp. 2191–2194, 1989.

[63] A. Lahrichi, "Bit-error rate and system limitations on the storage capacity of volume holographic memory systems," *Optical Engineering* **40**, pp. 2392–2399, 2001.

[64] F. H. Mok, "Angle-multiplexed storage of 5000 holograms in lithium niobate," *Optics Letters* **18**, pp. 915–917, 1993.

[65] J.-W. An, N. Kim, and K.-W. Lee, "Volume holographic wavelength demultiplexer based on rotation multiplexing in the 90° geometry," *Optics Communications* **197**, pp. 247–254, 2001.

[66] D. Lande, J. F. Heanue, M. C. Bashaw, and L. Hesselink, "Digital wavelength-multiplexed holographic data storage system," *Optics Letters* **21**, pp. 1780–1782, 1996.

[67] X. An, D. Psaltis, and G. W. Burr, "Thermal fixing of 10,000 holograms in $LiNbO_3$:Fe," *Applied Optics* **38**, pp. 386–393, 1999.

[68] G. W. Burr, F. H. Mok, and D. Psaltis, "Angle and space multiplexed holographic storage using the 90° geometry," *Optics Communications* **117**, pp. 49–55, 1995.

[69] M. C. Bashaw, R. C. Singer, J. F. Heanue, and L. Hesselink, "Coded-wavelength multiplex volume holography," *Optics Letters* **20**, pp. 1916–1918, 1995.

[70] J. F. Hutton, G. A. Betzos, M. E. Schaffer, and P. A. Mitkas, "Error-correcting codes for page-oriented optical memories," in *Proc. SPIE Vol. 2848, p. 146-156, Materials, Devices, and Systems for Optoelectronic Processing*, pp. 146–156, 1996.

[71] G. W. Burr, J. Ashley, H. Coufal, R. K. Grygier, J. A. Hoffnagle, C. M. Jefferson, and B. Marcus, "Modulation coding for pixel-matched holographic data storage," *Optics Letters* **22**, pp. 639–641, 1997.

[72] D. E. Pansatiankul and A. A. Sawchuk, "Variable-length two-dimensional modulation coding for imaging page-oriented optical data storage systems," *Applied Optics* **42**, pp. 5319–5333, 2003.

[73] G. W. Burr, C. M. Jefferson, H. Coufal, M. Jurich, J. A. Hoffnagle, R. M. Macfarlane, and R. M. Shelby, "Volume holographic data storage at an areal density of 250 gigapixels in. 2," *Optics Letters* **26**, pp. 444–446, 2001.

[74] G. W. Burr and B. Marcus, "Coding tradeoffs for high-density holographic data storage," in *Proc. SPIE Vol. 3802, p. 18-29, Advanced Optical Data Storage: Materials, Systems, and Interfaces to Computers, Pericles A. Mitkas; Zameer U. Hasan; Hans J. Coufal; Glenn T. Sincerbox; Eds.*, pp. 18–29, 1999.

[75] J. F. Heanue, M. C. Bashaw, and L. Hesselink, "Channel codes for digital holographic data storage," *Journal of Optical Society of America A* **12**, pp. 2432–2439, 1995.

[76] X. Yue, A. Adibi, T. Hudson, K. Buse, and D. Psaltis, "Role of cerium in lithium niobate for holographic recording," *Journal of Applied Physics* **87**, pp. 4051–4055, 2000.

[77] Y. Liu, L. Liu, D. Liu, L. Xu, and C. Zhou, "Intensity dependence of two-center non-volatile holographic recording in $LiNbO_3$:Cu:Ce crystals," *Optics Communications* **190**, pp. 339–343, 2001.

[78] Y. Liu, L. Liu, L. Xu, and C. Zhou, "Experimental study of non-volatile holographic storage in doubly-and triply-doped lithium niobate crystals," *Optics Communications* **181**, pp. 47–52, 2000.

[79] J. Ashley, M.-P. Bernal, G. W. Burr, H. Coufal, H. Guenther, J. A. Hoffnagle, C. M. Jefferson, B. Marcus, R. M. Macfarlane, R. M. Shelby, and G. T. Sincerbox,

"Holographic data storage," *IBM Journal of Research & Development,* **44**, pp. 341–368, 2000.

[80] M.-P. Bernal, H. Coufal, R. K. Grygier, J. A. Hoffnagle, C. M. Jefferson, R. M. Macfarlane, R. M. Shelby, G. T. Sincerbox, P. Wimmer, and G. Wittmann, "A precision tester for studies of holographic optical storage materials and recording physics," *Applied Optics* **35**, pp. 2360–2374, 1996.

[81] A. Renn and U. P. Wild, "Spectral hole burning and hologram storage," *Applied Optics* **26**, pp. 4040–4042, 1987.

[82] N. A. Hampp, "Bacteriorhodopsin as a photochromic retinal protein for optical memories," *Chemical Review* **100**, pp. 1755–1776, 2000.

[83] R. R. Birge, N. B. Gillespie, E. W. Izaguirre, A. Kusnetzow, A. F. Lawrence, D. Singh, Q. W. Song, E. Schmidt, J. A. Stuart, S. Seetharaman, and K. J. Wise, "Protein-based associative processors and volumetric memories ," *Journal of Physical Chemistry B* **103**, pp. 10746–10766, 1999.

[84] H. J. Coufal, D. Psaltis, and G. T. Sincerbox, eds., *Holographic Data Storage*, Springer, 2000.

[85] R. M. Shelby, J. A. Hoffnagle, G. W. Burr, C. M. Jefferson, M.-P. Bernal, H. Coufal, R. K. Grygier, H. Günther, R. M. Macfarlane, and G. T. Sincerbox, "Pixel-matched holographicdata storage with megabit pages," *Optics Letters* **22**, pp. 1509–1511, 1997.

[86] F. Lai and J. Morris, "Towards Nanocomputer Architecture," in *Conferences in Research and Practice in Information Technology, Computer Systems Architecture 2002 -Vol 6, Feipei Lai; and John Morris; Eds.*, pp. 141–150, 2002.

[87] F. T. S. Yu, S. Jutamulia, and S. Yin, eds., *Introduction to Information Optics*, Academic Press, 2001.

[88] R. L. Fork, "Physics of optical switching," *Physical Review A* **26**, pp. 2049–2064, 1982.

[89] M. Xaio, H. Wang, and D. Goorskey, "Light controlling light with enhanced kerr nonlinearity," *Optics and Photonics News* **13**, pp. 45–48, 2002.

[90] D. Bishop, C. R. Giles, and S. R. Das, "The rise of optical switching," *Scientific American* **284**, pp. 88–94, 2001.

[91] S. A. Podoshvedov, "Switching effects in photorefractive crystals belonging to 3m point group of symmetry," *Optics Communications* **199**, pp. 245–255, 2001.

[92] S. A. Podoshvedov, "Energy conversion and all-optical switching in three-wave mixing in crystal with periodical modulation of χ^2 susceptibility," *Optics Communications* **189**, pp. 365–375, 2001.

[93] A. Yacoubian and T. M. Aye, "Enhanced optical modulation using azo-dye polymers," *Applied Optics* **32**, pp. 3073–3080, 1993.

[94] F. Z. Henari, "Optical switching in organometallic phthalocyanine," *Journal of Optics A: Pure Applied Optics* **3**, pp. 188–190, 2001.

[95] F. Z. Henari, K. H. Cazzini, D. N. Weldon, and W. J. Blau, "All optical switching based on intensity induced absorption in C_{60}," *Applied Physics Letters* **68**, pp. 619–621, 1996.

[96] C. P. Singh and S. Roy, "Dynamics of all-optical switching in C60 and its application to optical logic gates," *Optical Engineering* **43**, pp. 426–431, 2004.

[97] M. E. Crenshaw, M. Scalora, and C. M. Bowden, "Ultrafast intrinsic optical switching in a dense medium of two-level atoms," *Physical Review Letters* **68**, pp. 911–914, 1992.

[98] P. N. Prasad, *Introduction to Biophysics*, Wiley-Interscience, 1 ed., 2003.

[99] D. L. Wise, G. E. Wnek, D. J. Trantolo, T. M. Cooper, and J. D. Gresser, eds., *Photonic Polymer Systems Fundamentals, Methods and Applications*, New York: Marcel Dekker, Inc., 1998.

[100] W. Stoeckenius, R. H. Lozier, and R. A. Bogomolni, "Bacteriorhodopsin and the purple membrane of halobacteria," *Biochimica et Biophysica ACTA* **505**, pp. 215–278, 1979.

[101] A. S. Bablumian and T. F. Krile, "Multiplexed holograms in thick bacteriorhodopsin films for optical memory/interconnections," *Optical Engineering* **39**, pp. 2964–2974, 2000.

[102] J. D. Downie, D. A. Timuçin, D. T. Smithey, and M. Crew, "Long holographiclife-times in bacteriorhodopsin films," *Optics Letters* **23**, pp. 730–732, 1998.

[103] F. Wang, L. Liu, and Q. Li, "Readout of a real-time hologram in bacteriorhodopsin film with high diffraction efficiency and intensity," *Optics Letters* **21**, pp. 1697–1699, 1996.

[104] Z. Chen, H. Takei, A. Lewis, and I. Nebenzahl, "Bacteriorhodopsin oriented in polyvinyl alcohol films as an erasable optical storage medium," *Applied Optics* **30**, pp. 5188–5196, 1991.

[105] Y. Zhang, Q. W. Song, C. Tseronis, and R. R. Birge, "Real-time holographic imaging with a bacteriorhodopsin film," *Optics Letters* **20**, pp. 2429–2431, 1995.

[106] F. J. Aranda, R. Garimella, N. F. McCarthy, D. Narayana Rao, D. V. G. L. N. Rao, Z. Chen, J. A. Akkara, D. L. Kaplan, and J. F. Roach, "All-optical light modulation in bacteriorhodopsin films," *Applied Physics Letters* **67**, pp. 599–601, 1995.

[107] Q. W. Song, C. Zhang, R. Blumer, R. B. Gross, Z. Chen, and R. R. Birge, "Chemically enhanced bacteriorhodopsin thin-film spatial light modulator," *Optics Letters* **18**, pp. 1373–1375, 1993.

[108] R. Thoma, N. A. Hampp, C. Braeuchle, and D. Oesterhelt, "Bacteriorhodopsin films as spatial light modulators for nonlinear-optical filtering," *Optics Letters* **16**, pp. 651–653, 1991.

[109] J. Joseph, F. J. Aranda, D. V. G. L. N. Rao, B. S. Decristofano, B. R. Kimball, and M. Nakashima, "Optical implementation of the wavelet transform by using a bacteriorhodopsin film as an optically addressed spatial light modulator," *Applied Physics Letters* **73**, pp. 1484–1486, 1998.

[110] D. Haronian and A. Lewis, "Elements of a unique bacteriorhodopsin neural network architecture," *Applied Optics* **30**, pp. 597–608, 1991.

[111] T. Zhang, C. Zhang, G. Fu, Y. Li, L. Gu, G. Zhang, Q. Song, B. Parsons, and R. R. Birge, "All-optical logic gates using bacteriorhodopsin films," *Optical Engineering* **39**, pp. 527–534, 2000.

[112] C. P. Singh and S. Roy, "All-optical switching in bacteriorhodopsin based on M state dynamics and its application to photonic logic gates," *Optics Communications* **218**, pp. 55–66, 2003.

[113] V. P. Leppanen, T. J. Haring, T. Jaaskelainen, E. Vartiainen, S. Parkkinen, and J. P. S. Parkkinen, "The intensity dependent refractive index change of photochromic proteins," *Optics Communications* **163**, pp. 189–192, 1999.

[114] Q. W. Song, C. Zhang, R. B. Gross, and R. R. Birge, "The intensity-dependent refractive index of chemically enhanced bacteriorhodopsin," *Optics Communications* **112**, pp. 296–301, 1994.

[115] A. Seitz and N. A. Hampp, "Kinetic optimization of bacteriorhodopsin films for holographic interferometry," *Journal of Physical Chemistry B* **104**, pp. 7183–7192, 2000.

[116] K. P. J. Reddy, "Passive mode locking of lasers using bacteriorhodopsin molecules," *Applied Physics Letters* **64**, pp. 2776–2778, 1994.

[117] Y. Li, Q. Sun, J. Tian, and G. Zhang, "Optical Boolean logic based on degenerate multi-wave mixing in bR film," *Optical Materials* **23**, pp. 285–288, 2003.

[118] J. Tallent, Q. W. Song, Z. Li, J. Stuart, and R. R. Birge, "Effective photochromic nonlinearity of dried blue-membrane bacteriorhodopsin films," *Optics Letters* **21**, pp. 1339–1341, 1996.

[119] C. C. Chang, H. F. Yau, N. J. Cheng, and P. X. Ye, "Pentagon-shaped 0°-cut $BaTiO_3$ as an efficient self-pumped phase conjugator," *Applied Optics* **38**, pp. 7206–7213, 1999.

[120] H. C. Kung, H. F. Yau, H. Y. Lee, N. Kukhtarev, T. C. Chen, C. Cherng Sun, C. C. Chang, and Y. P. Tong, "Double phase conjugation with orthogonally polarized beams in a BaTiO 3 crystal," *Optics Letters* **25**, pp. 1031–1033, 2000.

[121] A. Brignon, S. Breugnot, and J.-P. Huignard, "Very high-gain two-wave mixing in $BaTiO_3$ with a self-bent pump beam," *Optics Letters* **20**, pp. 1689–1691, 1995.

[122] K. Buse and T. Bierwirth, "Dynamics of light-induced absorption in $BaTiO_3$ and application for intensity stabilization," *Optical Society of America Journal B* **12**, pp. 629–637, 1995.

[123] M. U. L. Holtmann, E. Kräatzig, and G. Godefroy, "Conductivity and light-induced absorption in $BaTiO_3$," *Applied Physics A* **51**, pp. 13–17, 1990.

[124] P. Tayebati and D. Mahgerefteh, "Theory of the photorefractive effect for $Bi_{12}SiO_{20}$ and $BaTiO_3$ with shallow traps," *Optical Society of America Journal B* **8**, pp. 1053–1064, 1991.

[125] A. Motes, G. Brost, J. Rotgé, and J. J. Kim, "Temporal behavior of the intensity-dependent absorption in photorefractive $BaTiO_3$," *Optics Letters* **13**, pp. 509–511, 1988.

[126] G. S. He and S. H. Liu, *Physics of Nonlinear Optics*, World Scientific, 1999.

[127] M. Born and E. Wolf, *Principles of Optics*, Oxford: Pergamo, 1965.

[128] A. Yariv, *Quantum Electronics*, Wiley, 3 ed., 1989.

[129] R. K. Banyal and B. R. Prasad, "Light-induced absorption in photorefractive $BaTiO_3$ crystals," *Journal of Applied Physics* **93**, pp. 9466–9469, 2003.

[130] Y. Li, D. Trung, B. Zhang, Y. Segawa, and T. Itoh, "Temperature dependence of light-induced absorption in reduced Co:KNSBN crystal with multiple shallow traps," *Proc. SPIE* **3554**, pp. 33–39, 1998.

[131] G. A. Brost and R. A. Motes, "Photoinduced absorption in photorefractive barium titanate," *Optics Letters* **15**, pp. 538–540, 1990.

[132] M. Kaczmarek, G. W. Ross, R. W. Eason, M. J. Damzen, R. Ramos-Garcia, and M. H. Garrett, "Intensity-dependent absorption and its modelling in infrared sensitive rhodium-doped $BaTiO_3$," *Optics Communications* **126**, pp. 175–184, 1996.

[133] L. Corner, R. Ramos-Garcia, A. Petris, and M. J. Damzen, "Experimental and theoretical characterisation of rhodium-doped barium titanate," *Optics Communications* **143**, pp. 165–172, 1997.

[134] H. Krose, R. Scharfschwerdt, O. F. Schirmer, and H. Hesse, "Light-induced charge transport in $BaTiO_3$ via three charge states of rhodium," *Applied Physics B* **61**, pp. 1–5, 1995.

[135] H. Song, S. X. Dou, M. Chi, H. Gao, Y. Zhu, and P. Ye, "Studies of shallow levels in undoped and rhodium-doped barium titanate," *Optical Society of America Journal B* **15**, pp. 1329–1334, 1998.

[136] R. K. Banyal and B. R. Prasad, "Two-wave mixing and light-induced absorption dynamics in photorefractive $BaTiO_3$ crystals," *Journal of the Indian Institute of Science* **83**, pp. 61–71, 2003.

[137] M. Simon, St. Wevering, K. Buse, and E. Krätzig, "The bulk photovoltaic effect of Photorefractive $LiNbO_3$:Fe crystals at high light intensities," *Journal of Physics D: Applied Physics* **30**, pp. 144–149, 1997.

[138] F. Jermann and K. Buse, "Light-induced thermal gratings in $LiNbO_3$:Fe," *Applied Physics B* **59**, pp. 437–443, 1994.

[139] L. Ren, L. Liu, D. Liu, J. Zu, and Z. Luan, "Optimal switching from recording to fixing for high diffration from a $LiNbO_3$:Ce:Cu photoreractive non-volatile holograms," *Optics Letters* **29**, pp. 186–188, 2004.

[140] G. Zhang, S. Sunarno, M. Hoshi, Y. Yomita, C. Yang, and W. Xu, "Charaterization of two-color holography performance in reduced $LiNbO_3$:In," *Applied Optics* **40**, pp. 5248–5252, 2001.

[141] Q. Dong, L. Liu, D. Liu, C. Dai, and L. Ren, "Effect of dopant composition ratio on nonvolatile holographic recording in $LiNbO_3$:Cu:Ce crystals," *Applied Optics* **43**, pp. 5016–5022, 2004.

[142] M. Lee, S.Takekawa, Y. Furukawa, and K. Kitamura, "Quasinondestructive holographic recording in photochromic $LiNbO_3$," *Physical review Letters* **84**, pp. 875–878, 2000.

[143] H. Guenther, G. Wittmann, R. M. Macfarlane, and R. R. Neurgaonkar, "Intensity dependence and white-light gating of two-color photorefractive grating in $LiNbO_3$," *Optics Letters* **22**, pp. 1305–1307, 1997.

[144] S. Odoulov, T. Tarabrova, and A. Shumelyuk, "Photorefractive response of bulk periodically poled $LiNbO_3$:Y:Fe at high and low spatial frequencies," *Physical Review Letters* **84**, pp. 3294–3297, 2000.

[145] S. Breer, K. Buse, and F. Rickermann, "Improved development of thermally fixed holograms in photorefractive linbo$_3$ crystals with high-intensity laser pulses," *Optics Letters* **23**, pp. 73–75, 1998.

[146] P. Gunter, J. P. Huignard, and P. Yeh, "Photorefractive Materials and Their Applications," *Applied Optics* **28**, pp. 3813–3820, 1989.

[147] K. Takizawa, T. Fujii, M. Kawakita, H. Kikuchi, H. Fujikake, M. Yokozawa, A. Murata, and K. Kishi, "Spatial light modulators for projection displays," *Applied Optics* **36**, pp. 5732–5747, 1997.

[148] J. A. Coy, M. Zaldarriaga, D. F. Grosz, and O. E. Martinez, "Characterization of a liquid crystal television as a programmable spatial light modulator," *Optical Engineering* **35**, pp. 15–19, 1996.

[149] C. Soutar, S. E. Monroe, and J. Knopp, "Measurement of the complex transmittance of the Epson liquid crystal television," *Optical Engineering* **33**, pp. 1061–1068, 1994.

[150] C. Soutar, S. E. Monroe, and J. Knopp, "Complex characterization of the Epson liquid crystal television," in *Proc. SPIE Vol. 1959, p. 269-277, Optical Pattern Recognition IV, David P. Casasent; Ed.*, pp. 269–277, 1993.

[151] J. C. Kirsch, D. A. Gregory, M. W. Thie, and B. K. Jones, "Modulation characteristics of the Epson liquid crystal television," *Optical Engineering* **31**, pp. 963–970, 1992.

[152] G. T. Bold, T. H. Barnes, J. Gourlay, R. M. Sharples, and T. G. Haskell, "Practical issues for the use of liquid crystal spatial light modulators in adaptive optics," *Optics Communications* **148**, pp. 323–330, 1998.

[153] D. A. Gregory, J. C. Kirsch, and E. C. Tam, "Full complex modulation using liquid-crystal televisions," *Applied Optics* **31**, pp. 163–165, 1992.

[154] A. Miniewicz, A. Gniewek, and J. Parka, "Liquid crystals for photonics applications," *Optical Materials* **21**, pp. 605–610, 2003.

[155] G. G. Yang and S. E. Broomfield, "Programmable wavefront generation using two binary phase spatial light modulators," *Optics Communications* **124**, pp. 345–353, 1996.

[156] H.-Y. Tu, C.-J. Cheng, and M.-L. Chen, "Optical image encryption based on polarization encoding by liquid crystal spatial light modulators," *Journal of Optics A: Pure and Apllied Optics* **6**, pp. 524–528, 2004.

[157] P. Birch, R. Young, D. Budgett, and C. Chatwin, "Dynamic complex wave-front modulation with an analog spatial light modulator," *Optics Letters* **26**, pp. 920–922, 2001.

[158] R. L. Eriksen, P. C. Mogensen, and J. Glückstad, "Elliptical polarisation encoding in two dimensions using phase-only spatial light modulators," *Optics Communications* **187**, pp. 325–336, 2001.

[159] C. Cheng and M. Chen, "Polarization encoding for optical encryption using twisted nematic liquid crystal spatial light modulators," *Optics Communications* **237**, pp. 45–52, 2004.

[160] E. J. Haellstig, L. Sjoeqvist, and M. Lindgren, "Intensity variations using a quantized spatial light modulator for nonmechanical beam steering," *Optical Engineering* **42**, pp. 613–619, 2003.

[161] J. L. Sanford, P. F. Grier, K. H. Yang, M. Lu, R. S. J. Olyha, C. Narayan, J. A. Hoffnagle, P. M. Alt, and R. L. Melcher, "A one megapixel reflective spatial light modulator system for holographic storage," *IBM J. Res. Develop.* **42**, pp. 411–425, 1998.

[162] D. B. Glenn and R. R. Edward, "Modulation depth characterstics of a liquid crystal television spatial light modulators," *Journal of Optics A: Pure and Applied Optics* **27**, pp. 2940–2943, 1988.

[163] B. E. A. Salesh and M. C. Teich, *Fundamentals of Photonics*, Wiley, 1991.

[164] A. Yariv and P. yeh, *Optical waves in Crystals*, Wiley, New York, 1984.

[165] K. Lu and B. E. A. Saleh, "Theory and design of liquid crystal TV as an optical spatial phase modulator," *Optical Engineering* **29**, pp. 240–246, 1990.

[166] P. G. de Gennes and J. Prost, *The Physics of Liquid Crystals*, Oxford University Press, 2 ed., 1995.

[167] C. Soutar and K. Lu, "Determination of the physical properties of an arbitrary twisted-nematic liquid crystal cell," *Optical Engineering* **33**, pp. 2704–2712, 1994.

[168] P. Hariharan, *Basics of Interferometry*, Lightning Source Inc, 1 ed., 1992.

[169] R. K. Banyal and B. R. Prasad, "Pixel size and pitch measurements of liquid crystal spatial light modulator by optical diffraction," *Pramana –Journal of Physics* **65**, pp. 291–296, 2005.

[170] J. W. Goodman, *Introduction to Fourier Optics*, McGraw-Hill, 2 ed., 1996.

[171] G. Vdovin, "Spatial light modulator based on the control of the wavefront curvature," *Optics Communication* **115**, pp. 170–178, 1995.

[172] G. W. Burr, G. Barking, H. Coufal, J. A. Hoffnagle, C. M. Jefferson, and M. A. Neifeld, "Gray-scale data pages for digital holographic data storage," *Optics Letters* **23**, pp. 1218–1220, 1998.

[173] S. Gravano, *Introduction to Error Control Codes*, Oxford University Press, 1 ed., 2001.

[174] D. E. Pansatiankul and A. A. Sawchuk, "Variable-length two-dimensional modulation coding for imaging page-oriented optical data storage systems," *Applied Optics* **42**, pp. 275–290, 2003.

[175] N. Ahmed, T. Natarajan, and K. R. Rao, "On image processing and a discrete cosine transform," *IEEE transaction on Computers* **23**, pp. 20–23, 1974.

[176] A. B. Watson, "Image compression using discrete cosine transform," *Mathematica Journal* **4**, pp. 81–88, 1994.

[177] P. Addison, "The little wave with the big future," *Physics World* **17**, pp. 35–39, 2004.

[178] R. DeVore, B. Jawerth, and B. Lucier, "Images compression through wavelet transform coding," *IEEE Trans. Information* **38**, pp. 719–746, 1992.

[179] S. Subhasis, "Image compression - from DCT to wavelets: A review," 2000. Electronic version available at: http://www.acm.org/crossroads/xrds6-3/sahaimgcoding.html.

[180] I. Daubechies, *Ten Lectures on Wavelets*, CMBS 61, SIAM Press, Philadelphia PA, 1992.

[181] C. Chui, *An Introduction to Wavelets*, Academic Press, San Diego CA, 1992.

[182] B. H. Barbara, *The World According to Wavelets*, University Press India Pvt. Ltd., 2 ed., 2003.

[183] J. Dongarra, *Sparse Matrix Storage Formats in Zhaojun Bai et al, Eds., Template for Solution of Algebraic Eigenvalue Problems: A Practical Guide*, SIAM, Phillandephia, 2000.

[184] A. Ekambaran and E. Montagne, "An alternative compressed storage format for sparse matrices," *Computer and Information Sciences: ISCIS 2003, LNCS 2869, Springer-Verlag* , pp. 196–203, 1992.

[185] R. C. Gonzalez and R. E. Woods, *Digital Image Processing*, Pearson Education Asia, 2 ed., 2002.

[186] R. L. White and J. W. Percival, "Compression and Progressive Transmission of Astronomical Images," *Bulletin of the American Astronomical Society* **26**, pp. 1513–1523, 1994.

[187] J. L. Starck, F. Murtagh, P. Querre, and F. Bonnarel, "Entropy and astronomical data analysis: Perspectives from multiresolution analysis," *Astronomy & Astrophysics* **368**, pp. 730–746, 2001.

[188] F. M. J. L. Starck, "Astronomical image and signal processing," *IEEE Signal Processing magazine* **18**, pp. 30–40, 2001.

[189] D. A. Huffman, "A method for the construction of minimum-redundancy codes," in *Proceedings of the I.R.E.*, pp. 1098–1101, 1952.

[190] P. G. Howard and J. S. Vitter, "Arithmetic coding for data compression," *Proceedings of the IEEE* **82**, pp. 857–865, 1994.

[191] L. K. Tóth–Boconádi and W. Stoeckenius, "Late events in the photocycle of the bacteriorhodopsin mutant l93a," *Biophysical Journal* **84**, pp. 3848–3856, 2003.

[192] L. K. Tóth-Boconádi and W. Stoeckenius, "Photoexcitation of the o intermediate in bacteriorhodopsin mutant l93a," *Biophysical Journal* **84**, pp. 3857–3863, 2003.

[193] T. Jaaskelainen, V. P. Leppanen, S. Parkkinen, J. S. P. Parkkinen, and A. Khodonov, "The photochromic properties of 4-keto bacteriorhodopsin," *Optical Materials* **6**, pp. 339–345, 1996.

[194] D. A. Timuçin and J. D. Downie, "Phenomenological theory of photochromic media: optical data storage and processing with bacteriorhodopsin films," *Journal of Optical Society of America A* **14**, pp. 3285–3299, 1997.

[195] K. P. J. Reddy, "Analysis of light-induced processes in bacteriorhodopsin and its application for spatial light modulation," *Journal of Applied Physics* **77**, pp. 6108–6113, 1995.

[196] S. Roy, C. P. Singh, and K. P. J. Reddy, "Generalized model for all-optical light modulation in bacteriorhodopsin," *Journal of Applied Physics* , 2001.

[197] R. K. Banyal, G. M. Hegde, B. R. Prasad, and K. P. J. Reddy, "A time-dependent multistate model for bacteriorhodopsin photocycle," *Current Applied Physics* **5**, pp. 133–138, 2005.

[198] C. G. K. Ludmann and G. Váró, "Kinetic and thermodynamic study of the Bacteriorhodopsin photocycle over a wide pH range," *Biophysical Journal* **75**, pp. 3110–3119, 1998.

[199] C. G. K. Ludmann, András Dér, and G. Váró, "Electric signal during the bacteriorhodopsin photocycle, determined over a wide pH range," *Biophysical Journal* **75**, pp. 3120–3126, 1998.

[200] R. G. Zepp and D. M. Cline, "Rate of direct photolysis in acquatic environment," *Environment Science and Technology* **11**, pp. 359–366, 1977.

[201] K. J. Wise, N. B. Gillespie, J. A. Stuart, M. P. Krebs, and R. R. Birge, "Optimization of bacteriorhodopsin for bioelectronics devices," *Trends in Biotechnology* **20**, pp. 387–394, 2002.

[202] P. Wu, D. V. G. L. N. Rao, B. R. Kimball, M. Nakashima, and B. S. DeCristofano, "Enhancement of photoinduced anisotropy and all-optical switching in Bacteriorhodopsin films," *Applied Physics Letters* **81**, pp. 3888–3890, 2002.

[203] Y. Huang, S. Wu, and Y. Zhao, "Photonic switching based on the photoinduced birefringence in bacteriorhodopsin films," *Applied Physics Letters* **84**, pp. 2028–2030, 2004.

[204] P. Ormos, L. Fábián, L. Oroszi, E. K. Wolff, J. J. Ramsden, and A. Dér, "Protein-based integrated optical switching and modulation," *Applied Physics Letters* **80**, pp. 4060–4062, 2002.

[205] Y. Huang, S. Wu, and Y. Zhao, "All-optical switching characteristics in bacteriorhodopsin and its applications in integrated optics," *Optics Express* **12**, pp. 895–906, 2004.

[206] S. Roy, P. Sharma, A. K. Dharmadhikari, and D. Mathur, "All-optical switching with bacteriorhodopsin," *Optics Communications* **237**, pp. 251–256, 2004.

[207] R. K. Banyal and B. R. Prasad, "High contrast all-optical switching in bacteriorhodopsin films," *To be published in Sep. 2005 issue of Applied Optics* .

[208] D. V. G. L. N. Rao, F. J. Aranda, B. J. Wiley, J. A. Akkara, D. L. Kaplan, and J. F. Roach, "Mirrorless all-optical bistability in bacteriorhodopsin," *Applied Physics Letters* **63**, pp. 1489–1491, 1993.

[209] T. S. Y. Fransis, S. Jutamulia, and E. S. Yin (Eds.), *Introduction to Information Optics*, Chap. 4, Academic Press, 2001.

[210] K. Buse, A. Adibi, and D. Psaltis, "Non-volatile holographic storage in doubly doped lithium niobate crystals," *Nature* **393**, pp. 665–668, 1998.

[211] R. John, J. Joseph, and K. Singh, "Holographic digital data storage using phase-modulated pixels," *Optics and Lasers in Engineering* **43**, pp. 183–194, 2005.

[212] *Operation manual, 2085 Argon-ion laser: –Spectra Physics.*

[213] *Operation manual, Millennia*^{TM} *V: –Spectra Physics.*

[214] *Operation manual, Ti:Sapphire 3099S: –Spectra Physics.*

[215] *Operational Manual, Multi-Channel Optical Power Meter 4832-C: –Newport.*